Multi-proxy reconstruction of Holocene and Late Glacial climate variability using precisely dated speleothems from the Herbstlabyrinth, central Germany

Dissertation
zur Erlangung des Grades

"Doktor der Naturwissenschaften"

im Promotionsfach Geowissenschaften
am Fachbereich Chemie, Pharmazie und Geowissenschaften
der Johannes Gutenberg-Universität
in Mainz

Simon André Mischel

geb. in Herborn
Mainz, den 01.08.2016

Abstract

Speleothems grew in isolated places, in complete darkness and in harsh environments, in caves. Even so they are influenced by the climate of the surface surrounding the cave via percolating water from which they are precipitated. It is obvious that, beside the climate, the surface features, for example the type of vegetation, the stucture of the host rock and the soil properties alter the composition of the percolating water and thus, subsequently influences the drip water constituents. As a consequence, the geochemical composition of the precipitated speleothems are influenced by a variety of processes. These processes are of great interest when analysing speleothems, as they can vary spatially and temporally. The Herbstlabyrinth-Adventhöhle cave system provide an ideal place to study terrestrial past climate variability.

First of all, the recent behavior of the drip water to seasonal or annual surface climate variability need to be investigated. This is achieved by a cave monitoring, where site specific influences can be discovered and important new insights in karst hydrology and speleothem science can be achieved. With this knowledge the interpretation of the proxy signals from the speleothems can be examined. To disentangle the individual influencing factors, sampling speleothems from different parts of the cave can help solving the variability on the spatial domain. To explain to which extent past climate variability is recorded by the speleothems, coeval specimen need to be analysed.

In this thesis important progress could be made in terms of understanding the influences of climate pattern affecting the cave environment and the drip water and thus, the speleothems. The North Atlantic Oscillation has strong influence on the δ^{18}O values of the precipitation at the research area and subsequently, the drip water δ^{18}O values. A combination of research in the field and numeric modelling provide insight into the site specific behavior of the drip sites in the cave. As a consequence, the cave monitoring results should be combined with the speleothems sampled inside the cave.

Providing precisely dated, coeval speleothem proxy records of Late Glacial and Holocene age, the HL cave system is an ideal place to study past climate variability on the temporal domain. With the findings of the cave monitoring, the geochemical features of the speleothems could be examined. Combining the results of the drip water with the calcite of the speleothem, the trace element and stable isotope measurements enabled to break down the main influencing factors during spelethem growth. On a local scale the vegetation and the soil properties have a major impact on the geochemical constituents of the speleothems. The study revealed connections between the region of the Herbstlabyrinth with the polar North Atlantic.

Zusammenfassung

Speläotheme bilden sich in isolierter Umgebung, in kompletter Dunkelheit und in einer rauen Umgebung, in Höhlen. Trotzdem ist die Bildung dieser Tropfsteine durch das Sickerwasser an das Klima in der Umgebung der Höhle gekoppelt. Somit wird ersichtlich, dass neben dem Klima, wichtige Einflussfaktoren auf das Sickerwasser und somit auch auf die geochemischen Eigenschaften des Tropfwassers in der Vegetation, der Struktur des Ausgangsgesteines und den Bodeneigenschaften zu suchen sind. Konsequenterweise sind eine Vielzahl an Prozessen an der geochemischen Beschaffenheit der Tropfsteine beteiligt, welche sich räumlich und zeitlich variabel gestalten. Das Herbstlabyrinth-Adventhöhle System bietet einen idealen, kontinentalen Ort um das Klima der Vergangenheit zu studieren.

An erster Stelle stehen Untersuchungen, welche die Einflüsse der saisonalen und jährlichen Klimavariabilität auf der Tropfwasser analysieren. Dies ermöglicht ein Höhlenmonitoring, womit standortspezifische Einflüsse sowie neue Einblicke in die Karsthydrologie und für die Tropfsteininterpretation aufgezeigt werden können. Dieses Wissen bietet eine Grundlage für die Interpretation der Proxysignale der Tropfsteine. Um die räumliche Variabilität der Einflussfaktoren untersuchen tu können, ist es wichtig, Tropfsteine aus verschiedenen Teilen der Höhle zu beproben. Tropfsteine des gleichen Zeitabschnitts der Ergeschichte ermöglichen die Untersuchung des Einflusses des Klimas der Vergangenheit.

In dieser Arbeit wurde ein wichtiger Beitrag zu den Einflüssen des Klimas auf das Untersuchungsgebiet und des Tropfwassers, und damit auch auf die Tropfsteine, geleistet. Die Nordatlantische Oszillation hat einen Einfluss auf die δ^{18}O Werte des Niederschlags und somit auch auf die δ^{18}O Werte des Tropfwassers. Die Verbindung von Feldstudien und numerischen Modellen erlaubt Einblicke in das Verhalten der Tropfstellen in der Höhle. Konsequenterweise sollten diese Ergebnisse mit den Tropfsteinproben aus der Höhle verknüpft werden.

Die präzise datierten, zeitgleich entstandenen Tropfsteine bieten Proxydaten spätglazialen und holozänen Alters und machen somit das Höhlensystem zu einem idealen Ort um das Klima der Vergangenheit zu studieren. Mit den Erkenntnissen des Höhlenmonitoring können die geochemischen Eigenschaften der Tropfsteine detailiert analysiert werden. Die Kombination der Tropfwasseruntersuchungen mit den Speläothemen in Bezug auf Spurenelemente und stabile Isotope erlaubt eine Untersuchung der Haupteinflussfaktoren auf das Tropfsteinwachstum. Wichtige lokale Einflussfaktoren auf die Tropfsteine stellen die Vegetation und die Bodeneigenschaften dar. Die vorliegende Arbeit zeigt eine Verbindung des Untersuchungsgebietes mit dem polaren Nordatlantik.

Contents

List of Figures

List of Tables

1 Introduction

Speleothems are secondary carbonate precipitates found in limestone caves all over the world which are widely used as paleoclimate archives (Lauritzen and Lundberg 1999; Henderson 2006). Speleothems can be precisely dated with the ^{230}Th\U-disequilibrium method (Richards and Dorale 2003; Scholz and Hoffmann 2008) and a variety of proxies can be measured with high resolution. To understand past climate variability. In most studies stalagmites are examined, however, there are some studies using stalagtites or flowstones (Ayalon et al. 1999; Spötl and Mangini 2007). Speleothems can be used to reconstruct various past environmental conditions, such as precipitation (Goede and Vogel 1991; Ayalon et al. 1999; Roberts et al. 1998; McDonald et al. 2007), temperature (Frisia et al. 2003; Mattey et al. 2008; Scholz et al. 2012) and vegetation and soil characteristics (Hellstrom and McCulloch 2000; Huang et al. 2001). They can give important insight into the karst hydrology (Roberts et al. 1998; Treble et al. 2003) and provide information on anthropogenic impact in the catchment area (Verheyden 2004; Henderson 2006). In addition, speleothems have great potential to contribute to the field of paleoclimatology by analysing stable carbon and oxygen isotopes (Spötl and Mangini 2007; Mattey et al. 2008; Spötl et al. 2008), when applying state-of-the-art techniques to the samples. Speleothem research can enhance the understanding of past climate variability and can help to predict future climate change (Henderson 2006).

The processes influencing the geochemical composition of speleothems need careful consideration and investigation on the spatial and temporal domain. For a better understanding of these processes a variety of cave monitoring studies have been established in recent years all over the world (Tooth and Fairchild 2003; Spötl et al. 2005; McDonald et al. 2007; Asrat et al. 2008; Genty 2008; Mattey et al. 2008; Riechelmann et al. 2011; Genty et al. 2014). The processes occuring at each cave site are unique and need careful investigation to form a valuable paleoclimate reconstruction based on speleothems from these caves (e.g.,: Henderson 2006; McDermott et al. 1999; Fairchild et al. 2006).

Speleothems from the Herbstlabyrinth-Adventhöhle (HL) cave system were first analysed in the framework of a diploma-thesis with the title: "Petrographische Untersuchungen, ^{230}Th\U-Altersdatierungen und Spurenelementanalysen an Speläothemen aus dem Herbstlabyrinth-Adventhöhle-System bei Breitscheid-Erdbach, Hessen" (Mischel 2010). It became obvious that the HL cave system is an ideal place for paleoclimate research using speleothems. Due to the fact that the first sampled speleothem grew during the Holocene, this climate period was in the focus of the research conducted within the framework of this PhD thesis. One major aim

of this work was the understanding of the processes influencing the geochemical properties of the recent drip water. Therefore, data from the cave monitoring program was used to investigate influences of the North Atlantic Oscillation (NAO) on the $\delta^{18}O$ values of the drip water (**Chapter 2**). Another important aim of this work was the understanding of the proxy signals from the speleothems. Combining the cave monitoring data and different statistical methods allowed the interpretation of speleothem proxy data in terms of past vegetation productivity. Additionally, a comparison with other paleoclimate archives (ice core, lake sediments) was established and a connection between the HL region with the North Atlantic region during the Holocene was identified (**Chapter 3**). Beside stable isotope ratios a major part of the analysis performed on the speleothems are trace element analysis at high spatial resolution using laser ablation inductively coupled plasma massspectrometry (LA-ICPMS). this method is also of great interest for a variety of geological and environmental studies. For data evaluation of these measurements an R script (TERMITE) was developed, which allows fast calculation of the corresponding concentrations either performed using single spot or line scan measurements (**Chapter 4**).

1.1 Speleothems

Caves are often decorated with speleothems, these calcite formations are found in limestone caves all over the world and are widely used as paleoclimate archives (Lauritzen and Lundberg 1999; Henderson 2006). Stalagmites form a reliable paleoclimate archive, but there are some studies using stalagtites or flowstones (Ayalon et al. 1999; Spötl and Mangini 2007). The solution which enters the cave from which a speleothem can be precipitated is coupled to the meteoric water cycle (Figure 1.1) through the precipitation falling above the cave (Lauritzen and Lundberg 1999; Fairchild et al. 2006). Meteoric precipitation seeps into the soil and the complex interplay of soil properties, vegetation cover and the epikarst ultimatively alters the geochemical properties of the drip water forming the speleothem (Fairchild et al. 2006).

A high soil pCO_2 changes the pH of the soil water to lower values which is required to change the saturation state of the water. This acidic water is then able to desolve carbonate. Changing the pH through different pCO_2 is mostly achived through bacterial activity and microorganisms in the root zone of the soil (Ford and Williams 2007). The soil water is in equilibrium with a high pCO_2. When this water reaches air filled fissures and cavities or a cave passage with a lower pCO_2, CO_2 degasses from the solution resulting in higher pH values and, thus, the solution gets supersaturated with respect to calcite resulting in the precipitation of calcite (Hansen et al. 2013). This process is called Prior Calciate Precipitation (PCP), which influences trace element composition of the drip water and the speleothems. Another important mechanism changing the geochemical content of the drip water is the time the water is in contact with the host rock. Residence time is linked to the amount of precipitation falling above the cave (Tooth and Fairchild 2003). Trace element concentations

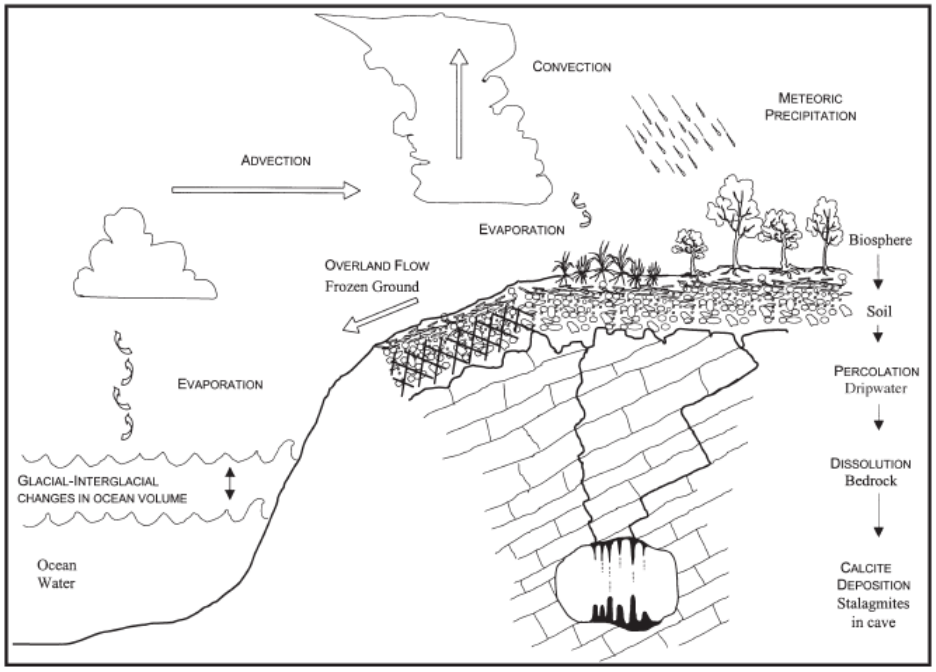

Figure 1.1: Schematic pathways of the meteoric precipitation to a drip site (Lauritzen and Lundberg 1999).

in speleothems can also be altered by the overlying soil and sediments (Figure 1.1). Due to this fact, each drip site and thus, the resulting speleothem formed by the percolation water bears an unique geochemical composition. These properties need to be deciphered for each individual sample and in a next step, the variations need to be put into a paleoclimate context (e.g.,: Henderson 2006; McDermott et al. 1999; Fairchild et al. 2006).

1.2 U-Th-dating

Carbonates, such as speleothems, can be precisely dated using the Uranium-series disequilibrium method (Richards and Dorale 2003; Scholz and Hoffmann 2008). In recent years, the analytical techniques using state-of-the-art multi collector inductively coupled mass spectrometer (MC-ICPMS) improved the precision of the obtained ages (Hoffmann et al. 2007) and allows the calculation of age-depth-models (Scholz and Hoffmann 2011; Scholz et al. 2012).

Elemental fractionation between Uranium and Thorium is a prerequisite for the disequilibrium method (Scholz and Hoffmann 2008). Uranium is soluble in water and can be transported into the cave and incorporated into a speleothem. Contrasting Thorium which is bound to particels and therefore not transported in solution by the drip water into the cave and in an ideal case not present during the formation of speleothems. This geochemical behavior results in a disequilibrium between Th and U isotopes. After the incorporation of Uranium, radioactive decay starts (Figure 1.2, Scholz and Hoffmann 2008).

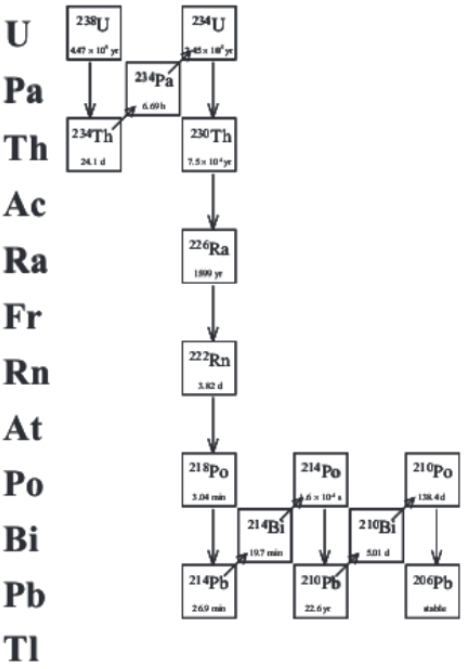

Figure 1.2: The decay chain of ^{238}U (Scholz and Hoffmann 2008).

After deposition, speleothems are most of the time protected against diagenesis. Therefore, it is likely that some basic assumptions are fulfilled. Firstly, the samples are not diagenetically altered after deposition. Neither U nor Th should be lost after the formation of the speleothem, the sample should remain in a closed system. Secondly, no initial ^{230}Th should be present in the drip water and the speleothem. Thirdly, no detrital ^{230}Th, ^{234}U and ^{238}U should be present (Scholz et al. 2014). These assumptions represent an ideal case and are rarely fulfilled in a natural environment. Nevertheless, measuring the activity ratios (^{234}U/^{238}U) and (^{230}Th/^{238}U) allows the calculation of the time the sample was formed. Also essential for reliable dating results is the correction of instrumental biases and a well calibrated spike. In addition, measuring ^{232}Th as a proxy for detrital components is performed and is subsequently used for detrital correction (Scholz and Hoffmann 2008). When these requirements are fulfilled, ages of approximately 600 ka can be obtained (Scholz and Hoffmann 2008; Obert et al. 2016).

1.3 Trace elements and stable isotopes

Figure 1.1 shows the pathways of the meteoric precipitation through the soil towards a specific drip site in the cave. In geological and environmental studies as well as in paleoclimate studies, the trace element concentration and stable isotope ratios are of great interest. They can be

determined at high spatial resolution and are used in a variety of geological and environmental studies. The method used to obtain trace element concentrations is LA-ICPMS and using a MicroMilling to obtain samples at high resolution for stable isotope analysis (Spötl and Mattey 2006).

For example, trace element (e.g. Mg, Sr, Ba, U) to calcium ratios in inorganic as well as biogenic carbonates have been shown to provide valuable information on past climate variability (e.g. Felis et al. 2004; Fairchild and Treble 2009; Mertz-Kraus et al. 2009; Yang et al. 2014; Jochum et al. 2012) and have been established as important climate proxies in various climate archives. In speleothems, trace element concentrations can be used to reconstruct the productivity of the vegetation (Hellstrom and McCulloch 2000; Huang et al. 2001). The amount of precipitation can be reconstructed (McMillan et al. 2005) as well as distinguishing between calcite and aragonite due to different incorporation mechanisms of these elements into the carbonate minerals (Wassenburg et al. 2012). Effects of Prior Calcite Precipitation can be investigated and wet and dry periods during growth of speleothems can be distinguished Fairchild et al. (2000); Fairchild and McMillan (2007); Stoll et al. (2012). One advantage of LA-ICPMS is that only a small amount of sample preparation is needed prior to analysis. Typically, solid samples are analyzed at a spatial resolution of 10 – 150 µm using single spot measurements. Alternatively, a continuous trace element profile can be measured as a line scan with scan speeds ranging from 1 – 200 $\mu m\,s^{-1}$ (Mischel et al. 2016).

The $\delta^{13}C$ ratio of the drip water is ultimately linked to the biospere. Processes occuring in the soil zone, like microbial activity and root respiration of the plants have a great effect on the composition of the $\delta^{13}C$ values of the drip water and thus, the $\delta^{13}C$ of the speleothems. Trace elements and the $\delta^{13}C$ values are influenced by processes occuring in the soil zone and coupled to the productivity of the vegetation and the pCO_2 of the soil air. Beside these processes, effects inside the cave related to cave air exchange with the outside atmosphere are also important. The $\delta^{13}C$ isotopic composition of the cave air often vary inversely with the pCO_2 of the cave air and the drip water composition mirrors these connections (Spötl et al. 2005).

$\delta^{18}O$ values from paleowater are often used to obtain paleotemperatures (Jouzel et al. 2000). Nevertheless, there are different effects, which have an influence on the composition of $\delta^{18}O$ values (e.g. latitude, altitude, amount of precipitation, distance from the source area and temperature McDermott 2004). The variations are linked to climate and are site specific (McDermott 2004). Therefore, a careful investigation of the influencing processes are needed prior to the interpretation of speleothem data.

1.4 The Herbstlabyrinth cave system

The HL cave system is located in the Rhenish Slate Mountains at an elevation of 345 m asl. next to the Fuchtskaute (656 m asl.), the highest mountain of the Westerwald. It is

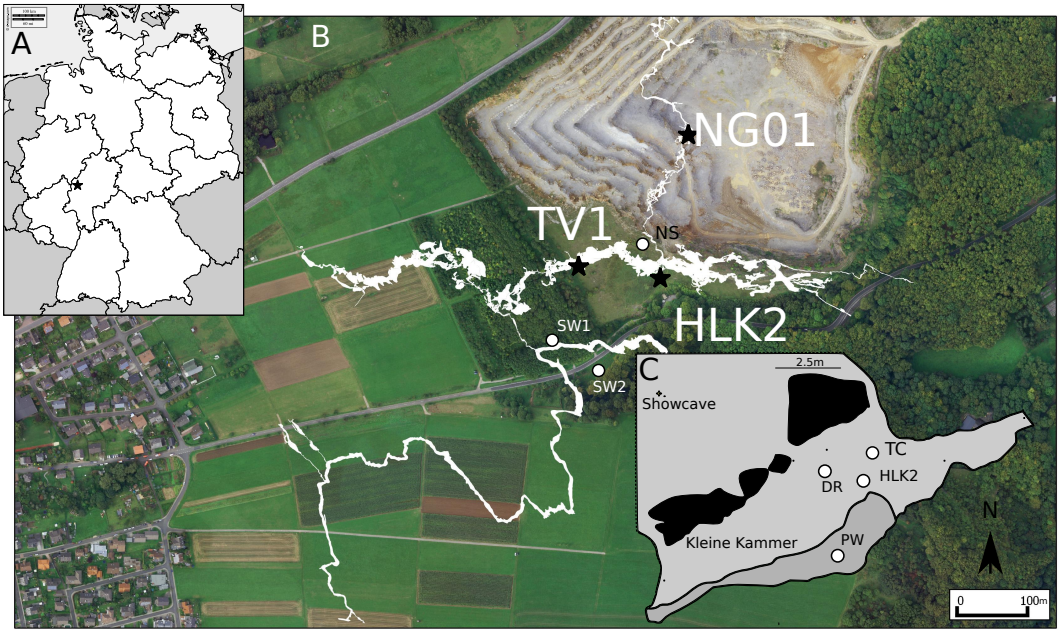

Figure 1.3: A Map of Germany, the black asterisk marks the research area enlarged in (B). B Arial photograph of the cave area. The cave is indicated in white. (NG01) Sampling location of stalagmite NG01. (HLK2) Sampling location of stalagmite HLK2. (TV1) Sampling location of stalagmite TV1. (NS) Location of the weather station. (SW1) Soil water (forest). (SW2) Soil water (meadow). C Enlarged map of the "Kleine Kammer". (TC) Location of the CORA logger. (DR) indicates the drip sites and (PW) the cave pool.

situated in a 3 km^2 area of Upper Devonian limestone and is surrounded by Tertiary volcanic rocks (Richter et al. 2010; Mischel et al. 2015). There are four distinct horizontal levels in the cave system, which locally differentiate in open passages, chambers of different size and sections characterized by breakdown. The lowest level is still hydrologically active with active cave formation. In almost every part of the cave extensive speleothems were formed. In the majority stalagmites and stalactites with various shapes as well as helictites and flowstones developed. Figure 1.3 shows the research area as well as the passages of the cave. The vegetation above the cave is patchy and mainly consists of meadow and deciduous forest. A 60 cm-thick cambisol (Terra fusca) is present above the cave (Mischel et al. 2015).

1.5 Cave monitoring

A cave monitoring is a prerequisite in the deciphering process of the geochemical properties of a speleothem (Tooth and Fairchild 2003; Spötl et al. 2005; McDonald et al. 2007; Asrat et al. 2008; Genty 2008; Mattey et al. 2008; Riechelmann et al. 2011; Genty et al. 2014). Only when the processes occuring on the short timescale are understood, an interpretation of the proxy signals from speleothems covering thousands of years of past climate variability

is feasible. Therefore, since September 2010, a cave monitoring program has been setup in a small chamber ("Kleine Kammer", Figure 1.3C) inside the cave as well as at the surface above the cave (Figure 1.3B). During the cave monitoring the precipitation, soil water and drip water inside the cave were sampled on a monthly basis. Various loggers record cave related climate parameters at high resolution.

1.6 Objectives and aims

The research area of the work presented in this thesis is the Herbstlabyrinth-Adventhöhle cave system. The cave developed in the karstic landscape near Breitscheid-Erdbach in Hesse, central Germany. To interpret the proxy records of the speleothems found inside the cave, an extensive cave monitoring program was installed and maintained for 5 years. The cave monitoring provided a substantial basis for the understanding of the karst processes and the first publication presented in **Chapter 2**, were the relation between the NAO and the drip water δ^{18}O values was examined.

Chapter 3 is a combination of the data from the cave monitoring program and proxy data from the speleothems sampled in the HL cave system. The proxy data from the speleothems were statistically examined and different statistical methods were applied to the data. Principal Component Analysis (PCA) reveals a common pattern found in the time series of three coeval speleothems. The δ^{18}O values from the speleothems are compared with supra-regional climate archives such as ice-cores from greenland (NGRIP) or the lake Ammersee ostracode record. The Principal Component 1 of the trace elements (Mg, P, Ba and U) and the δ^{13}C values explain about 50 % of the overall variability of the proxy records and is interpreted as reflecting past vegetation productivity. This result is further confirmed by a comparison with the Hematite Stained Grain (HSG) record from Bond et al. (1997; 2001). PC1 of all three stalagmites fit well to the HSG record and thus, the HL provides a paleoclimate archive where a close relationship between terrestrial climate in central Europe and the polar North Atlantic is evident.

Chapter 4 provides TERMITE - An R script for fast reduction of LA-ICPMS data and its application to trace element measurements. Running this script programmed in the statistical language R, the user is able to calculate the trace element concentrations obtained by LA-ICPMS in a fast and flexible way which is less prone to errors than already established methods. Data reduction for spot scan measurements as well as line scan measurements can be performed within minutes. The performance of TERMITE is tested using a speleothem sample from the HL cave system, and the usability and the results are compared with the commercial software. Performing trace element measurements is an important tool in paleoclimate research, as the results are of great interest for various geological and environmental studies as well as paleoclimate interpretation using speleothems.

2 δ^{18}O values of cave drip water: a promising proxy for the reconstruction of the North Atlantic Oscillation?

Simon A. Mischel · Denis Scholz · Christoph Spötl

Abstract

We present cave monitoring data and two drip water δ^{18}O models for the Herbstlabyrinth-Adventhöhle (HL) cave system, Germany. Winter climate of the cave region is influenced by the North Atlantic Oscillation (NAO), as documented by the positive correlations between winter temperature, winter rainfall δ^{18}O values and the winter NAO index. Cave monitoring data show that recharge of the aquifer at the HL cave system mainly occurs during winter months, confirming our drip water model, which calculates recharge as the difference between precipitation and potential evapo-transpiration. Cave drip water from the HL cave system should, thus, be a sensitive proxy for reconstruction of the NAO. The infiltration models accounting for mixing effects occurring in the karst aquifer show a very good agreement with the monitoring data. Comparison of the modelled and the monitored drip water δ^{18}O values suggests a mean residence time of the water in the aquifer of 12 months and a transmission time of 10 months. Using these parameters, a long-term dataset from the nearby meteorological station Frankfurt am Main and the rainfall δ^{18}O data from our monitoring program, we model the δ^{18}O values of the cave drip water for the last 144 years. Despite of the favourable conditions of the HL cave system for NAO reconstruction, the modelled drip water δ^{18}O time series only shows a moderate correlation with the winter NAO index (r = 0.33). The major reason for the relatively low correlation is the substantial contribution of precipitation from the remaining seasons to the drip water, for instance, due to heavy precipitation events occurring during summer. These rainfall events bias the seasonality of infiltration and weaken the winter NAO signal recorded in the drip water δ^{18}O values. Reconstruction of the NAO from speleothems is, thus, challenging, in particular considering further complications arising from chronological uncertainties and calcite precipitation under conditions deviating from isotopic equilibrium. These problems may, at least in part, be avoided by multi-proxy studies of annually laminated stalagmites.

Keywords: NAO · Cave monitoring · Stable Isotopes · Modelling

2.1 Introduction

The North Atlantic Oscillation (NAO) has a strong impact on the variation of temperature and precipitation over Europe and the Mediterranean, in particular during winter months (e.g., Hurrell 1995). The NAO index (NAOI) is an indicator of the difference of the normalised sea-level pressure between the stations Stykkishólmur, Iceland, and Lisbon, Portugal (Hurrell 1995) or Stykkishólmur, Iceland, and Gibraltar (Jones et al. 1997) and is associated with the variability of the surface westerlies onto Europe. The observed states of the NAOI can be positive, leading to warmer and wetter than normal winters over Europe and cooler and dryer winters in the Mediterranean. During negative states of the NAOI, the opposite climate pattern is observed. However, these general relationships have been shown to be temporally unstable (Casty et al. 2005).

The influence of the NAO on winter temperature and winter precipitation in Europe (Hurrell 1995; Trigo et al. 2002; Munoz-Diaz and Rodrigo 2003) as well as on the δ^{18}O value of winter precipitation (Baldini et al. 2008) has been studied in detail. Several authors have also studied combined effects of the NAO and other climate patterns, such as the East Atlantic or the Scandinavian pattern (e.g., Comas-Bru and McDermott 2013). Baldini et al. (2008) analysed climate and stable isotope data from 43 stations of the Global Network of Isotopes in Precipitation (GNIP) and found that the relationship between the winter NAOI (defined as the mean NAOI of December, January, February and March, DJFM) and the δ^{18}O value of winter (DJFM) precipitation is most pronounced for two stations in Central Germany (i.e., Koblenz and Wasserkuppe/Rhön), both showing highly positive correlations. Based on these observations, they concluded that "Central Europe is replete with natural archives (alpine ice cores, tree rings, lake sediments, and stalagmites) capable of recording past changes in atmospheric circulation", such as the NAO. Nevertheless, only a few NAO reconstructions are currently available (Cook et al. 1998, based on tree rings; Luterbacher et al. 2001, instrumental and documentary proxy data; Trouet et al. 2009, tree rings and speleothem lamina thickness; Olsen et al. 2012, lake sediments; Wassenburg et al. 2013, speleothem trace element data). An NAO reconstruction based on speleothem δ^{18}O values is not available yet.

Speleothems are secondary calcite precipitates formed inside caves (Fairchild and Baker 2012). The majority of speleothems used for paleoclimate reconstruction are stalagmites and flowstones, either consisting of calcite or aragonite. They offer a climate archive, which can be very precisely dated using U-series disequilibrium methods (Richards and Dorale 2003; Scholz and Hoffmann 2008). The most widely used climate proxies are the stable carbon (δ^{13}C) and oxygen (δ^{18}O) isotopes (McDermott 2004; Lachniet 2009), which can be measured at high temporal resolution (Spötl and Mattey 2006). However, understanding and eventually modelling the processes influencing the formation of speleothems and the archived stable isotope records remains a complex task (Dreybrodt and Scholz 2011; Deininger et al. 2012), and site-specific processes need careful investigation (Fairchild et al. 2006). In order to obtain

a better understanding of the processes influencing the δ^{18}O value of cave drip water and the associated speleothems, cave monitoring has been shown to provide essential information (Tooth and Fairchild 2003; Spötl et al. 2005; Mattey et al. 2008; Riechelmann et al. 2011; Genty et al. 2014). An important point for paleoclimate reconstruction from speleothem δ^{18}O values is the residence time of the water in the karst above the cave, which typically results in substantial smoothing and delaying of the δ^{18}O signal of precipitation. Several cave monitoring programs found relatively long mean residence times of the water in the aquifer before it reaches the drip site (e.g., >1 year, Spötl et al. 2005; 2–4 years, Kluge et al. 2010; several years, Genty et al. 2014).

Most of the groundwater recharge in Central Europe occurs during winter months (Renger et al. 1974; Riechelmann et al. 2011). The major reason for this is that most of the summer precipitation is used up by the vegetation, which has its main growth-period during spring and summer, whereas almost no growth occurs during winter. Furthermore, higher temperature leads to increased evaporation during summer. Both processes are expressed by a high potential evapo-transpiration (pET). In contrast, evapo-transpiration is low or almost zero during winter. Therefore, the reservoirs in a karst aquifer, supplying the drip water ultimately forming speleothems, are mainly fed from the winter precipitation above the cave (Wackerbarth et al. 2010). Consequently, the δ^{18}O value of cave drip water should mainly reflect the climatic conditions at the surface in the cave area during winter.

Here we present data from a 4-year cave monitoring program set up at the Herbstlabyrinth-Adventhöhle (HL) cave system, central Germany. The data enable us to study the characteristics of different drip sites inside the cave in detail and their relationship to outside precipitation and the δ^{18}O values of precipitation. Using the results of this monitoring program, a long-term (1870–2014 AD) climate data set from a nearby meteorological station and two different infiltration models, we simulate the δ^{18}O values of the drip water at the HL cave system. Comparison with the winter NAOI allows us to test whether the relationship between the NAOI and the precipitation δ^{18}O values is transported inside the cave by seepage and consequently, is reflected in the δ^{18}O values of the drip water. Up to now, this study is the first attempt to study in detail the observed relationship between the δ^{18}O values of precipitation and cave drip water, which represents the basis to reconstruct the NAOI from speleothem δ^{18}O values.

2.2 Materials and methods

2.2.1 The Herbstlabyrinth cave system

The HL cave system is located in the Rhenish Slate Mountains in Central Germany (Fig. 2.1a) at an elevation of about 430 m above sea level. The cave developed in Devonian limestone and has a length of about 9 km. It shows four distinct levels and is characterized by an alternation of passages mainly consisting of breakdown and chambers decorated by speleothems. Various kinds of speleothems, including stalactites, stalagmites and flowstones, calcite spar in cave pools as well as helictites, are present. The lowest level of the cave is more than 100 m below the surface and hydrologically active. Since 2009, a show cave has been established inside a small part of the cave, which is located at the second level (ca. 30 m below the surface). In order to minimise the impact on cave climate, visitor access is restricted to the weekends and small groups of up to 15 persons per hour. The vegetation above the cave is patchy and mainly consists of meadow and deciduous forest. A 60 cm-thick Cambisol (Terra fusca) is present above the cave. The regional climate is temperate with dominating westerly winds. There is no distinct rainy season.

2.2.2 The cave monitoring program

Since September 2010, a cave monitoring program has been setup in a small chamber ("Kleine Kammer", Fig. 2.1d) inside the cave as well as at the surface above the cave (Fig. 2.1c). The chamber is located near the show cave. At the surface, air temperature is recorded, and rainwater is collected using a rain gauge (Pluvimate, www.driptych. com), which is sensitive to 0.006 mm/h. Table 2.1 shows the amount of annual precipitation and mean annual temperature for the last 4 years.

Table 2.1: Precipitation and mean annual air temperature measured at the weather station at the cave site

Hydrological cycle	Precipitation (mm/a)	Mean annual air temperature (°C)
2010–2011	581	8.8
2011–2012	944	8.9
2012–2013	912	8.4
2013–2014	776	10.0

An aggregate aliquot of the rainwater is sampled every month. In addition, two soil suction probes (UMS SK20, www.ums-muc.de) are used to obtain soil water samples at a depth of approximately 60 cm. Inside the cave, three fast drip sites (instantaneous sampling), one slow drip site (aggregated sample collected within 1 month) and a cave pool are sampled during monthly cave trips. The average drip rates of the fast drip sites are 0.5, 0.4 and 0.3 drops s^{-1}, respectively. The drip rate of the slow drip site is too slow to determine the drip interval

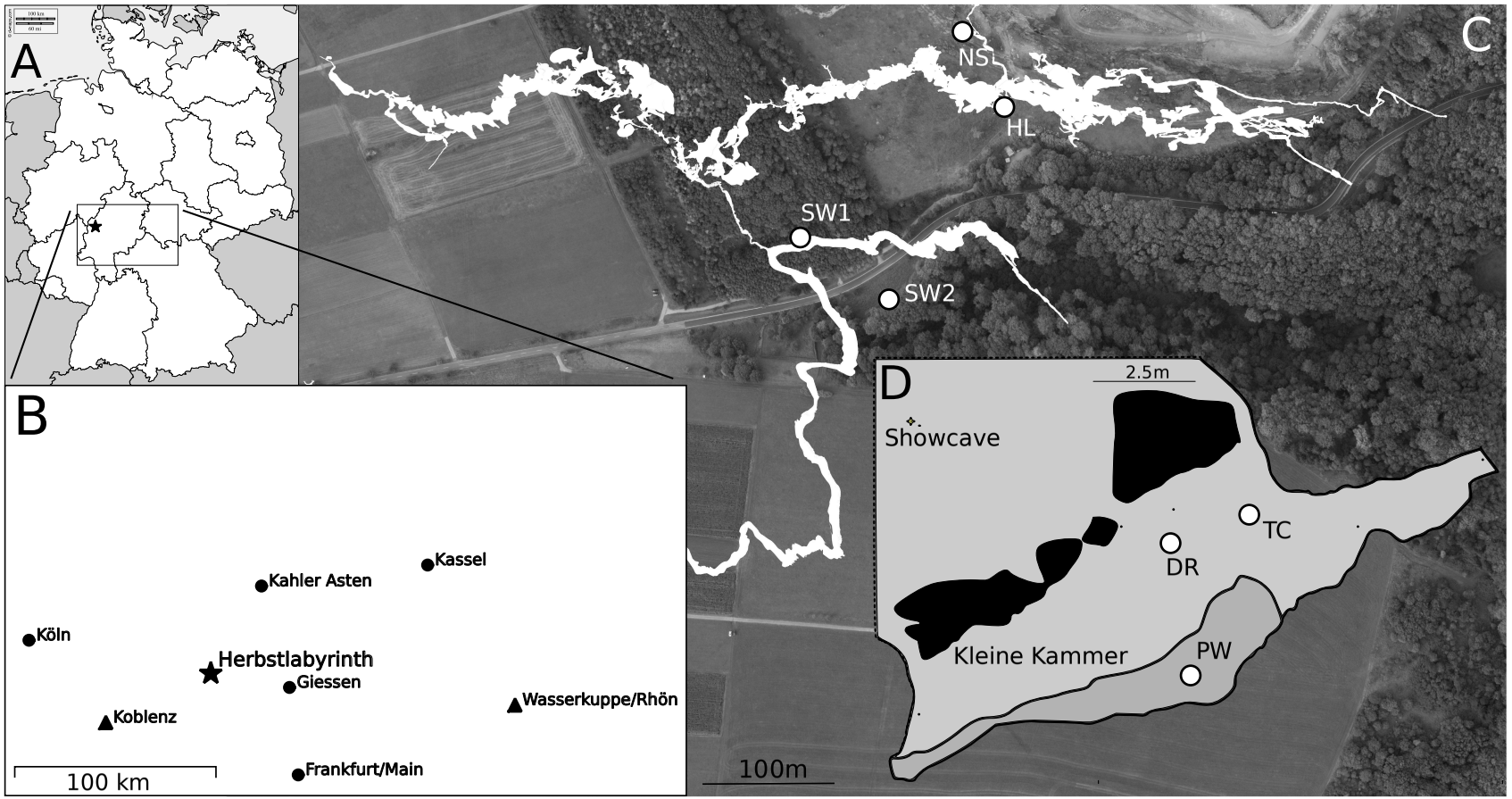

Figure 2.1: *a* Map of Germany, the rectangle marks the area, which is enlarged in panel (*b*). *b* the location of the Herbstlabyrinth-Adventhöhle cave system is marked by the *asterisk*. Also shown are the locations of the meterological stations (*dots*) and the GNIP stations (*triangles*) used in this study. *c* Arial photograph of the cave area. The *cave* is indicated in white. (*NS*) The location of the weather station. (*SW1*) Soil water (*forest*). (*SW2*) Soil water (*meadow*). (*HL*) The location of the "Kleine Kammer". *d* Enlarged map of the "Kleine Kammer". (*TC*) the location of the temperature and the CORA loggers. (*DR*) indicate the drip sites and (*PW*) the cave pool

(i.e., ca. 60 ml/month). Thus, we can only provide an estimate of the drip interval, which is in the range of 1 h. Relative humidity inside the cave is >98 % preventing evaporation inside the cave. In order to prevent evaporative effects prior to analysis, all water samples are filled into gastight vials immediately after recovery. All sampled waters are analysed for pH, electrical conductivity (EC), concentration of cations and anions as well as δ^{18}O and δD values. δ^{18}O and δD values were measured using a ThermoFisher DELTA^{plus}XL mass spectrometer with a Gasbench II and a ThermoFisher DELTA ADVANTAGE coupled to a TC/EA at the University of Innsbruck. These instruments were calibrated using VSMOW, GISP and SLAP. The long-term precision (1σ) of the δ^{18}O and δD values is 0.08 and 1.0 ‰, respectively.

The drip rate of one of the fast drip sites (0.5 drops s^{-1}) is logged at hourly resolution using a Stalagmate drip logger (www.driptych.com), which is capable of recording up to 5 drops/s. In addition, cave air temperature of the small chamber (Fig. 2.1d) is monitored using TinyTag temperature loggers (TGP-4520 and TG-4100, www.geminidataloggers. com) at a resolution of 0.01 °C and an accuracy of 0.5 °C. The pCO_2 of the cave air inside the small chamber (Fig. 2.1d) is logged with a CO_2 recording apparatus (CORA) with an accuracy of 3 % (Luetscher and Ziegler 2012).

Table 2.2: Compilation of the meterological station data

Station	Data source	Availability and resolution of climate parameter [a]				
		T	T_{max}	Precipitation	rH	δ^{18}O
Frankfurt am Main	dwd.de	01 Nov. 1949	01 Nov. 1949	01 Nov. 1949	01 Nov. 1949	NA
Frankfurt am Main	knmi.nl[b]	01 Nov. 1870	01 Nov. 1870	01 Nov. 1870	NA	NA
Giessen	dwd.de	01 Nov. 1949	01 Nov. 1949	01 Nov. 1949	01 Nov. 1949	NA
Köln	dwd.de	01 Nov. 1957	01 Nov. 1957	01 Nov. 1957	01 Nov. 1957	NA
Kahler Asten	dwd.de	01 Nov. 1955	01 Nov. 1955	01 Nov. 1955	01 Nov. 1955	NA
Wasserkuppe/Rhön	dwd.de	01 Nov. 1949	01 Nov. 1949	01 Nov. 1949	01 Nov. 1949	NA
Kassel	dwd.de	01 Nov. 1951	01 Nov. 1951	01 Nov. 1951	01 Nov. 1951	NA
Wasserkuppe/Rhön	GNIP[c]	Jan. 1984-Dec. 2001	NA	Jan. 1978-Dec. 2012	NA	Jan. 1978-Dec. 2013
Koblenz	GNIP[c]	Jan. 1984-Dec. 2001	NA	Jan. 1981-Dec. 2012	NA	Jan. 1981-Dec. 2013

[a] Unless otherwise identified, all data are available at daily resolution until 31 Oct. 2014

[b] The knmi.nl data from Frankfurt am Main contain missing values between March and May 1945

[c] The GNIP data are available at monthly resolution

2.2.3 The climate data

The weather data set from our cave monitoring program currently comprises 4 years. This is obviously too short to compare with the NAOI. Thus, we use meteorological data from meteorological stations surrounding the cave site as input data for our drip water model (Fig. 2.1b), which are available from the Deutscher Wetterdienst (www.dwd.de) and the KNMI Climate Explorer (www.knmi.nl). Table 2.2 provides an overview of the stations used in this study. All stations show a relatively high correlation with our weather data from the Herbstlabyrinth as well as between each other (supplemental Figs. 1–4). All correlations are calculated using the maximum overlap between the corresponding data sets. For the cave monitoring data, this only corresponds to 4 years. Daily temperatures as well as maximum daily temperatures are highly correlated between all stations ($r \geq 0.95$, supplemental Figs. 1 and 2). Daily amounts of precipitation are also significantly correlated between all stations, but the correlation coefficients are lower ($r \geq 0.43$, supplemental Fig. 3). Finally, rH shows a strong positive correlation between all stations at a daily scale ($r \geq 0.64$, supplemental Fig. 4). This shows that the general climate pattern is very similar for all stations, even at the daily scale. The longest data set is available for the meteorological station Frankfurt am Main (Table 2.1; Fig. 2.1) from www.knmi.nl. For the period between 1949 and 2014, this data set is identical with the corresponding data set obtained from www.dwd.de (Table 2.1). The exception is rH, which is only provided by www.dwd.de (Table 2.1). Except for rH, this data set thus offers all data used for our drip water model at the daily scale from 1870 to 2014, covering 144 years. Thus, we only use the climate data from this station in the following.

δ^{18}O values of precipitation were obtained from the GNIP stations Koblenz and Wasserkuppe/Rhön (IAEA/WMO 2014). Here we use an updated data set (Stummp et al. 2014), which covers 36 and 32 years, respectively (Table 2.1). Note that the HL cave system is located in the middle of these two GNIP stations (Fig. 2.1). Using the updated data sets, the correlation between the δ^{18}O values of precipitation from the stations Koblenz and Wasserkuppe/Rhön is 0.71 (supplemental Fig. 5). Both data sets also show a strong correlation with the precipitation δ^{18}O data set from the HL cave system (i.e., 0.68 and 0.79, respectively, supplemental Fig. 5). Thus, it is most likely δ^{18}O values of cave drip water that the δ^{18}O value of winter precipitation at the cave site is also correlated with the NAOI, as observed by Baldini et al. (2008) for the two GNIP stations.

The NAOI has been taken from the Climatic Research Unit at the University of East Anglia (http://www.cru.uea.ac.uk/timo/datapages/naoi.htm). The correlation between the two different NAOI provided by Hurrell (1995) and Jones et al. (1997) is 0.9. Here we use the traditional NAOI, as defined by Hurrell (1995).

2.2.4 The drip water models

We use two different drip water models in this study. The first model is very similar to the model described by Wackerbarth et al. (2010). Thus, we only briefly summarise the underlying basics here.

In limestone areas, the amount of infiltration (Inf) can be approximated by Eq. (2.1), which is, strictly speaking, only applicable for highly fissured limestone when surface runoff is negligible:

$$Inf = Prec - pET \tag{2.1}$$

where Prec is the amount of precipitation and pET is the potential evapo-transpiration. Here we use the approach of (Haude 1954; 1955) to calculate pET [Eq. (2.2)], which has been shown to yield reliable results for Germany (Schiff 1975; Wackerbarth et al. 2010).

$$pET = k * e_s * \left(1 - \frac{rH}{100}\right) \tag{2.2}$$

where e_s is the saturation vapour pressure in hPa (Eq. 2.3) and rH is the relative humidity, both at 14.00 h. k is the Haude coefficient describing different types of vegetation where each month has a specific value. The vegetation above the HL cave system is patchy and consists of forest as well as meadow. Thus, we use two different k values here, for meadow and forest, respectively. pET above the cave is then calculated as the mean pET using the average of both k values.

Several equations to calculate e_s are available (see, for instance, the compilation provided by Alduchov and Eskridge (1996)). Following their suggestion, we calculate e_s according to Eq. (2.3):

$$e_s = 6.1094 * 10^{\left(\frac{17.625 * T_{max}}{243.04 + T_{max}}\right)} \tag{2.3}$$

where T_{max} is the maximum daily temperature.

As discussed in the previous section, climate variables from Frankfurt am Main and above the cave site are correlated (r = 0.99 for temperature and r = 0.43 for precipitation, supplemental Figs. 1 and 3). However, the absolute values are substantially different. In order to account for these differences, we calculate the mean offset between the corresponding climate variables for the two stations (Fig. 2.2). In general, the Frankfurt am Main dataset overestimates T_{max} and T at the HL cave system by 2.45 °C (sd = 1.72 °C) and 2.1 °C (sd = 1.1 °C), respectively. The mean difference in precipitation is small [i.e., 0.57 mm (sd = 4.6 mm) for the period between 2010 and 2014]. Note, however, that the variability of the calculated offsets, in particular on a daily scale, may be considerable (Fig. 2.2), which is also expressed by the relatively large standard deviation.

Equations (2.1), (2.2) and (2.3) and our model are based on daily values, and the meteorological station Frankfurt am Main provides daily data for T, T_{max} and precipitation for the period between 1870 and 2014 (Table 2.2). However, rH is only available from 1949 to 2014. In order to extend the dataset, we calculated a linear regression between rH and T_{max} (supplemental Fig. 6). Infiltration above the HL cave system is then calculated on a monthly scale using Eq. (2.4) and the offset-corrected Frankfurt am Main weather data set:

$$Inf_{month} = \sum Prec_i - \sum pET_i \tag{2.4}$$

where $Prec_i$ and pET_i are daily precipitation and pET, respectively. If monthly potential evapo-transpiration is higher than the amount of monthly precipitation, resulting in a negative value for Inf_{month} [Eq. (2.4)], we set the corresponding value to zero. Note that on the *daily* scale, negative values for infiltration are *not* set to zero. This accounts for the fact that during dry conditions (water stress), the vegetation may also use water stored in the soil zone. According to Wackerbarth et al. (2010), the mean $\delta^{18}O$ value of the cave drip water for one hydrological cycle (i.e., the period from November to October) is calculated as the weighted mean $\delta^{18}O$ value of the infiltrating water [Eq. (2.5)]:

$$\delta^{18}O_{hyd} = \sum G_i * \delta^{18}O_i \tag{2.5}$$

where $\delta^{18}O_{hyd}$ is the modelled $\delta^{18}O$ value for the corresponding hydrological cycle, and G_i and $\delta^{18}O_i$ are the weighting factor and the $\delta^{18}O$ value of precipitation for the individual months, respectively. The weighting factor for the individual months, G_i, is given by the ratio of the monthly to the annual infiltration [Eq. (2.6)]:

$$G_i = \frac{Inf_i}{\sum Inf_i} \tag{2.6}$$

The time series of rainfall $\delta^{18}O$ values from the GNIP stations Koblenz and Wasserkuppe/Rhön are shorter than the weather data set from Frankfurt am Main (Table 2.2). As for rH, we calculated the relationship between $\delta^{18}O$ values of precipitation at the HL cave system and the temperature at the cave site (Fig. 2.3). The relationship is similar for the GNIP stations Koblenz and Wasserkuppe/Rhön (supplemental Fig. 7), which shows that our monitoring $\delta^{18}O$ data are representative for the area as has already been suggested by the high correlation between the individual data sets (supplemental Fig. 5). We then use this relationship to model the $\delta^{18}O$ value of precipitation for the period between 1870 and 2014. Using the extended and offset-corrected datasets, we are able to calculate all values required for Eqs. (2.5) and (2.6) and to model the $\delta^{18}O$ value of the drip water inside the cave for the last 144 years.

Several cave monitoring programs have shown that the mean residence time of the drip water in the karst aquifer typically exceeds 1 year (e.g. Spötl et al. 2005; Genty et al. 2014).

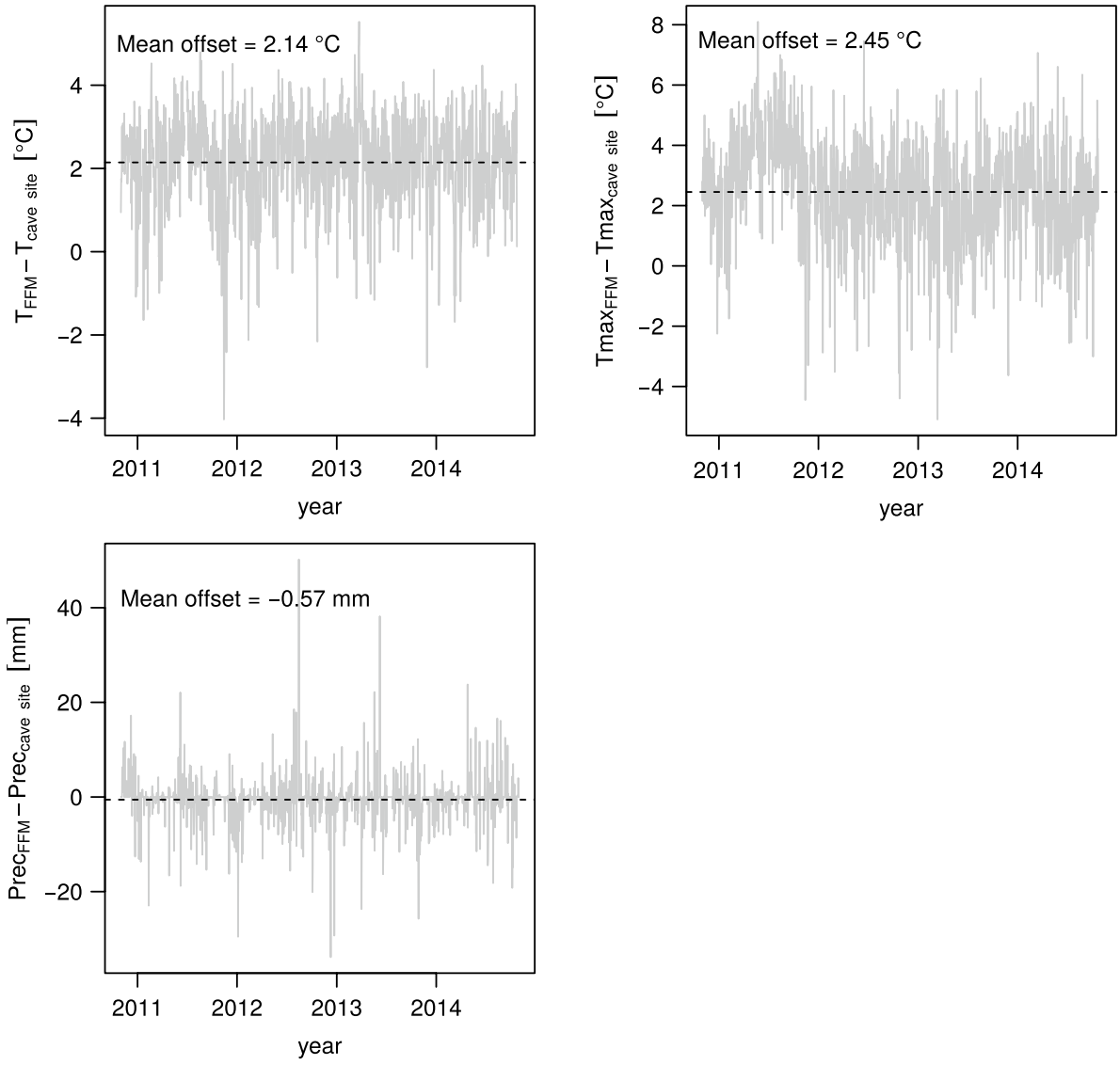

Figure 2.2: Calculated mean offset of different climate parameters between the HL cave site and the climate station Frankfurt am Main for the four hydrological cycles 2010-2014. Shown are daily temperature, maximum daily temperature and precipitation. The dashed black lines marks the mean values used to account for the difference between the Frankfurt am Main dataset and the climate at the cave site

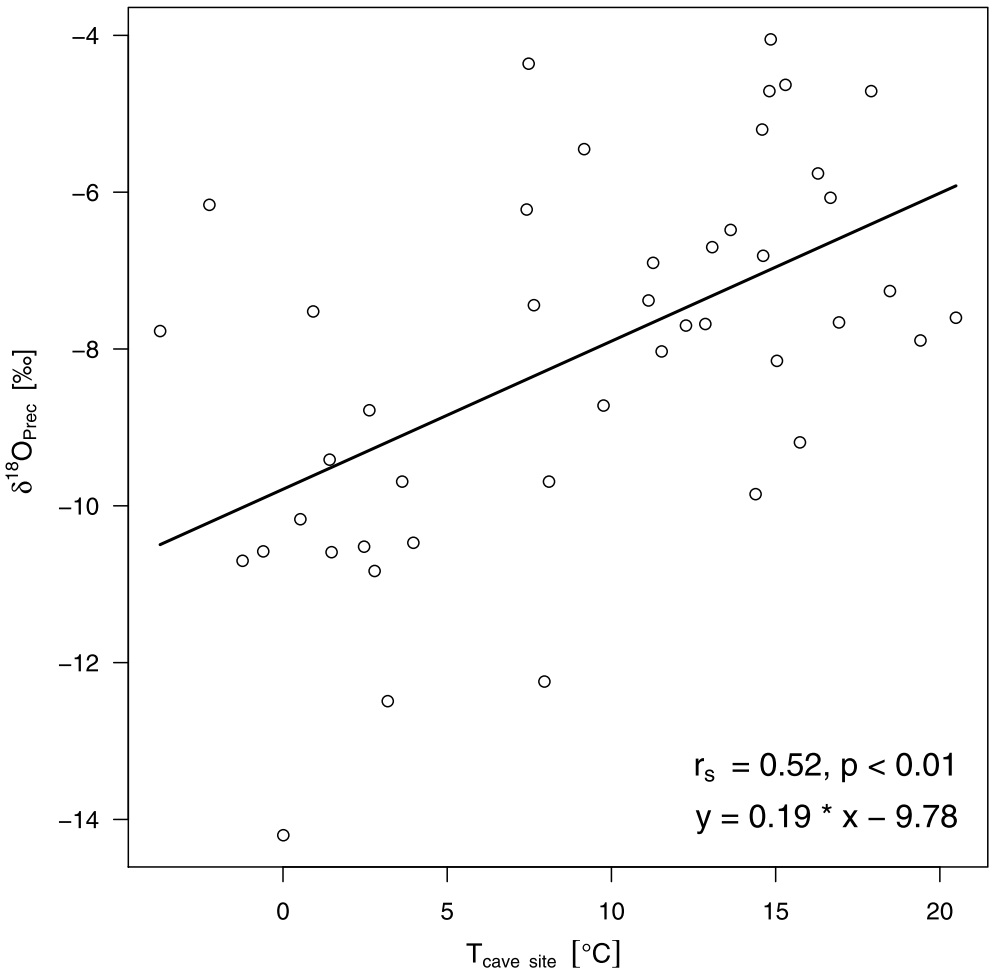

Figure 2.3: Calculated mean offset of different climate parameters between the HL cave site and the climate station Frankfurt am Main for the four hydrological cycles 2010-2014. Shown are daily temperature, maximum daily temperature and precipitation. The dashed black lines marks the mean values used to account for the difference between the Frankfurt am Main dataset and the climate at the cave site

Thus, the drip water may represent a mixture of several years (Williams 2008) rather than only one hydrological cycle, as assumed by our first model. The mixing results in a smoothing of the seasonal δ^{18}O signal of precipitation and may also overprint a potential relationship to the NAO. To account for these processes, we developed another infiltration model (in the following referred to as the "mixing model"), which is capable of simulating longer residence times. In contrast to the first model, this model calculates drip water δ^{18}O values on a monthly scale. Since we collect monthly drip water samples in our cave monitoring program, this model is also more realistic than the first model. Furthermore, we are able to directly correlate the output of the mixing model δ^{18}O values with the measured δ^{18}O values of the cave drip water.

The mixing model assumes that the drip water represents a mixture of the last N months and calculates monthly drip water δ^{18}O values according to Eq. (2.7):

$$\delta^{18}\mathrm{O}_{mixhyd} = \sum_{i=1}^{10} G_i * \delta^{18}\mathrm{O}_i \tag{2.7}$$

which is similar to Eq. (2.5). However, in this case, the weighting factor, G_i , represents the contribution of the corresponding month to the total infiltration during N months (instead of during one hydrological cycle) and is calculated according to Eq. (2.8):

$$G_i = \frac{Inf_i}{\sum_{i=1}^{N} Inf_i} \tag{2.8}$$

For instance, if $N = 24$, the drip water represents a weighted mixture of the last 24 months (months 1–24). The drip water δ^{18}O value of the next month is then simply calculated as the mixture of months 2–25. Note that N does not necessarily have to be a multiple of 12 months. The resulting drip water data set can be considered as a weighted moving average of the rainfall δ^{18}O data.

The output of the mixing model can then be directly correlated with the measured drip water δ^{18}O values. In addition to mixing, which is accounted for by the number of contributing months N, the drip water may also be stored for a specific time in the aquifer without further mixing. The resulting delay is referred to as the transmission time in the following, which can be determined by shifting the modelled δ^{18}O values until the maximum correlation with the monitoring data is obtained. For instance, a mixing time of 12 months and transmission time of 6 months means that the drip water represents a mixture of 12 months and is stored 18 months in total in the aquifer. The water of the most recent 6 months, however, does not contribute to the cave drip water. This may be considered as a mixed reservoir of water slowly travelling through the karst aquifer. The mixing time determines the size of the reservoir, and the transmission time defines its velocity. Thus, the degree of smoothing is solely determined

by the mixing time, whereas the transmission time only results in a delay of the drip water time series. The degree of smoothing (i.e., the number of contributing months, N), can be estimated by calculating the variability (i.e., the standard deviation) of the modelled drip water data set. In case of a reasonable value for N, the standard deviation of the modelled drip water δ^{18}O values and the monitoring drip water δ^{18}O data should be similar. A smaller standard deviation of the model data suggests too much smoothing, whereas a larger standard deviation suggests that the amount of mixing (i.e., N) has been underestimated.

2.3 Results

2.3.1 Cave monitoring

Figure 2.4 shows a comparison of rainfall amount, calculated potential evapo-transpiration and drip rate at the HL cave system for the period from November 2010 to November 2014. The rainfall amount is evenly distributed over the year and does not show a distinct seasonality. The drip rate, in contrast, shows a distinct seasonal pattern, with high drip rates during winter and low drip rates during summer. This pattern is clearly anti-correlated with the seasonal cycle of pET, showing high values during summer due to strong evaporation and the active vegetation. During winter, in contrast, pET is low due to weak evaporation and because the vegetation is mostly inactive. The observed pattern, thus, confirms that infiltration and recharge mainly occur during winter months. As a consequence, the cave drip water should mainly reflect the winter precipitation falling above the cave. Since the NAO is a winter phenomenon and the δ^{18}O values of winter precipitation in the study area are highly correlated with the NAOI, the δ^{18}O values of cave drip water should be a promising proxy for past NAO variability, if the δ^{18}O signal of precipitation is transferred into the cave.

As a first test of this hypothesis, we applied the drip water model to the corrected precipitation and rainfall δ^{18}O data from Frankfurt am Main (Fig. 2.2). This enables us to compare the drip water model with the measured δ^{18}O values of the cave drip water. We do not use the cave monitoring data for this comparison for two reasons: (1) rainfall δ^{18}O data at the cave site are not available for all months (Fig. 2.5). (2) rH is not available for the cave site. Figure 2.5 shows a comparison of the rainfall δ^{18}O values, the drip water δ^{18}O values and the modelled drip water δ^{18}O values using both the non-mixing and the mixing model assuming a mixing time of 12 months. The modelled δ^{18}O values are in very good agreement with the cave drip water δ^{18}O values. This shows that even our simple model yields realistic results for the HL cave system. It is also obvious that the drip water δ^{18}O values are more negative than the annual mean values of rainfall δ^{18}O. This suggests a higher contribution of winter precipitation to the drip water due to the effect of enhanced pET during summer.

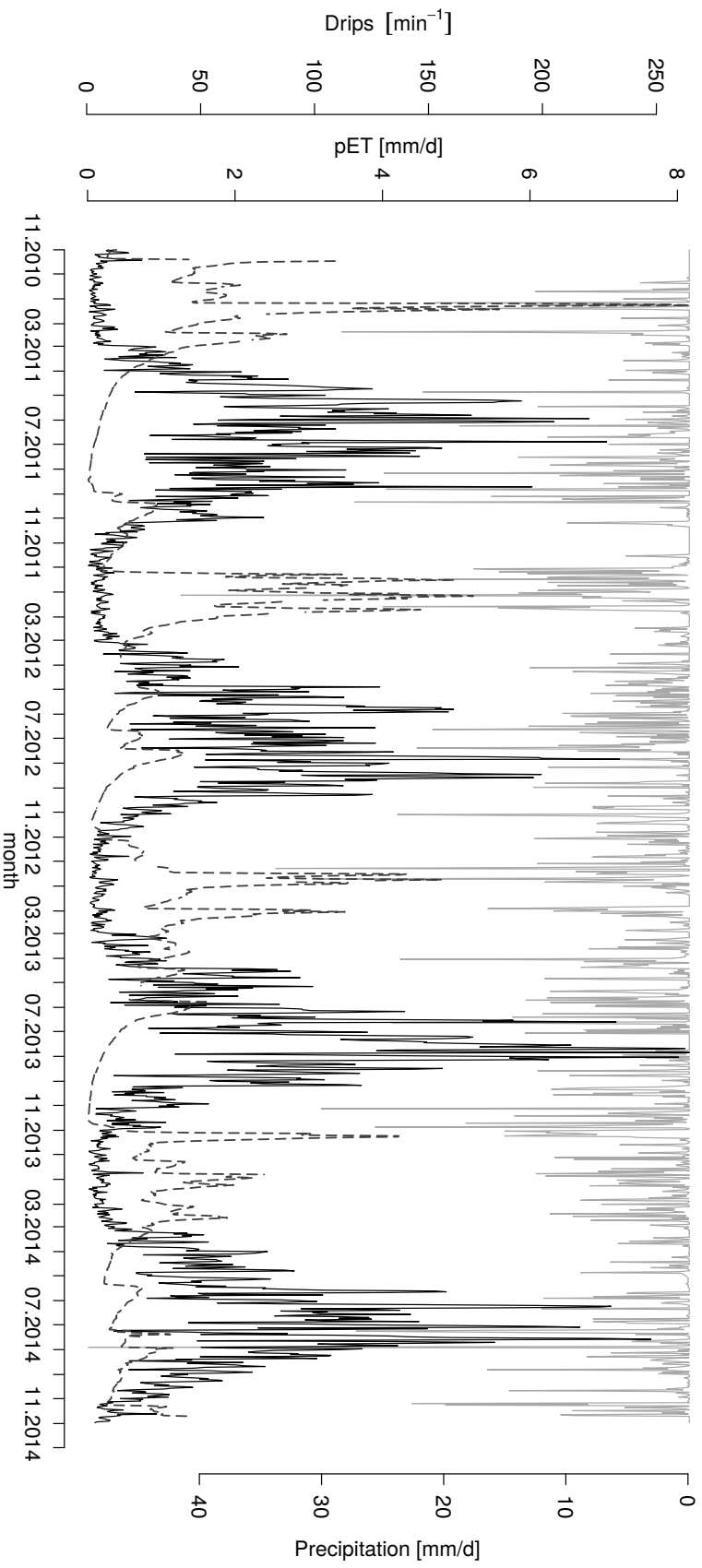

Figure 2.4: Comparison of precipitation (*light grey*, plotted on an inverted scale), calculated pET (*black*) and drip rate (*dashed line*) for 4 years at the HL. High drip rates occur during winter, whereas pET shows the highest values during winter months, indicating an active vegetation. Groundwater recharge, thus, mostly occurs during winter month

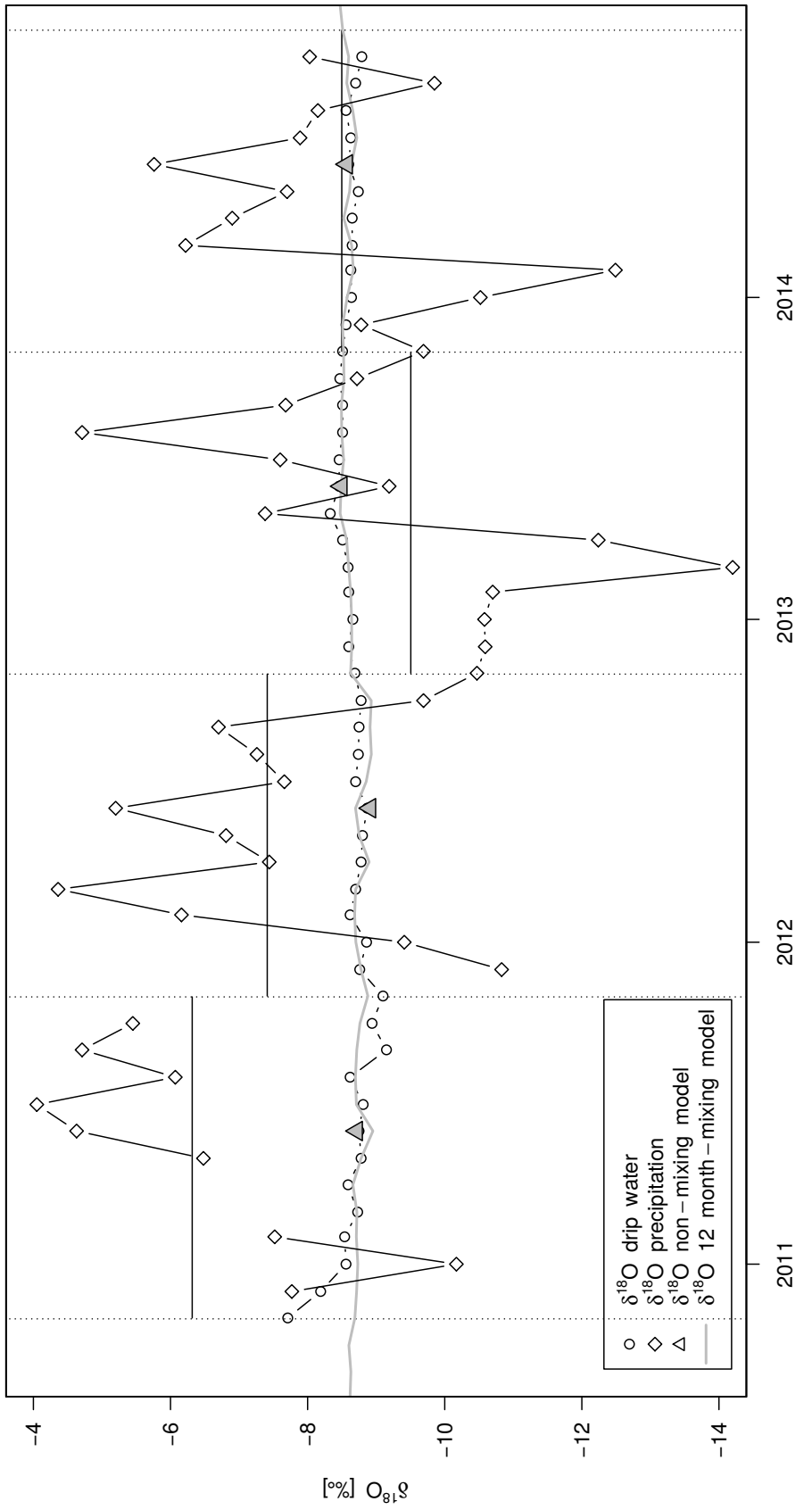

Figure 2.5: Comparison of rainfall $\delta^{18}O$ values at the HL cave system with measured and modelled drip water $\delta^{18}O$ values. The *grey line* shows the output of the 12 month-mixing model. They are in very good agreement. The *horizontal straight lines* show the mean $\delta^{18}O$ values of the precipitation of the individual years, *the vertical dotted lines* show the four hydrological cycles from November to September

Mixing in the aquifer generally leads to a lower variability of the δ^{18}O values of the drip water than of the δ^{18}O values of precipitation. Figure 2.6 shows a comparison of the drip water δ^{18}O values with the δ^{18}O values simulated using the mixing model. Assuming a mixing time of 12 months ($N = 12$), results in drip water δ^{18}O values are comparable to the non-mixing model. The standard deviation of the δ^{18}O values of the mixing model is 0.12 ‰, which compares well with the standard deviation of 0.15 ‰ of the monitored δ^{18}O values. This suggests a mixing time of about 12 months. In order to account for any delay due to transmission effects occurring in the karst aquifer, we calculated a lagged correlation between the mixing model and the measured cave drip water δ^{18}O values. The maximum correlation is observed for a transmission time of 10 months (Fig. 2.6). This suggests that the drip water at the HL cave system represents a mixture of about 12 months, and this mixed water then travels through the aquifer for about 10 additional months. This suggests a mixing time of about 12 months. In order to account for any delay due to transmission effects occurring in the karst aquifer, we calculated a lagged correlation between the mixing model and the measured cave drip water δ^{18}O values. The maximum correlation is observed for a transmission time of 10 months (Fig.2.6). This suggests that the drip water at the HL cave system represents a mixture of about 12 months, and this mixed water then travels through the aquifer for about 10 additional months.

2.3.2 Meteorological station data

For the winter season (DJFM), monthly mean temperature at the meteorological station Frankfurt am Main is significantly correlated with the NAOI (Spearman's rank correlation $r_s = 0.62$, $p < 0.01$, n = 144). During the other seasons (AMJJ and ASON), no significant correlations with the NAOI are observed. This confirms the strong influence of the NAO on winter temperature in the study area (e.g., Hurrell 1995; Baldini et al. 2008). The Spearman's rank correlation coefficients between the winter NAOI and the δ^{18}O value of winter precipitation are $r_s = 0.75$ ($p < 0.01$, n = 36) and $r_s = 0.63$ ($p < 0.01$, n = 32) for the GNIP stations Wasserkuppe/Rhön and Koblenz, respectively (supplemental Fig. 9). This confirms the results of Baldini et al. (2008), who used slightly shorter datasets and found $r_s = 0.68$ (n = 19) for Koblenz and $r_s = 0.80$ (n = 22) for Wasserkuppe/Rhön. The correlation between the δ^{18}O value of winter precipitation at the HL cave system is relatively high (0.41), but—due to the limited amount of data (n = 4)—not significant at the 99 %-confidence level.

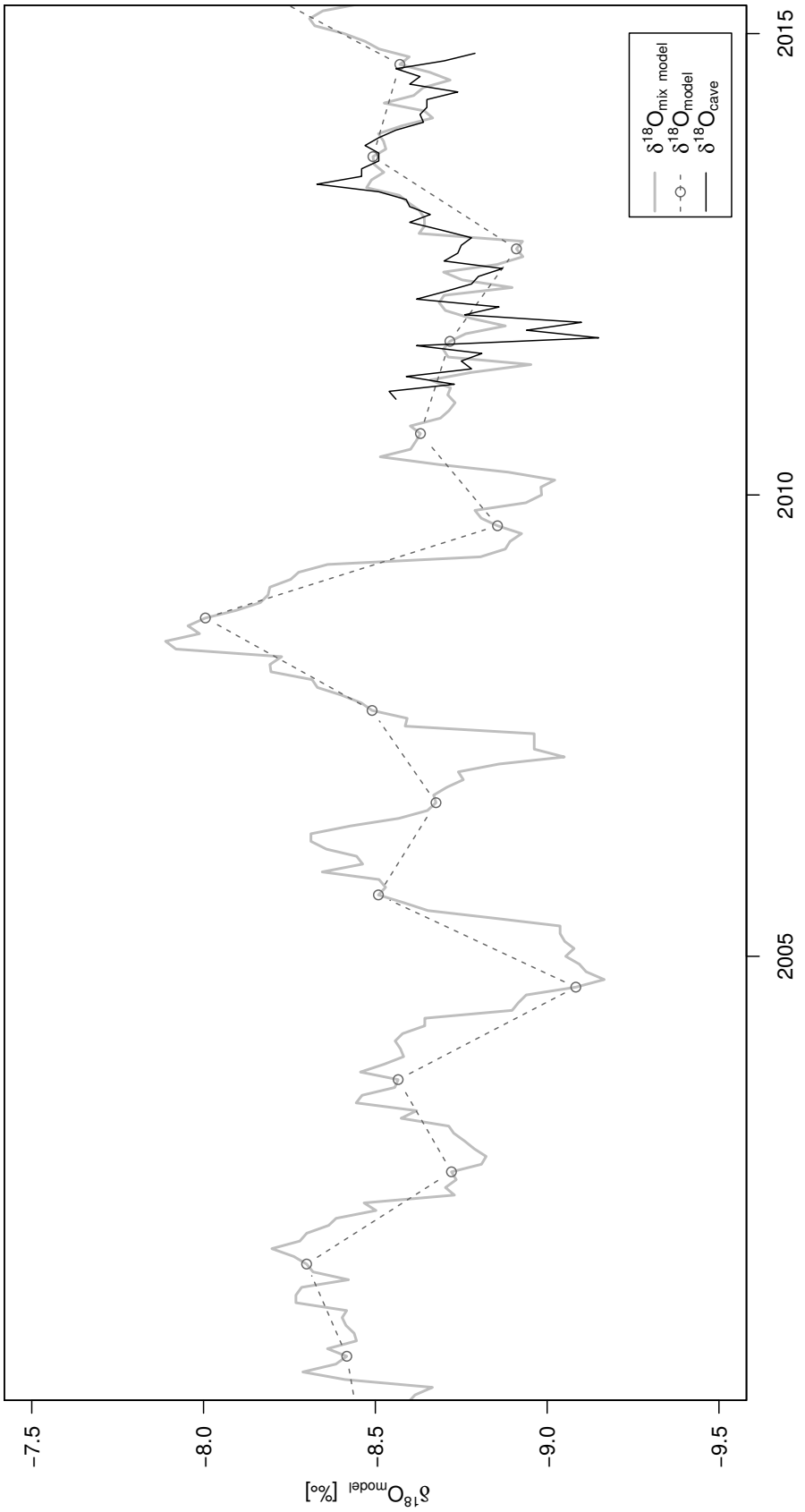

Figure 2.6: Comparison of the δ^{18}O values of the mixing model (assuming a mixing of 12 month), the non-mixing model and the measured δ^{18}O of the cave drip water. Assuming a transition time of 10 month results in the largest correlation of r = 0.69, p $<$ 0.01, with the δ^{18}O values of the cave drip water

2.3.3 Drip water model

As explained in Sect. 2.2.4, the δ^{18}O value of the cave drip water can be calculated using Eq. (2.5), based on the approach of Wackerbarth et al. (2010). The model is fed with the offset-corrected daily precipitation and T_{max} data from Frankfurt am Main (Fig. 2.2) and the extended data set for rH (supplemental Fig. 6). Furthermore, we use the extended rainfall δ^{18}O dataset for the HL cave system based on the observed linear relationship between rainfall δ^{18}O and temperature (Fig. 2.3). The modelled drip water δ^{18}O values for the period from 1870 to 2014 are shown in Fig. 2.7. Our modelled drip water δ^{18}O record shows a low, but significant correlation (r = 0.33, $p < 0.01$, n = 144) with the NAOI. For the same period, the correlation between the non-mixing model and the mixing model assuming a mixing time of 12 months is r = 0.78, $p < 0.01$, indicating a good agreement between both models (supplemental Fig. 7). Nevertheless, the correlation with the NAOI is a weaker for the mixing model (r = 0.14, $p = 0.09$).

In case of a longer residence time than assumed in our model, and consequently stronger mixing in the aquifer, the drip water may also reflect a mixture of several years (Genty et al. 2014). To investigate the effects of potential mixing in the epikarst, we use the mixing model and calculate the drip water δ^{18}O values assuming a mixing of 12, 36, and 96 months (Fig. 2.8). As expected, the drip water δ^{18}O values are getting progressively smoother for longer mixing times. As a result, the correlation with the NAOI weakens for increased mixing and no significant correlation with the NAOI is observed anymore. For a mixing time of 36 months, r = 0.03 ($p = 0.68$), for a mixing time of 96 months, r = -0.08 ($p = 0.34$).

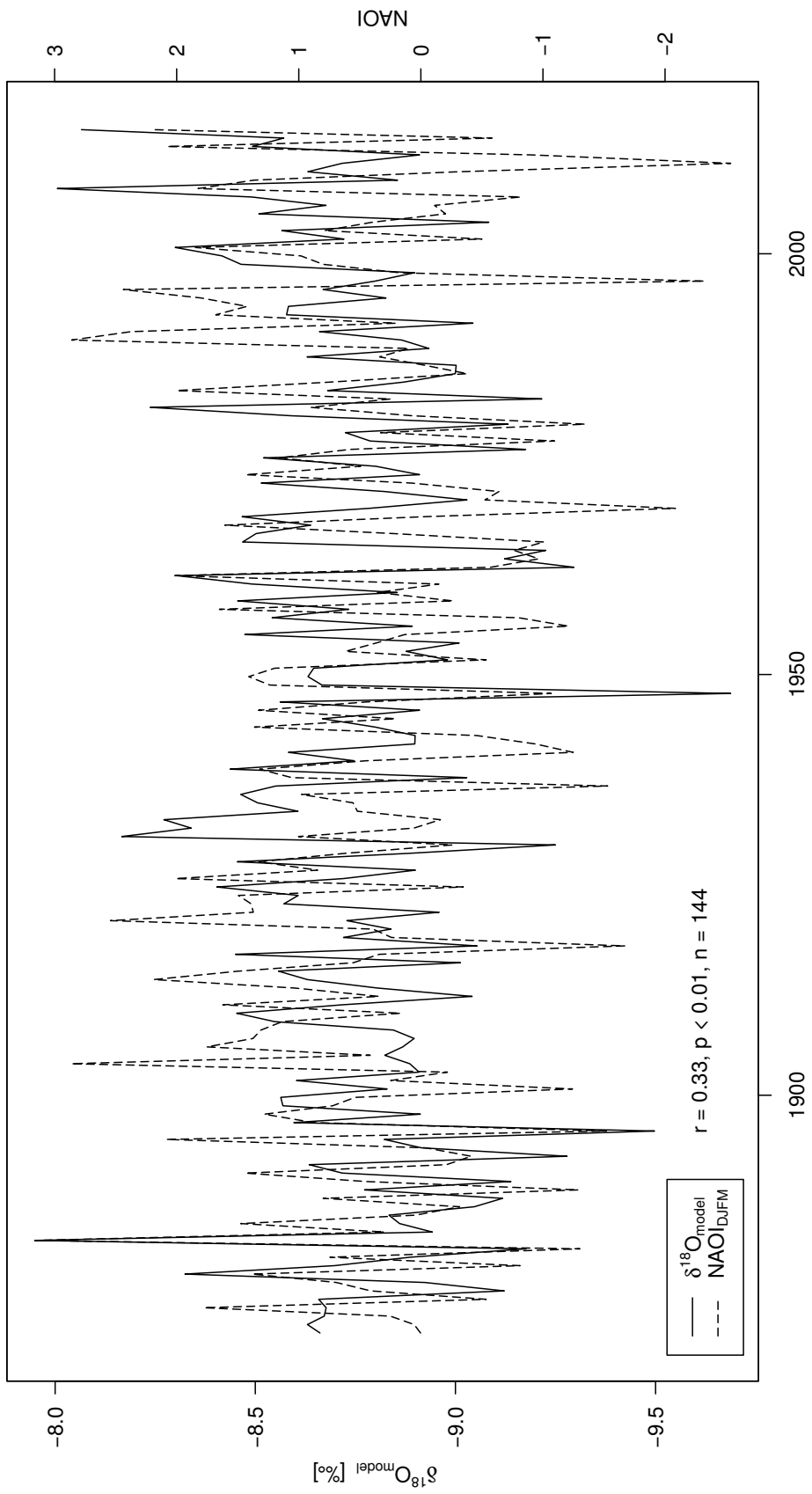

Figure 2.7: Comparison of the modelled $\delta^{18}O$ values (non-mixing model) of the cave drip water and the winter NAOI for the last 144 years. The two time series show a relatively low, but significant correlation of r = 0.33

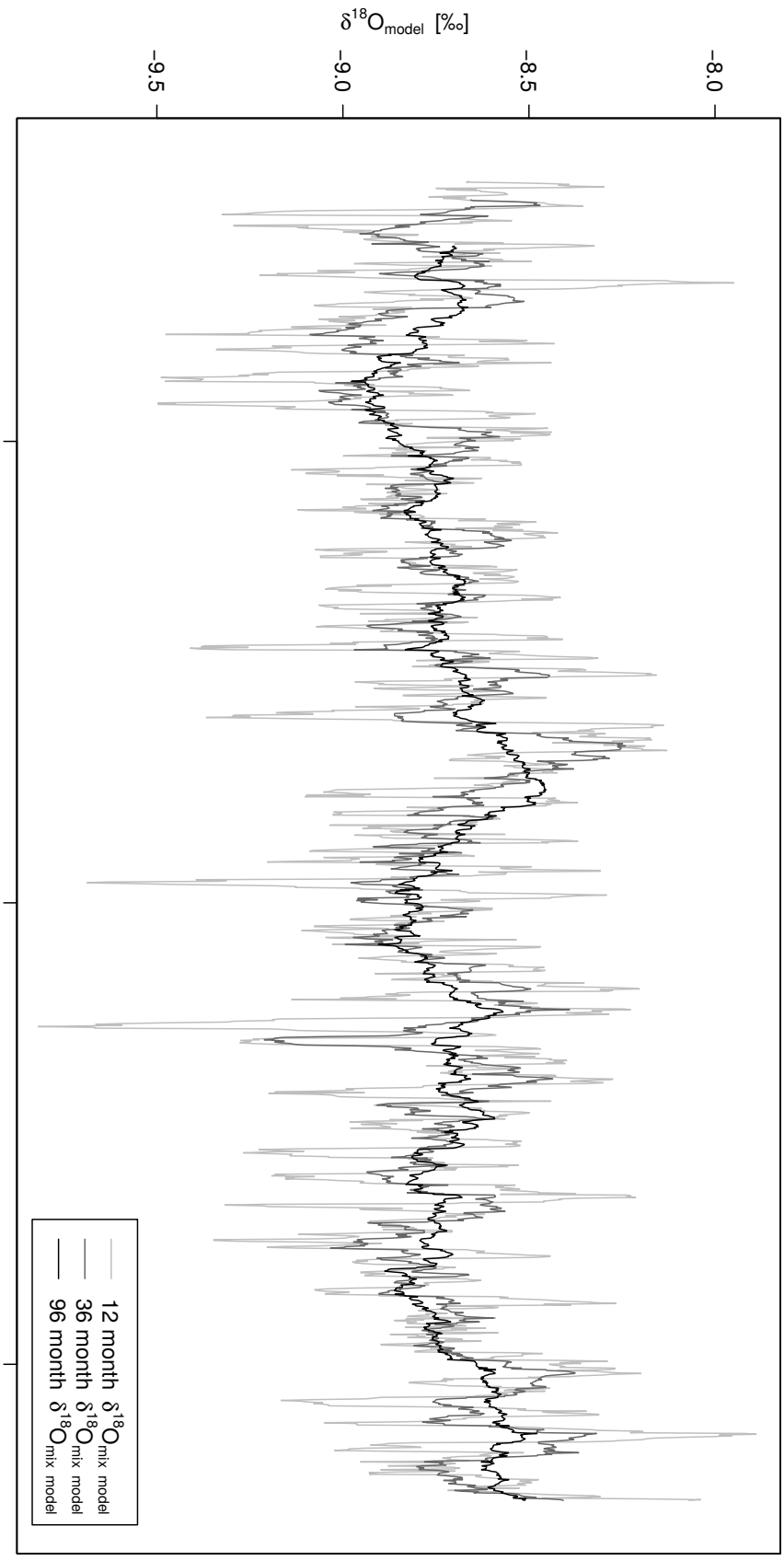

Figure 2.8: Comparing the modelled $\delta^{18}O$ values of the mixing model for the last 144 years assuming a mixing of 12, 36 and 96 month

2.4 Discussion

2.4.1 Effects influencing the relationship between the NAOI and the cave drip water δ^{18}O values

Several studies have used past changes in the NAO to explain the observed changes in speleothem δ^{18}O values (Mangini et al. 2005; Vollweiler et al. 2006; van Beynen et al. 2007; Wackerbarth et al. 2010; Langebroek et al. 2011; Fohlmeister et al. 2012; Kotlia et al. 2012; Scholz et al. 2012). The reasoning is in most cases as follows: the NAO is a winter phenomenon, which is reflected in the δ^{18}O values of winter precipitation at the cave site. Due to the strong seasonality of vegetation activity and, consequently, pET, the cave drip water mainly consists of winter precipitation. Thus, the δ^{18}O values of cave drip water and speleothem calcite reflect past changes in the NAO.

This is the first study attempting to quantitatively evaluate the potential of cave drip water δ^{18}O values for reconstructing the NAOI. As shown by Baldini et al. (2008), the GNIP stations Koblenz and Wasserkuppe/Rhön, which are surrounding the HL cave system (Fig. 2.1b), show the highest correlation between the δ^{18}O values of winter precipitation and the NAOI in Central Europe. This is confirmed by the corresponding correlation coefficients for the updated, longer data sets calculated in our study ($r_s = 0.68$ and $r_s = 0.79$, for Koblenz and Wasserkuppe/Rhön respectively). This is further corroborated by the high correlation coefficients between winter temperature and the winter NAOI for the other meteorological stations surrounding the cave (Fig. 2.1b; Table 2.2.2, (Baldini et al. 2008). The high drip rates during winter observed in our cave monitoring program confirm our calculations suggesting a high pET during summer and almost no pET during winter. Furthermore, this shows that most of the recharge at the HL cave system occurs during winter. Another explanation for the observed drip rate seasonality is related to hydrological pressure. Deeper roots of large trees may extract water from a reservoir several meters below the surface instead of using the most recent precipitation. These trees would, thus, not affect transpiration above the cave, allowing precipitation of all seasons to infiltrate the karst aquifer. Since vegetation is less active during winter, these trees would withdraw more water from the deeper reservoir during summer than during winter. This would result in an increased hydrological pressure and higher drip rates during winter. Nevertheless, the reservoir would be fed by the precipitation throughout the year rather than mainly by winter precipitation in this case. However, due to the very good agreement between the modelled and the monitored drip water δ^{18}O values (Fig. 2.5) this explanation is unlikely for the HL. Thus, at the HL, the drip water should mainly consist of winter precipitation, and the cave system should be an ideal site for an NAO reconstruction based on speleothem δ^{18}O values.

We also evaluated the effect of using different k values in Eq. (2.2). As explained in Sect. 2.2.4, the vegetation above the HL cave system is patchy and consists of forest as well

as meadow. Therefore, we used two different k values (for meadow and forest, respectively) for our calculations and calculated the pET using the average of both k values. In order to quantify the effect of the k value, we also calculated pET using the individual k values for meadow and forest, respectively. The resulting correlation between modelled drip water $\delta^{18}O$ and the NAO index is 0.34 and 0.31, respectively, which is very similar to the result using the mean k values (r = 0.33). This shows that the sensitivity of our model to the k value is relatively low.

On this basis, the relatively low correlation coefficient of r = 0.33 between the modelled cave drip water $\delta^{18}O$ values and the winter NAOI is surprising. The model documents an influence of the NAO on cave drip water $\delta^{18}O$ values, but on a relatively low level only (the explained variance is ca. 10 %). This low correlation coefficient may—at least partly—be related to the assumptions used for the model. Since no long-term monitoring dataset is available from the cave site, we had to resort to climate data (amount of precipitation, T_{max} and rH) from the nearby station Frankfurt am Main. In particular for precipitation, the correlation between the HL cave system and Frankfurt am Main dataset is relatively low (r = 0.43). Furthermore, in order to extend the datasets of rH and rainfall $\delta^{18}O$ back to 1870 AD, we had to perform linear regressions and attribute their variability to changes in temperature. The relationship between rainfall $\delta^{18}O$ and temperature at the HL cave system is in good agreement with that at the two nearby GNIP stations Koblenz and Wasserkuppe/Rhön supporting our approach. Nevertheless, all these assumptions are, of course, simplifications, which may affect the observed relationship between cave drip water $\delta^{18}O$ values and the winter NAOI.

In order to quantify the effect of this simplification, we also used the GNIP data set from Wasserkuppe/Rhön to model the $\delta^{18}O$ values of the drip water. To account for local climatic differences between the HL cave site and Wasserkuppe/Rhön, we used linear regression models (Fig. 2.9). Afterwards, the drip water model was fed with the cave site-corrected values. Due to the fact, that the GNIP Wasserkuppe/Rhön data set is only 36 years long, the modelled drip water $\delta^{18}O$ data set also contains 36 years only. The correlation with the NAOI (DJFM) is slightly higher than for our initial approach ($r_s = 0.5$, $p < 0.01$, n = 36, Fig. 2.10) suggesting that the lower correlation obtained using the temperature relationship may—at least partly—result from this simplification. However, for the alternative approach, the NAO still only explains 25 % of the observed variance of the drip water.

Another crucial factor influencing the observed relationship is the composition of the recharge water and, consequently, also the cave drip water. As outlined above and confirmed by our calculations, winter rainfall is the major component of the cave drip water. However, even if a large part of the precipitation falling during the other seasons does not reach the cave due to enhanced pET, this contribution is not negligible. Figure 2.11 shows the relative contribution of the individual months to the cave drip water for the corresponding hydrological cycle based on our long modelled drip water $\delta^{18}O$ data set using the data from Frankfurt am Main (Fig. 2.7). On average, more than 50 % of the recharge occurs between November and

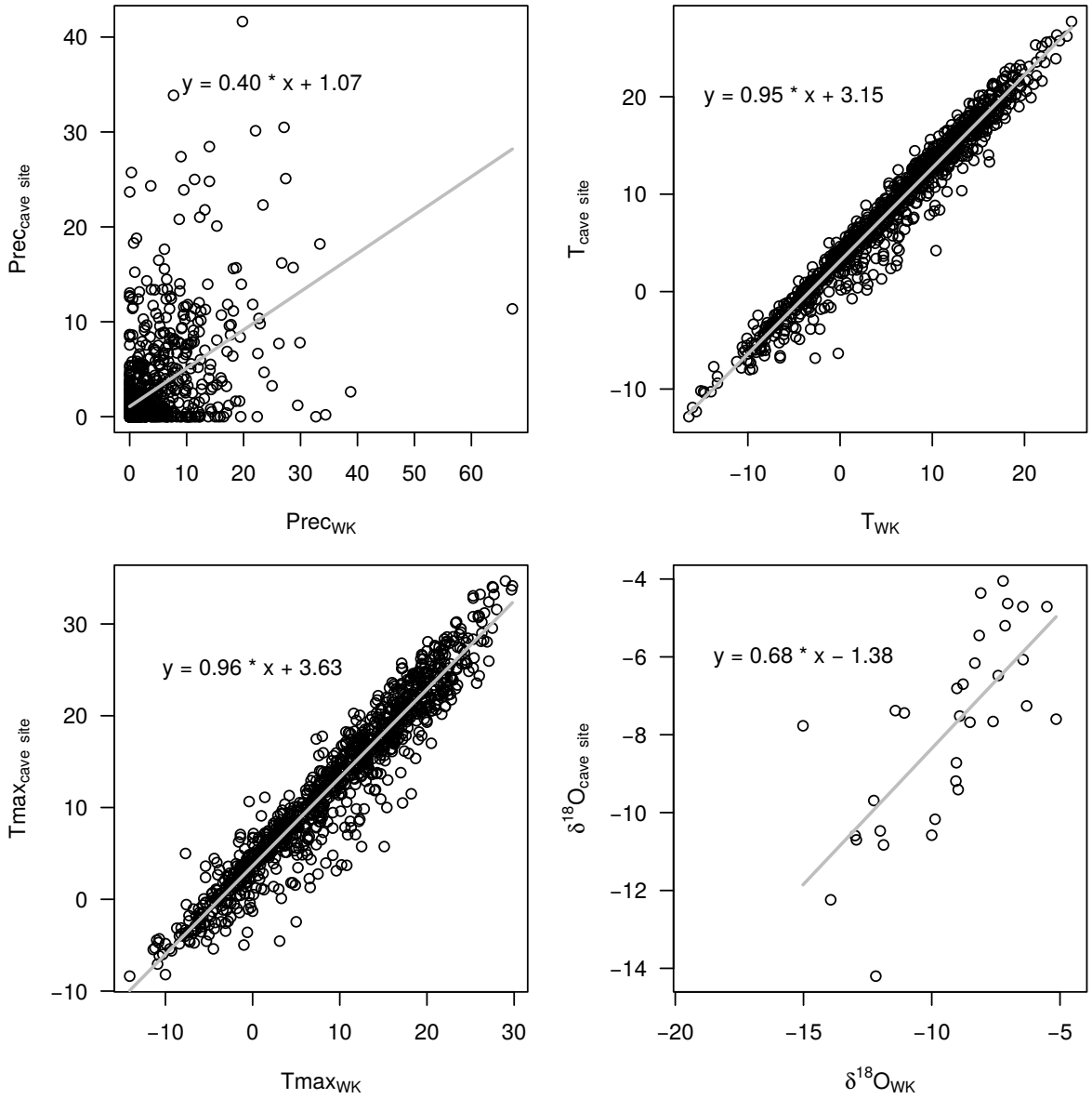

Figure 2.9: Linear regression models for all releveant climate parameters between Wasserkuppe/Rhön (WK) and the HL cave site. Precipitation, temperature and maximum temperature are daily values from 2010 to 2014, δ^{18}O values are monthly data from 2010 to 2013.

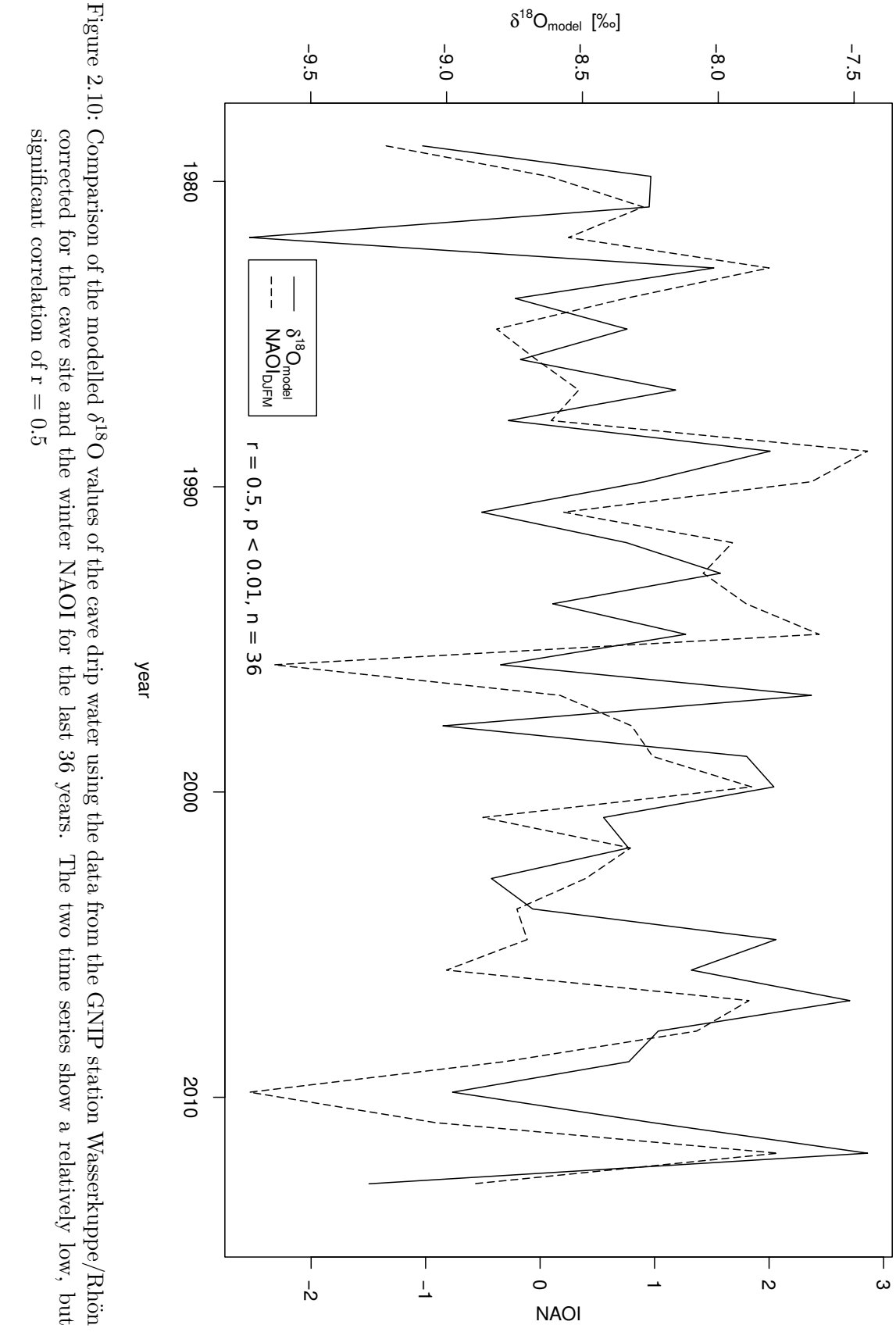

Figure 2.10: Comparison of the modelled $\delta^{18}O$ values of the cave drip water using the data from the GNIP station Wasserkuppe/Rhön corrected for the cave site and the winter NAOI for the last 36 years. The two time series show a relatively low, but significant correlation of r = 0.5

March. However, the rest of the year, on average, contributes up to 40 % to the recharge water showing that these months are also relevant for the annual budget. In case of strong precipitation events during summer months, such as during thunder storms, the contribution of these months may be even larger than 20 %. In this case, the more positive δ^{18}O values of summer precipitation represent a substantial contribution to the recharge water. As a consequence, the δ^{18}O values of the drip water are biased towards more positive values and do not show a pure winter signal. This effect, thus, may substantially weaken the NAO signal in the cave drip water.

In order to quantify this effect, we fed the drip water model with winter precipitation (DJFM) only (i.e., assuming that the contribution of all other months is effectively zero). In this case, we find a correlation coefficient between drip water δ^{18}O and the NAOI of r = 0.53. This value can be interpreted as the maximum value, which can be obtained using our model approach. This is also reflected by the good agreement of this value with the correlation coefficient between the δ^{18}O value of winter precipitation at the GNIP station Koblenz and the winter NAOI (r = 0.51). This scenario, thus, represents an ideal case, where the drip water only consists of winter precipitation.

In contrast to Wackerbarth et al. (2010), our model does not consider potential isotope fractionation occurring during evaporation. Wackerbarth et al. (2010) assumed that between 20 and 50 % of the water lost by evapo-transpiration are lost due to soil evaporation and accounted for the corresponding isotope fractionation using a Rayleigh fractionation model. However, several studies have shown that the fraction of precipitation lost by evaporation is much smaller (between ca. 10 and 30 %, (Sutanto et al. 2012; Lawrence et al. 2007). Furthermore, the evaporative effect is most pronounced in the upper 20 cm of the soil and compensated by downward diffusion process (Sutanto et al. 2012). Furthermore, heavy rainfall events may replenish all water inside the soil pores. Thus, the effect on the δ^{18}O value of the soil water is low. Therefore, in summary, isotope fractionation occurring during evaporation may only have a small effect on the δ^{18}O value of the infiltrating water and can reasonably be neglected. This is also confirmed by the very good agreement between our modelled and monitored cave drip water δ^{18}O values (Fig. 2.5).

In summary, cave drip water δ^{18}O values in central Germany do reflect past changes in the NAO due to (1) the seasonal effect of vegetation activity influencing pET, and (2) the correlation of winter rainfall δ^{18}O values in the area with the winter NAOI. However, due to the highly variable contribution of precipitation during the remaining months to the drip water, the relationship is significantly weakened.

2.4.2 Implications for NAO reconstructions based on speleothem δ^{18}O values

The longest currently available reconstruction of the NAOI extends back to 5.2 ka and is based on a lake sediment record from south-western Greenland (Olsen et al. 2012). Speleothems

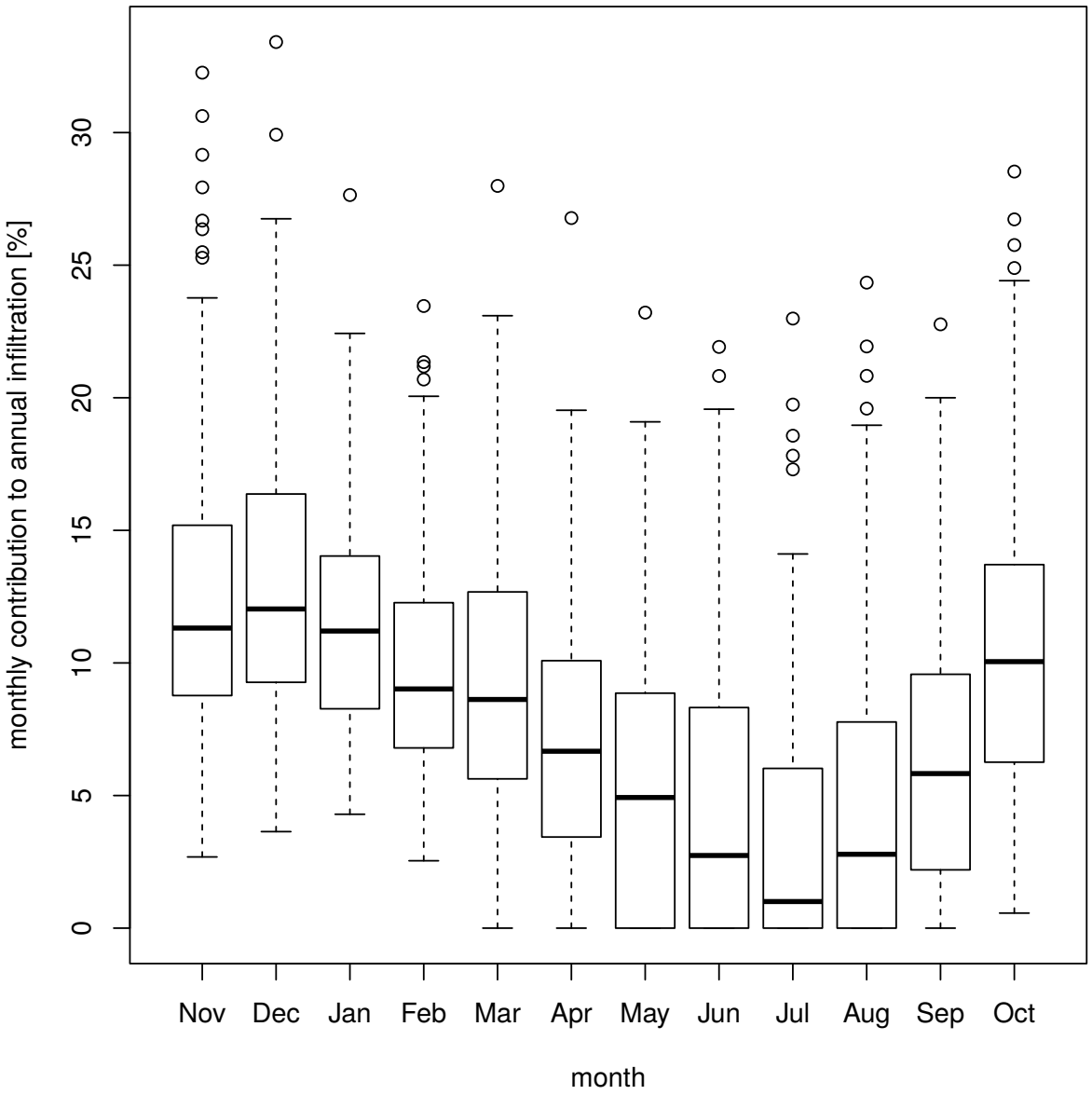

Figure 2.11: Boxplots of the monthly contribution to the annual infiltration for the last 144 years

can be precisely dated by U-series methods and provide long, continuous proxy records. For this reason and since they record the $\delta^{18}O$ value of the precipitation falling above the cave, they are considered to have high potential for NAO reconstructions (Mangini et al. 2005; Wackerbarth et al. 2010; Langebroek et al. 2011; Fohlmeister et al. 2012; Wassenburg et al. 2013).

The HL cave system is located in one of the most sensitive regions affected by the NAO (Baldini et al. 2008), and its positive and negative state, respectively, are clearly reflected in the $\delta^{18}O$ values of local winter precipitation. Therefore, past NAO variability should be recorded in the $\delta^{18}O$ values of stalagmites from the HL cave system, even if the relationship between the NAO and winter climate may have been temporally unstable (Casty et al. 2005). However, as shown by our study, the NAO signal in the cave drip water may be substantially biased by the variable contribution of summer precipitation. It is, thus, very unlikely that the stalagmites only record winter precipitation, and they probably rather show a mixed signal consisting mainly of winter precipitation, but to a variable extent, also of summer precipitation.

For an NAO reconstruction based on speleothems, further complications arise. Firstly, a variety of studies has demonstrated that speleothem calcite is not necessarily precipitated in stable oxygen isotope equilibrium with the drip water (Mickler et al. 2006; Day and Henderson 2011; Tremaine et al. 2011; Kluge et al. 2013; Riechelmann et al. 2013). Since the degree of disequilibrium is modulated by the drip rate (Mühlinghaus et al. 2009; Riechelmann et al. 2013), which is variable with time, these effects may further bias the NAO signal of the drip water. Secondly, the NAO does not only affect the $\delta^{18}O$ values of local precipitation, but also temperature, with both higher $\delta^{18}O$ values and temperatures corresponding to a positive NAOI. Due to the relatively large overburden, surface temperature changes are only slowly transferred into caves (Domínguez-Villar et al. 2015). Since the NAO is an inter-annual phenomenon, the related temperature changes are, thus, unlikely to have a strong effect on cave temperature. However, if the temperature effect would be observed inside a cave, the effect on the $\delta^{18}O$ values of speleothem calcite would be opposite to those of the drip water $\delta^{18}O$ values due to the negative relationship between temperature and speleothem calcite $\delta^{18}O$ values resulting from the stable isotope fractionation during precipitation of calcite (Mühlinghaus et al. 2009; Tremaine et al. 2011). The temperature effect would, thus, further weaken the potential NAO signal contained in the drip wated $\delta^{18}O$ values. Thirdly, the growth rate of speleothems may be low (<50 µm/a). Thus, sampling at annual resolution, as would be ideal for reconstruction of an interannual phenomenon such as the NAO, is not possible for all speleothems. Fourthly, speleothem growth rates may be highly variable with time (Scholz and Hoffmann 2011). Stable isotope sampling at equidistant spatial resolution would, thus, result in a non-equidistant time series or, even worse, variable mixing of calcite precipitated during different years. Fifthly, many speleothems have a relatively low U content, which makes precise U-series dating of Holocene samples challenging. The time scale of the $\delta^{18}O$

time series may then be associated with substantial uncertainty. Finally, the environmental conditions above the cave may have been different in the past. For instance, the vegetation cover above the cave may change substantially throughout the Holocene, both due to climatic and anthropogenic reasons. Soil properties may also change substantially with time as has been shown, for instance, by speleothem $\delta^{13}C$ values (Scholz et al. 2012). Both processes would have an effect on evapo-transpiration and, thus, also on infiltration and the relationship between drip water $\delta^{18}O$ and the NAO. Such temporally variable effects further complicate a reconstruction of the NAO based on speleothem $\delta^{18}O$ values.

Taking all these possible factors into account and considering that the drip water signal itself may be complex, it is not too surprising that NOAI reconstructions based on speleothem $\delta^{18}O$ data have to be approached with caution. An exception may be annually laminated samples, whose chronologies are robust.

The application of additional proxies, such as trace elements (Wassenburg et al. 2013), can support the interpretation of speleothem $\delta^{18}O$ signals in terms of past NAO variability. These can be measured at higher resolution than stable isotope signals (Jochum et al. 2012) and may provide important insights into the processes occurring in the karst aquifer and during formation of speleothems.

2.5 Conclusions

We have presented a 4-year, monthly resolved monitoring data set for the HL cave system, which is located in a highly sensitive region for the NAO. Application of an infiltration model to account for mixing effects occurring in the karst aquifer shows a very good agreement with the monitoring data and suggests a mean residence time of 12 months and a transmission time of 10 months. Using these parameters, we have modelled the $\delta^{18}O$ values of cave drip water for the last 144 years in the HL cave system. Although the drip water mainly consists of winter precipitation and winter rainfall $\delta^{18}O$ values show a high correlation with the winter NAOI, the modelled drip water $\delta^{18}O$ time series only shows a moderate correlation with the winter NAOI. The major reason for this low correlation is the substantial contribution of precipitation from the other seasons to the drip water, for instance, due to heavy precipitation events in summer. These rainfall events weaken the winter-biased NAO signal recorded in the drip water $\delta^{18}O$ values.

Reconstruction of the NAOI using speleothems, thus, remains challenging in particular considering additional factors, such as chronological uncertainties and calcite precipitation deviating from isotopic equilibrium. These issues may, at least in part, be avoided by multi-proxy studies of annually laminated stalagmites.

Acknowledgments

We thank two anonymous reviewers for there constructive and thorough reviews and Jean-Claude Duplessy for editorial handling. Denis Scholz and Simon A. Mischel thank the Deutsche Forschungsgemeinschaft (DFG) for funding (SCHO1274/3- 1). We are also thankful to the Verband der deutschen Höhlen- und Karstforscher e.V. for funding CORA and the Landesverband für Höhlen- und Karstforschung HESSEN e.V. for providing a temperature logger. We gratefully thank the people at IAEA and especially Stefan Terzer for providing an updated GNIP data set. Finally, we also thank the local caving club Speläologische Arbeitsgemeinschaft Hessen e.V. at the Herbstlabyrinth for support.

3 Holocene climate variability in central Germany and a potential link to the polar North Atlantic - a replicated record from three coeval speleothems

Simon A. Mischel · Denis Scholz · Christoph Spötl · Klaus Peter Jochum · Andrea Schröder-Ritzrau · Sabine Fiedler

Abstract

Here we present high-resolution trace element and stable isotope records from three coeval Holocene stalagmites from the Herbstlabyrinth cave system, central Germany. All stalagmites were precisely dated using MC-ICPMS ^{230}Th\U-dating. One stalagmite started to grow at 13.62 ± 0.13 ka BP, covering the Late Glacial, the other two speleothems started to grow at 11.13 ± 0.08 and 10.26 ± 0.08 ka BP, respectively. The combined record covers the entire Holocene. The interpretation of the different climate proxies is supported by data from a detailed cave monitoring program. Cold conditions during the Younger Dryas are reflected by intermittent stalagmite growth at the Herbstlabyrinth. The δ^{18}O records are in general agreement with the NGRIP δ^{18}O record on millennial time scales indicating that speleothem δ^{18}O values at the Herbstlabyrinth reflect large-scale climate variability in the North Atlantic area. The 8.2 ka event is clearly visible as a pronounced negative excursion in the δ^{18}O records. In all other proxies, it is not reflected as a major excursion. Correlation and principal component analysis enables us to disentangle the various processes affecting the stable isotope and trace element signals. Phases with higher P, Ba and U concentrations and more negative δ^{13}C values are interpreted as reflecting more productive vegetation above the cave. The negative correlation of Mg with P, Ba and U and the positive correlation with δ^{13}C indicate more recharge during phases of more productive vegetation, probably due to increased rainfall. The majority of the observed phases of reduced vegetation productivity and drier climate coincide with cooler periods in the polar North Atlantic as reflected by a higher abundance of hematite-stained grains (i.e., the Bond events) suggesting a close relationship between terrestrial climate in central Europe and the polar North Atlantic.

Keywords: Speleothem · Holocene · trace element · stable isotope · cave monitoring · U-series dating

3.1 Introduction

Speleothems offer a variety of advantages as climate archives and are increasingly used for paleoclimate studies (Lauritzen and Lundberg 1999; Henderson 2006). One of their advantages is that they occur on all continents except Antarctica (Ford and Williams 2007), at a variety of latitudes and longitudes as well as altitudes (Spötl and Mangini 2007). Using the ^{230}Th\U disequilibrium method, speleothems can be dated with exceptional accuracy and precision up to an age of about half a million years (Richards and Dorale 2003; Scholz and Hoffmann 2008; Cheng et al. 2000). The most widely used paleoclimate proxies in speleothems are stable carbon and oxygen isotopes (e.g., Asrat et al. 2007; Spötl and Mangini 2007; Mattey et al. 2008; Meyer et al. 2008; Spötl et al. 2008; Baker et al. 2011). Another group of widely used climate proxies are trace elements, which provide insights into the karst hydrology (Ayalon et al. 1999; Roberts et al. 1998; 1999; Finch et al. 2003; Treble et al. 2003; McMillan et al. 2005; Fairchild and McMillan 2007; van Beynen et al. 2008; Zhou, Chi, Lawrence, Zhao, Yan, Greig and Feng 2008; Zhou, Wang, Zhao, Zheng, Guan, Feng and Greig 2008), soil and vegetation characteristics (Hellstrom and McCulloch 2000; Huang et al. 2001) and may allow detection of anthropogenic impact in the catchment (Verheyden 2004; Fairchild and Treble 2009; Labuhn et al. 2015).

Here we present stable isotope and trace element data from three Late Glacial and Holocene stalagmites from the Herbstlabyrinth (HL) cave system, central Germany, and use data from an extensive cave monitoring program to support the interpretation in terms of past climate change. This study aims towards a better understanding of terrestrial climate variability in central Europe during the Late Glacial and the Holocene and in particular its relationship with the polar North Atlantic.

The Late Glacial (i.e., the transition period between fully glacial and interglacial conditions, from 19 to 11.5 ka BP (thousands of years before 1950)), is characterized by large climate oscillations at both global and regional scales (Litt et al. 2003). Here we focus on the Northern Hemisphere and in particular central Europe. The δ^{18}O record of the NGRIP ice core from central Greenland shows warmer climate conditions during the Bølling (14.64-14.03 ka BP) and a progressive cooling towards the end of the Allerød (14.03-12.85 ka BP). These time intervals were also characterized by several rapid oscillations from warmer to cooler conditions (Rasmussen et al. 2006). Between 14.45 and 13.35 ka BP, the vegetation in central Europe changed from Arctic steppe tundra to open woodland with birch trees (Litt and Stebich 1999). The onset of the Younger Dryas (12.85 $\pm$ 0.13 ka BP; Rasmussen et al. 2006) was characterized by rapid cooling (Litt et al. 2003) lasting until 11.65 $\pm$ 0.1 ka BP (Vinther et al. 2006). Litt et al. (2003) suggested a subdivision of the Younger Dryas into a first part which was relatively wet and cold, followed by a second part which was drier and warmer. During the Younger Dryas, the steppe tundra vegetation in central Europe returned for more than 1 ka (Litt and Stebich 1999). The focus of this study is on the Holocene, which started at the

end of the Younger Dryas at 11.65 ka BP (Vinther et al. 2006). This boundary is clearly visible in the NGRIP ice core by a rapid shift towards more positive δ^{18}O values and similar shifts in deuterium excess and dust content, which occurred within ca. 3 years (Steffensen et al. 2008; Walker et al. 2009). This shift is interpreted as a change in atmospheric circulation, which was accompanied by a temperature change of 10 ± 4 °C in Greenland (Walker et al. 2009). In addition, sea-surface temperatures in the source region of Arctic precipitation declined by ca. 2-4 °C, due to the reorganization of the Northern Hemispheric atmospheric circulation, shifting from the warmer mid-Atlantic during glacial times to colder high latitudes in the early Holocene (Walker et al. 2009). During the last 8 ka, the δ^{18}O values of the NGRIP ice core show relatively low variability, except for three prominent events: the 8.2 ka and the 9.3 ka events and the Preboreal Oscillation at 11.4 ka (Vinther et al. 2006). During the 8.2 ak event, January temperatures in central Europe were lower than today, but the effect on the vegetation was not as pronounced as for instance in Scandinavia (Seppa et al. 2007; Litt et al. 2009). In contrast to the relatively stable conditions suggested by the δ^{18}O values of the NGRIP ice core, various other studies suggest substantial climate variability during the Holocene. For instance, Bond et al. (1997; 2001) found cycles in the abundance of ice-rafted debris (IRD) in deep-sea sediments from the sub-polar North Atlantic which are occurring approximately every 1.5 ka. They interpreted these maxima in IRD as colder phases caused by a reorganization of ocean currents in the North Atlantic. Reconstructed July temperatures in central Germany during the Early Holocene (around 9 ka BP) are comparable to present-day temperatures, whereas January temperatures were between 2 and 10 °C colder than today (Litt et al. 2009). In addition, climate became progressively wetter during the Holocene (Litt et al. 2009). During the Holocene climate optimum (between about 8.5 and 5 ka BP), July temperatures in central Europe were ca. 1 °C warmer than today. The mid-Holocene climate optimum peaked at 6.7-6 ka BP (Davis et al. 2003; Litt et al. 2009). Subsequently, during the Late Holocene, summer temperatures declined again, whereas winter temperatures progressively increased (Davis et al. 2003). Litt et al. (2009) found high variability in January temperatures and precipitation in central Germany around 5 ka BP. Prior to 6 ka BP, the pollen records show a natural succession of vegetation controlled by the development of soil, climate and competition of trees (Litt et al. 2009). Human impact is visible in central Europe since ca. 7 ka BP and is mainly indicated by the decreasing abundance of forest indicators (arboreal pollen) and the increasing abundance of herb pollen suggesting more open habitats (Litt et al. 2009). This strong land-use continues until today with regional differences depending on the fertility of soils (Litt et al. 2009).

3.2 Materials and Methods

3.2.1 The Herbstlabyrinth cave system

The Herbstlabyrinth (HL) cave system developed in Devonian limestone in an area bordered by Tertiary volcanic rocks. The limestone area is 3 km^2 large and lies in the Rhenish Slate Mountains, central Germany, at an elevation of 435 m ASL (Supplemental Figure B.1). The HL has a total length of more than 9 km established on four levels (Supplemental Figure B.1). The upper three levels are well decorated with different kinds of actively growing as well as inactive speleothems including flowstones, stalagmites, stalactites and helictites. Large passages alternate with passages characterized by breakdown. The lowest level is hydrologically active. The mean annual temperature at the cave site is 9.0 °C, and the mean annual cave air temperature is slightly higher at the monitoring site (9.2 °C) (Mischel et al. 2015). Mean annual precipitation is around 800 mm^{-1}, and rainfall is evenly distributed throughout the year. Since 2010, a cave monitoring program (see below for details) has been set up in a natural small chamber right next to the show cave, which opened in 2009. Building of the show cave introduced an artificial tunnel entrance, which is sealed by doors to prevent exchange with the outside air. By comparing the 4-year cave monitoring data set with meteorological climate station data, Mischel et al. (2015) used $\delta^{18}O$ values to state that substantial mixing occurs in the epikarst above the cave. Model results suggest that the drip water represents a mixture of the water infiltrating within ca. 12 months and a mean residence time in the aquifer of about 10 months (Mischel et al. 2015). The effect of this mixing is a smoothed $\delta^{18}O$ signal of the drip water. This effect also results in an alteration of winter climate patterns, such as the North Atlantic Oscillation, due to significant contribution of summer precipitation to the drip water (Mischel et al. 2015).

3.2.2 Stalagmite samples

Stalagmite NG01 (Supplemental Figures B.2A and B.3A) is 50 cm long and has a diameter of ca. 15 cm. It was sampled in the Nordgang passage of the cave prior to the destruction of this passage in 2008 by the mining activities of the nearby quarry (Supplemental Figure B.1B). NG01 has no visible growth layers, and the stalagmite appears opaque and milky. Furthermore, NG01 does not contain any visible hiatuses or changes in the direction of the growth axis. The stalagmite grew on top of a thick sediment layer. Recently, the fatty acid concentration of NG01 has been studied, which suggested that this stalagmite records paleoenvironmental changes (Bosle et al. 2014).

Stalagmite HLK2 (Supplemental Figures B.2B and B.3B) is 15 cm long and grew in a small chamber about 30 m below the surface (Kleine Kammer, Supplemental Figure1 B.1C) adjacent to the show cave. At 13.5 cm distance from the top, the stalagmite contains a prominent clay layer (black arrow in Supplemental Figure B.3B). Above this layer, HLK2 is composed

of opaque, milky calcite, which becomes clearer and more transparent towards the top. The direction of the growth axis changes partially, probably because the stalagmite grew on an unstable substrate (Supplemental Figure B.3B). The stalagmite formed beneath a 60 cm-long stalactite, which was accidentally broken during the recovery of HLK2. The surface of the stalagmite was wet, suggesting active growth during the time of sampling in 2010 (Supplemental Figure B.2B). The cave monitoring program (e.g. drip water sampling site, location of the loggers) was set up in proximity to this stalagmite. Stalagmite TV1 (Supplemental Figures B.2C and B.3C) was removed in 2013 from the Traverse room (Supplemental Figure B.1B). TV1 is 15 cm long and has a similar shape as HLK2 (Supplemental Figures B.2C and B.2C). The stalagmite is transparent and clear, with macroscopically visible crystals. As NG01, TV1 does not have any visible hiatuses or changes in the direction of growth. The drip site feeding the stalagmite was actively dripping when TV1 was removed. In addition to the speleothems, two host rock samples were retrieved from the surface in order to compare their isotopic composition and trace element content to that of the speleothems. The samples were randomly chosen.

3.2.3 Analytical methods

All samples for ^{230}Th\U-dating were cut from the growth axis of the speleothems using a diamond wire saw. The average sample mass was approximately 0.3 g. After brief leaching in weak HNO_3 in order to remove surface contamination, chemical separation of U and Th isotopes was performed as described by Yang et al. (2015). Uranium and Th isotopes were measured using a MC-ICP-MS (Nu Plasma). In order to obtain correction factors for instrumental biases, such as mass fractionation and ion counter gain, a standard-bracketing method was applied. Details are provided by Scholz et al. (2014) and Obert et al. (2016). To account for the potential effects of detrital contamination, all ages were corrected assuming an average upper continental crust ^{232}Th\$^{238}$U mass ratio of 3.8 for the detritus and ^{230}Th, ^{234}U and ^{238}U in secular equilibrium. All activity ratios were calculated using the half-lives from Cheng et al. (2000). Since the growth patterns of speleothems may be complex, an age-distance model needs to be applied to obtain a robust time series. We used the algorithm StalAge (Scholz and Hoffmann 2011) to calculate the depth-age models.

Trace element concentrations were determined using an Element 2 single-collector sector-field ICP-MS coupled with a New Wave Research Nd:YAG UP 213 nm laser system. Samples were ablated at equidistant spacing depending on the mean growth rate of the speleothem (HLK2: 500 µm, NG01: 2 mm, TV1: 1 mm). Jochum et al. (2007; 2012) give a detailed description of the instruments used for LA-ICP-MS. The reference glass NIST 612 was measured every 35 sample spots in order to account for instrumental fractionation and elemental sensitivity. Data reduction was performed with the recently developed software TERMITE (Mischel et al. 2016). Samples for stable carbon and oxygen isotope analysis were obtained at

the same resolution as the trace elements using a micromill system in order to enable direct comparison of the climate proxies. Stable isotope measurements were performed using a ThermoFisher GasBench II linked to a $DELTA^{plus}XL$ mass spectrometer. Values are reported relative to the VPDB standard. Long-term precision of the δ^{13}C and δ^{18}O values, estimated as the 1σ-standard deviation of replicate analyses, is 0.06 and 0.08 ‰(Spötl and Vennemann 2003).

3.2.4 Cave monitoring

Monthly aggregated samples of soil water, one under forest (SW1, Supplemental Figure B.1B) and one under meadow vegetation (SW2, Supplemental Figure B.1B), were obtained at a depth of approximately 60 cm using soil suction probes. Soil air pCO2 values were obtained at the same depth using a Vaisala MI-70 handheld meter and a Vaisala GMP222 Carbon Dioxide probe coupled with a GM70 aspiration pump. The accuracy of the pCO2 measurements is ±150 ppmv + 2 % of the current reading. The values are corrected for air pressure (P) using the equation from (Spötl et al. 2005):

$$CO_{2\ (ppmv)} = CO_{2\ RAW(ppmv)} * \frac{1013}{P} \tag{3.1}$$

Air pressure was measured barometrically with a Sunartis BKT 381/B 381 device. The same instrumental setup was used to measure the pCO_2 inside the cave. The cave monitoring program is set up in a small chamber, close to the location where stalagmite HLK2 grew (Supplemental Figure B.1C). The drip rate was logged using a Stalagmate drip logger (www.driptych.com) at one hour resolution. The logger records up to 5 drops s^{-1}. Additionally, the drip rate was measured manually every time the cave was visited. For this purpose, the number of drips amounting to 2 ml of drip water was counted and the corresponding time recorded. Three fast drip sites (Supplemental Figure 1C (DR)) with an average drip rate of 0.4 drops s^{-1} were instantaneously sampled. In addition, a slow drip site with a water throughput of about 60 ml $month^{-1}$ was also sampled (Mischel et al. 2015). Here we only report the mean value of the three fast drip sites. During the monthly cave trips, water from a cave pool in the Kleine Kammer was also sampled (Supplemental Figure B.1C (PW)). All sampled waters were analysed for pH, electrical conductivity (EC), carbonate hardness, cations and anions as well as δ^{18}O and δD. δ^{18}O and δD values were measured using a ThermoFisher $DELTA^{plus}XL$ mass spectrometer with a Gasbench II and a ThermoFisher DELTA Advantage coupled to a TC/EA at the University of Innsbruck. These instruments were calibrated using VSMOW, GISP and SLAP. The long-term precision (1σ) of the δ^{18}O and δD values is 0.08 ‰and 1.0 ‰, respectively.

Cation concentrations of the drip water samples were determined at Heidelberg University using an Agilent ICP-OES 720. The internal 1 σ-standard deviation is <1% for Ca, Mg, Ba and Sr. SPS SW2 was used as external standard and its long-term 1σ-reproducibility is 1.7%

for Ca, 3.6% for Mg, 3.6% for Sr and 1.7% for Ba. PO_4^{3-} was measured spectrometrically (Specord 50 plus (Analytik Jena, Germany)).

3.3 Results

3.3.1 ^{230}Th\U-dating and age modelling

The results of ^{230}Th\U-dating are presented in Supplemental Tables 1-3 and the age models constructed using StalAge are displayed in Figure 3.1. The ^{238}U concentration of the stalagmites ranges from 0.02 to 0.3 $\mu g\, g^{-1}$. Sub-sample SM39 from stalagmite NG01 is not in stratigraphic order (Figure 3.1, Supplemental Table 1). Since all other ages of the corresponding section are in stratigraphic order and indicate a constant growth rate, sub-sample SM39 is regarded as an outlier and discarded. The relatively large uncertainty at the beginning of the youngest growth phase of NG01 is a result of StalAge, which uses ensembles of three-point-fits and, thus, attaches only little importance to individual ages in the border areas of individual growth phases (Scholz and Hoffmann 2011). This is reflected by considerably enlarged age model uncertainties at the beginning and end of the growth sections, in particular in case of changes in growth rate (Scholz et al. 2012). All other 22 ages determined of NG01 are in stratigraphic order (Figure 3.1). The recent growth of stalagmite NG01 is confirmed by extrapolation of the age model to the top of the stalagmite. The 18 ages obtained for stalagmite HLK2 are all in stratigraphic order within error (Supplemental Table 2, Figure 3.1). The recent growth of this stalagmite, suggested by the wet surface when collected (Supplemental Figure B.2B), is not confirmed by the dating. The youngest age is 2.2 ka, and extrapolation of the age model suggests a top age of the stalagmite of 0.59 ± 0.28 ka. The lowest part of the stalagmite below the clay layer (indicated by the black arrow in Supplemental Figure 3B) is older than 58 ka (Supplemental Table 2) and not subject of this paper. The 12 sub-samples obtained on stalagmite TV1 are in stratigraphic order (Figure 3.1, Supplemental Table 3).

The first growth period after the Last Glacial started at 13.62 ± 0.13 ka BP (HLK2, Figure 3.1). Speleothem growth during the Late Glacial is uncommon for caves in central Germany (Niggemann et al. 2003). This early growth phase is constrained by five ages and lasted for about 550 years until 13 ka BP. The next sample, at a depth of 108 mm distance from top (dft), has an age of 11.99 ± 0.13 ka BP. Thus, HLK2 have a hiatus between 13 and 12 ka BP or at least a phase of very slow growth. However, since this phase corresponds to the Younger Dryas with lower temperatures and probably reduced vegetation, an interruption of speleothem growth is likely. Thus, we assume a hiatus during this phase (Figure 3.1). Stalagmites NG01 and TV1 started to grow at 11.13 ± 0.08 and 10.26 ± 0.08 ka BP, respectively. Stalagmite TV1 grew continuously until the present day. Stalagmite NG01 has two hiatuses, one between 8.81 ± 0.01 and 7.65 ± 0.06 ka BP and another one between 4.96 ± 0.07 and 2.2 ± 0.04 ka BP (Figure 3.1, Supplemental Table 1). Stalagmites HLK2 and TV1 (Supplemental

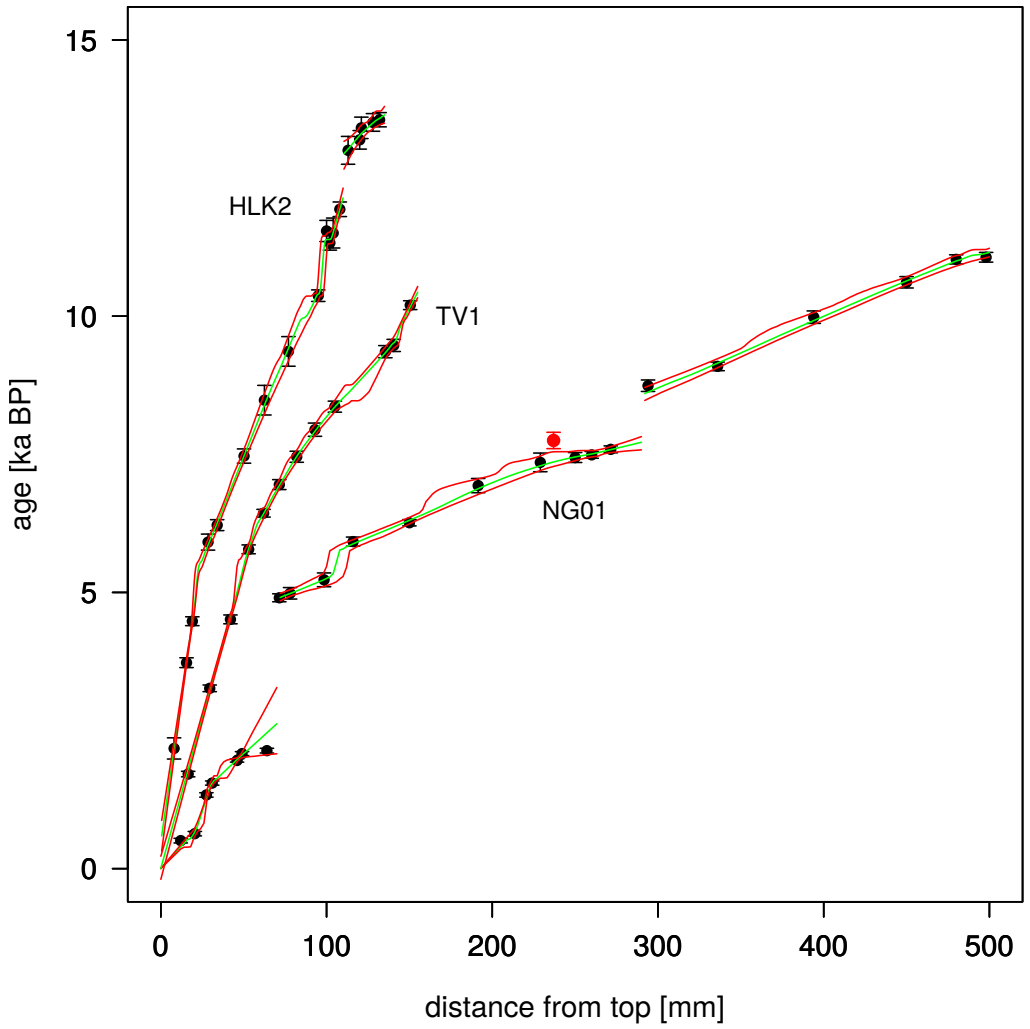

Figure 3.1: Depth-age models of stalagmites HLK2, TV1 and NG01 calculated using StalAge. Sub-sample SM39 not used for age modeling is marked in red.

Figure B.4) have slow growth rates between 5 and 35 µm a^{-1}. In contrast, the two older parts of stalagmite NG01 grew much faster (80 to 140 µm a^{-1}). The youngest growth phase again has a slower growth rate of approximately 40 µm a^{-1} (Supplemental Figure 4).

3.3.2 Stable isotope and trace element data

The $\delta^{13}C$ values of the two host rock samples are between 1.6 and 2.9‰, the $\delta^{18}O$ values range from -4.8 to -5.2 ‰. These results are in agreement with the values published by (Richter et al. 2010), who found $\delta^{13}C$ values between 1.8 and 2.7 ‰and $\delta^{18}O$ values from -1.0 to -5.3 ‰. These values are typical for Devonian limestone from the Rhenish Slate Mountains.

The stable isotope and trace element data of the three stalagmites are compiled in Figures 2 - 4, the values measured on the host rock are found in Supplemental Table 4. We present $\delta^{13}C$ and $\delta^{18}O$ values as well as the concentrations of Mg, Sr, P, Ba and U. The magnitude and variability of these proxies is comparable in all three stalagmites (Table 1). The long-term trend of all data sets was calculated by an interpolating spline with five degrees of freedom (Figures 2-4) using the smooth.spline function of R (R Core Team 2016).

The early growth phase of stalagmite HLK2 is generally characterized by more negative $\delta^{18}O$ values (Figure 3.2, Table 1) and a decreasing trend after the onset of growth during the Bølling/Allerød. During the Younger Dryas, stalagmite HLK2 stopped growing. With the onset of the Holocene, the $\delta^{18}O$ values increase in all three stalagmites. In HLK2 and TV1, the $\delta^{18}O$ values record a distinct depression around 8.2 ka, whereas this phase is characterized by a hiatus in stalagmite NG01 (Figure 3.2). The remaining part of the Holocene is characterized by variable $\delta^{18}O$ values without a strong trend in both HLK2 and TV1. NG01 has a trend in the $\delta^{18}O$ values in the youngest part, with larger values at the beginning and end of the growth phase. The $\delta^{13}C$ values of stalagmites HLK2 and TV1 are comparable and indicate a similar long-term trend. Both stalagmites exhibit relatively low $\delta^{13}C$ values at the beginning of the Holocene followed by a trend towards more positive values starting around 10 ka BP. The most positive values are observed between 8 and 4 ka BP. Subsequently, the $\delta^{13}C$ values decrease towards the present day. The evolution of the $\delta^{13}C$ values of stalagmite NG01 is different, as a mid-Holocene maximum recorded by the other stalagmites is not present (Figure 3.2). Furthermore, stalagmite NG01 has a distinct minimum in $\delta^{13}C$ around 2 ka BP (Figure 3.2) and rapidly increasing $\delta^{13}C$ values towards the present day. Both patterns are not visible in the other records. Nevertheless, the magnitude of the $\delta^{13}C$ values of NG01 is generally comparable with that of the other stalagmites (Table 1). Visible in the Late Glacial part of HLK2 is a strong negative trend in both Mg and Sr with high initial values followed by rapid decrease (Figure 3.3). Whereas the Mg content of TV1 decreases during the Holocene, the Holocene Mg records of HLK2 and NG01 values decrease during the Early Holocene and are relatively stable afterwards (Figure 3.3). Interestingly, the mean Mg content of the Holocene part of stalagmite HLK2 is about twice as high as that of NG01 despite of the general similarity

of the long-term signals (Table 3.1). The Sr content decreases during the Holocene in all three stalagmites and, thus, has a similar long-term pattern (Figure 3.3). In phosphorus, Ba and U the same long-term pattern is visible in the Late Glacial part of stalagmite HLK2 with decreasing concentrations at the beginning and increasing concentrations towards the end. The evolution of these three elements is also comparable in the Holocene sections of the three stalagmites. Phosphorus and Ba in HLK2 have higher concentrations at the beginning of the Holocene, followed by a progressive decrease. Between 10 ka BP and today, TV1 has a similar long-term pattern as HLK2. The U content slightly decreases in the long-term trend in all stalagmites. As for the other proxies, the long-term evolution of the P, Ba and U content of NG01 is slightly different, in particular in the youngest section of the stalagmite. The mean values of the three elements agree well between the three stalagmites (Table 3.1).

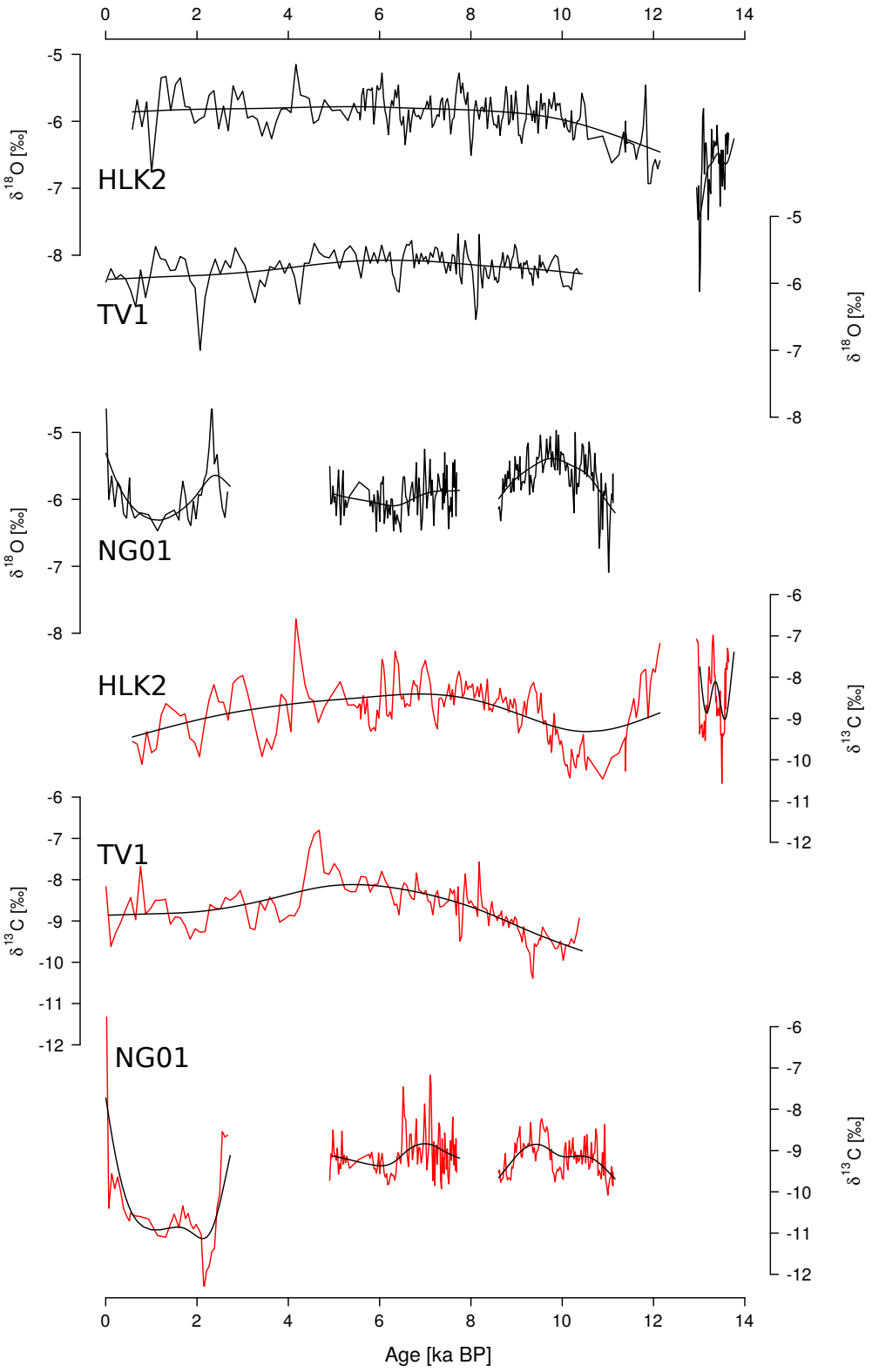

Figure 3.2: Temporal evolution of the δ^{18}O and δ^{13}C values of stalagmites HLK2, TV1 and NG01. The black lines are the long-term trends of the data.

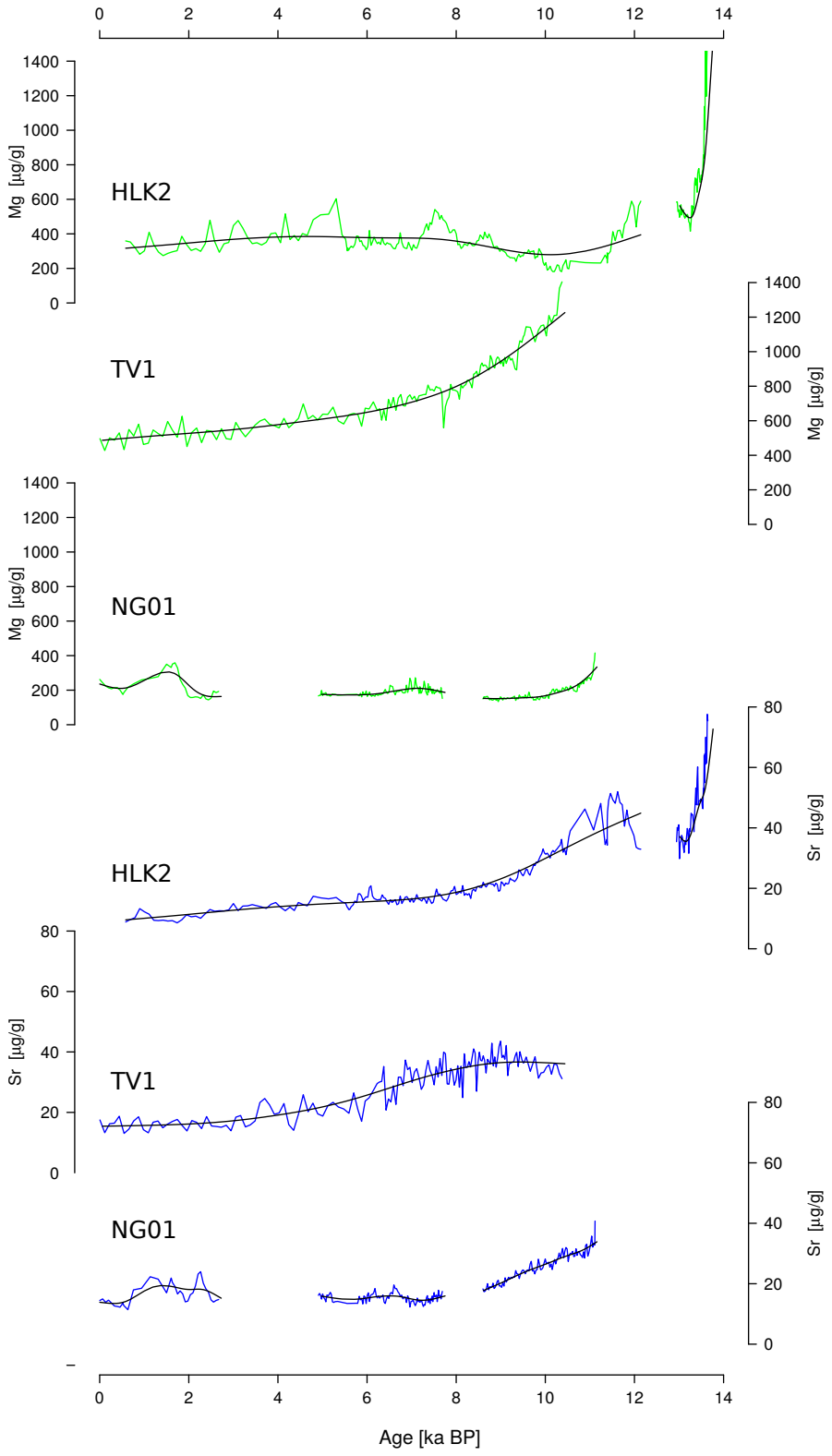

Figure 3.3: Temporal evolution of the Mg and Sr concentrations of HLK2, TV1 and NG01. The black lines are the long-term trends of the data.

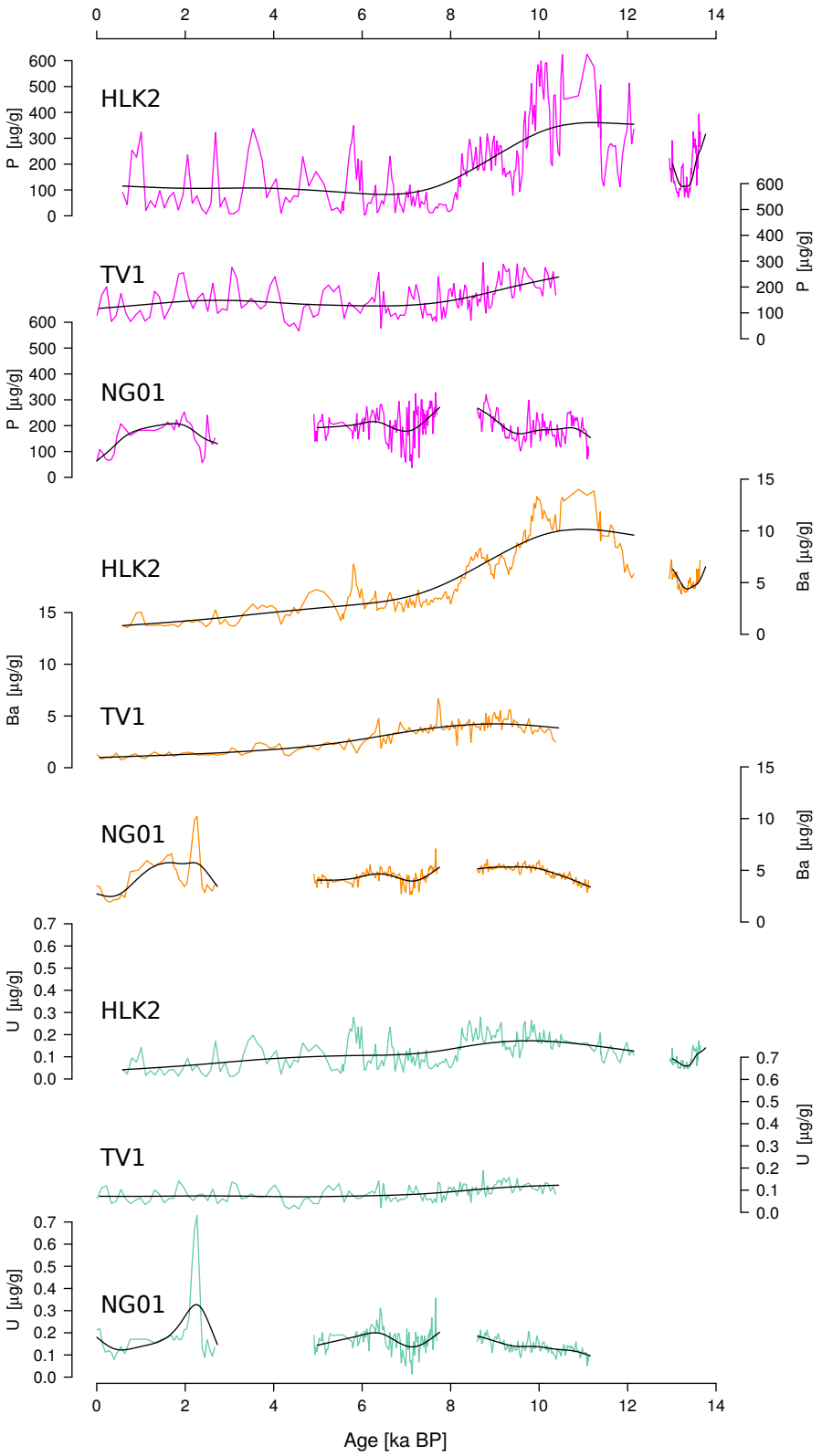

Figure 3.4: Temporal evolution of the P, Ba and U concentrations of HLK2, TV1 and NG01. The black lines are the long-term trends of the data.

Table 3.1: Mean values and standard deviations of the stable isotope and trace element data of the individual stalagmites. HLK2 LG corresponds to the Late Glacial part of stalagmite HLK2.

Stalagmite	δ^{13}C ‰		δ^{18}O ‰		Mg [µg g^{-1}]		Sr [µg g^{-1}]		P [µg g^{-1}]		Ba [µg g^{-1}]		U [µg g^{-1}]	
	mean	SD	mean	SD	mean	SD	mean	SD	mean	SD	mean	SD	mean	SD
HLK2 LG	-8.5	0.8	-6.7	0.5	735	303	47.0	11.4	179	84	5.1	0.8	0.09	0.04
HLK2	-8.8	0.7	-5.9	0.3	340	84	21.8	9.8	186	155	5.5	3.5	0.13	0.07
TV1	-8.7	0.6	-5.8	0.2	760	205	28.4	8.8	155	61	3.1	1.3	0.09	0.03
NG01 youngest section	-10.5	0.8	-5.9	0.4	222	62	16.6	3.3	159	57	4.4	2.1	0.2	0.2
NG01 older section	-9.1	0.5	-5.8	0.4	195	42	20.4	6.3	201	57	4.6	0.7	0.15	0.05

3.4 Discussion

Speleothem proxy signals (both stable isotope and trace element signals) may be influenced by a variety of processes (Fairchild and Treble 2009; Lachniet 2009; McDermott 2004). Thus, their interpretation in terms of past climate variability, in particular during phases of relatively stable climate such as the Holocene, may not be straightforward. A multi-proxy approach to coeval stalagmites from the same cave provides the advantage that common robust features of the records, driven by a general process (e.g., a change in precipitation above the cave), may be extracted. This may enable to disentangle the various processes influencing the proxy signals from each other as well as the climate signals from the intrinsic noise of the specific cave system. In order to identify common features of the different proxy signals, we performed correlation and principal component analysis (PCA) of the data sets of the individual stalagmites. For improved comparability, NG01 was divided into two parts separated by the ca. 2.2 ka-long hiatus at 4.9 ± 0.07 ka BP (Figures 2-4). The older part has substantially higher growth rates than the young part (Supplemental Figure B.4). Similarly, stalagmite HLK2 is separated by the hiatus into the Late Glacial and the Holocene part.

To avoid artificial correlations due to long-term trends, we detrended all records using an interpolating spline with five degrees of freedom (Figures 2-4), which was subtracted from the dataset. The long-term trends can be considered as reflecting orbital to millennial-scale information, whereas the detrended records reflect centennial to decadal-scale variability. Both signals may, in principle, contain paleoclimate information.

In the following, we first discuss the δ^{18}O records of our stalagmites and compare them with other paleoclimate archives. Subsequently, the δ^{13}C and trace element data are discussed in greater detail based on the results of the statistical analyses.

3.4.1 δ^{18}O values

The detrended δ^{18}O values of the speleothem records are not significantly correlated with the other proxies (Supplemental Figure B.5). The exception are the δ^{13}C values, which exhibit weak to moderate positive correlations with the δ^{18}O values in the Holocene growth phases, except the youngest part of NG01. In addition, the δ^{18}O values of the older section of stalagmite NG01 have a weak positive correlation with the Mg concentration. This suggests that the δ^{18}O values are influenced by different processes than the other proxy signals weakening potential correlations. It is well known that speleothem δ^{18}O signals are influenced by a variety of different processes occurring in the atmosphere (affecting the δ^{18}O value of precipitation), in the soil and the karst aquifer as well as inside the cave (Lachniet 2009; Dreybrodt and Scholz 2011). Our recent study of drip water δ^{18}O values based on cave monitoring and meteorological data (Mischel et al. 2015) showed that the δ^{18}O values of the drip water at the HL are influenced by a complex interplay of different processes. Mischel et al. (2015) examined the influence of the North Atlantic Oscillation (NAO) on drip water δ^{18}O values at the HL

and concluded that the reconstruction of the NAO from speleothems at the HL is challenging if not even impossible. The most important factors biasing the present-day speleothem $\delta^{18}O$ signal are the even distribution of precipitation at the HL throughout the year and the slow growth rate of speleothems, precluding the reconstruction of seasonal climate signals. This suggests that the interpretation of speleothem $\delta^{18}O$ signals at the HL during the climatically stable period of the Holocene is difficult as has also been shown for other cave systems (Scholz et al. 2012). This is further supported by the reconstruction of precipitation from Litt et al. (2009), they reconstructed relatively stable rainfall amounts during the last 5 ka for central Europe.

Although the interpretation of the $\delta^{18}O$ values is challenging, comparison with other records may provide information on supra-regional climate patterns. Figure 3.5 shows a comparison of the three speleothem $\delta^{18}O$ records with the $\delta^{18}O$ values of the NGRIP ice core, the lake Ammersee ostracod $\delta^{18}O$ record (von Grafenstein et al. 1999) and a stacked speleothem $\delta^{18}O$ record from nearby Bunker Cave (Fohlmeister et al. 2012). The Allerød is recorded in stalagmite HLK2, and its isotope pattern compares well with that of NGRIP and Ammersee.

At the beginning of the Younger Dryas, the speleothem $\delta^{18}O$ values decrease abruptly. Subsequently, stalagmite growth ceased, which is probably related to the rapid cooling and drying at the beginning of the Younger Dryas (Björck et al. 1996; Litt et al. 2009). After the Younger Dryas, speleothem growth at the HL recommenced. The generally increasing $\delta^{18}O$ values between the Younger Dryas and ca. 10 ka BP as visible in the NGRIP and Bunker Cave record are clearly visible in both the HLK2 and the NG01 $\delta^{18}O$ record (Figure 3.5). This suggests that on the millennial scale, speleothem $\delta^{18}O$ values at the HL reflect large-scale climate variability in the North Atlantic area. In stalagmites HLK2 and TV1, the 8.2 ka event is expressed as a pronounced negative $\delta^{18}O$ excursion (Figure 3.5). The timing of the event is in agreement in both stalagmites and also agrees with the negative excursion recorded in the Ammersee, NGRIP and Bunker Cave records. The 8.2 ka event is not preserved in Stalagmite NG01, there is a hiatus. In stalagmite HLK2, a negative excursion at 9.1 ± 0.2 ka BP might coincide with the 9.1 ka climate anomaly in the Alps as reported by (Boch et al. 2009). This event is also recorded in other paleoclimate archives and other regions, for instance in a stalagmite from Dongge Cave in China (Dykoski et al. 2005) and in the Ammersee record (Figure 3.5). However, the other speleothem $\delta^{18}O$ records (NG01 and TV1) and the Bunker Cave record do not show this event as a pronounced excursion. In addition, all speleothem records from the HL show a pronounced trough between 10.3 and 10.0 ka which is also clearly visible in the Bunker Cave record. This event probably corresponds to the supra-regional cooling event discussed by (Boch et al. 2009). Considering the proximity of Bunker Cave and the HL (Supplemental Figure B.1) the $\delta^{18}O$ records at the two cave sites are expected to be similar. However, except for the prominent cooling phases discussed above, the records do not show striking similarities. For instance, the large positive peak in the Bunker Cave record during the Little Ice Age is not visible in the speleothems from the HL. This may be related

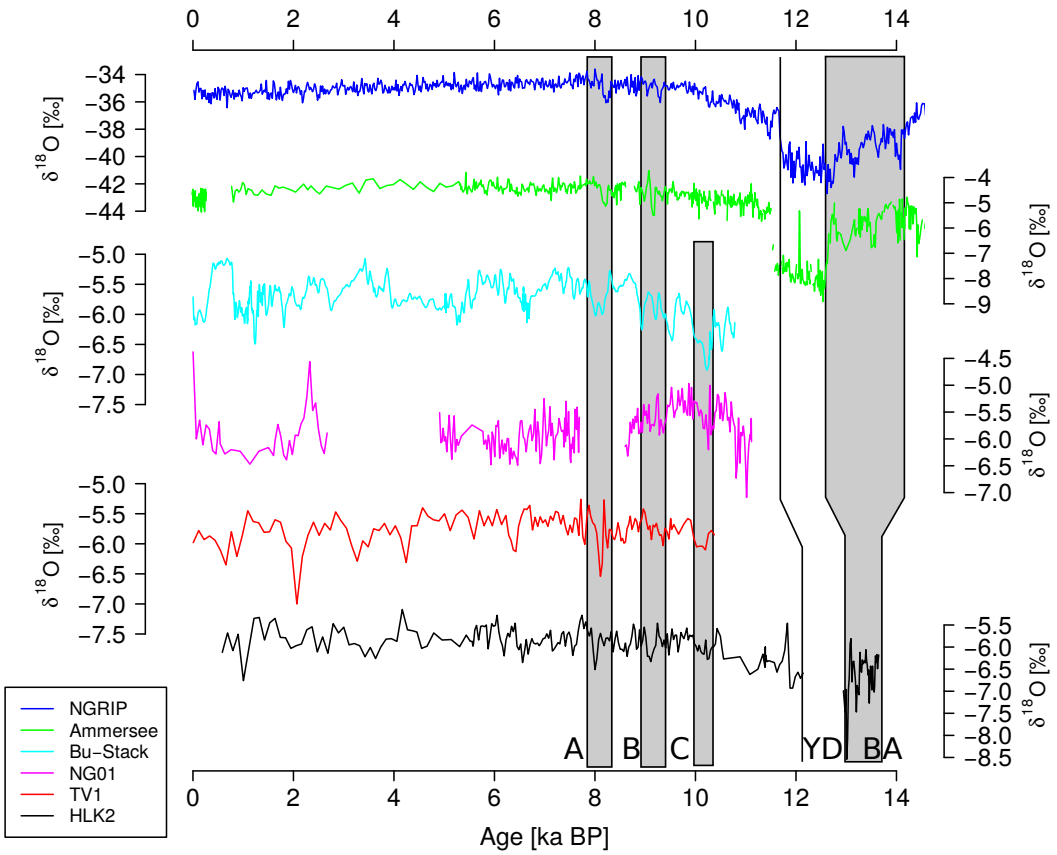

Figure 3.5: Comparison of the $\delta^{18}O$ values of speleothems NG01 (magenta), TV1 (red) and HLK2 (black) with the $\delta^{18}O$ records from NGRIP (blue, Vinther et al. 2006), Ammersee (green, von Grafenstein et al. 1999) and Bunker Cave (cyan, Fohlmeister et al. 2012). Light grey boxes indicate the Bølling/Allerød (BA) as well as the 10.0 (C), 9.1 (B) and 8.2 (A) ka events (Boch et al. 2009). Also indicated is the Younger Dryas (YD) to Holocene transition (solid line). The dark grey boxes indicate phases with similar evolution of the $\delta^{18}O$ values at the HL and Bunker Cave.

to the slow growth of NG01 and TV1 during this period. The differences between the $\delta^{18}O$ signals at the HL and Bunker Cave may either result from the dating uncertainties or effects occurring in the local karst aquifers.

3.4.2 $\delta^{13}C$ values and trace elements

The growth rates of stalagmites HLK2 and TV1 are relatively low and more or less constant over the entire Holocene (∼10 µm a^{-1}, Supplemental Figure B.4). The growth rate of NG01 is much higher (∼80 µm a^{-1}), even in the youngest part (∼40 µm a^{-1}, Supplemental Figure B.4). The most likely explanation for this difference is that the drip rate of the stalactite that fed stalagmite NG01 was much higher and/or that the supersaturation with respect to calcite of

the drip water feeding this stalagmite was higher. Since the gallery was destroyed by quarrying before our study was conducted, this cannot be confirmed by monitoring. Nevertheless, it seems to be a common pattern for all stalagmites that growth rates are higher during the early growth phases and lower and rather constant during the last 4-6 ka (Supplemental Figure B.4). Since both drip rate and supersaturation may have a substantial effect on speleothem stable isotope values (Scholz et al. 2009; Mühlinghaus et al. 2009; Riechelmann et al. 2013) and trace element concentrations (for instance due to their influence on prior calcite precipitation (PCP), Fairchild and Treble 2009), this may have important consequences for the proxy signals recorded in the stalagmites. Thus, differences between NG01 and the other stalagmites need to be considered in the interpretation of the proxy records.

Supplemental Figure B.5 contains the correlation matrices of the detrended dataset of all stalagmites. Phosphorus, Ba and U are positively correlated throughout the Holocene, except for the youngest part of NG01. Phosphorus originates from the host rock (dissolution of apatite), serves as a plant nutrient and is recycled biogeochemically (Fairchild and Treble 2009). A more productive vegetation cover leads to more leaf litter, which will then be leached and flushed into the cave leading to a higher P concentration of the cave drip water (Huang et al. 2001; Borsato et al. 2007). Figure 3.6 shows that the seasonal pattern of phosphate concentration in the drip water indicates flushing of phosphate into the cave during autumn and winter. Figure 3.6 also shows the drip rate, which peaks during winter months at the HL (Mischel et al. 2015). Since the retention time of the drip water is about 10 months (Mischel et al. 2015), transmission of the trace element signals into the cave should lag the peaks in drip rate by ca. 1 year and consequently not affect the seasonal pattern. Thus, the monitoring data confirm our hypothesis. More productive vegetation also leads to increasing soil pCO_2 due to the higher degree of soil microbial activity and root respiration. This is also clearly visible in the monitoring data from the HL, which reveals a pronounced seasonal cycle in soil pCO_2 (Figure 3.6). The related change in the acidity of soil CO_2 may influence the Ba content of the drip water (Hellstrom and McCulloch 2000), which should consequently lead to higher values during spring and summer months. However, the Ba content of the drip water peaks in winter months and is anti-correlated with soil pCO_2 (Figure 3.6). This suggests that Ba, similar to P, is flushed into the cave during autumn and winter when drip rates are higher. As U is positively correlated to P and Ba, the U content also seems to be related to vegetation. The U content of the drip water can also be influenced by the change from more oxidizing to more reducing conditions in the soil regime with U being more mobile in oxidized environments (Hellstrom and McCulloch 2000). We interpret P, U and Ba as proxies for vegetation productivity above the cave, with increasing concentrations of all elements reflecting a stronger intensity of nutrient cycling. This is a function of the availability of leaf litter, root respiration and biological activity, which correlate with a more productive vegetation. Figure 3.4 displays the long-term trend of P, Ba and U in the three stalagmites. These elements have a similar trend, in particular in stalagmites HLK2 and TV1, with higher

values during the Early Holocene, which progressively decrease towards the recent past. This may reflect a gradual depletion of the source of these elements, for instance, a loess cover, as has been suggested for other sites (Fohlmeister et al. 2012). Stalagmite NG01 has a different long-term pattern, probably due to the different growth rate. The Mg content of speleothems has been interpreted as a proxy of effective precipitation (McMillan et al. 2005; Fairchild and Treble 2009). A longer residence time in the karst aquifer, due to a reduction in precipitation and recharge, leads to a prolonged contact of the water with the host rock. Even if the water is saturated with respect to calcite, it may still leach Mg from the host rock due to the lower solubility of dolomite. This, in turn, leads to elevated Mg concentrations in the drip water (Roberts et al. 1998; Fairchild and Treble 2009). Higher Mg concentrations in the drip water thus reflect less recharge and vice versa. In most of our stalagmite records, Mg is negatively correlated with P, Ba and U and positive correlated with δ^{13}C (Supplemental Figure B.5). This indicates less Mg and consequently increased recharge during times of more productive vegetation, probably reflecting wetter conditions. We note that more productive vegetation may also lead to increased transpiration and, thus, a reduction in recharge (Mischel et al. 2015). If evapotranspiration exceeds summer rainfall, this leads to a deficit in soil moisture, which might be reflected by decreasing drip rates in the cave (Mischel et al. 2015). If the amount of rainfall remains constant, more productive vegetation would result in a higher Mg content of the drip water due to a longer residence time of the groundwater. Since we observe the opposite in the speleothems from the HL, this effect either seems to be negligible or is compensated by additional summer rainfall. Mischel et al. (2015) explained that summer rainfall currently contributes 40 % to the annual precipitation.

Interestingly, Sr has a significant positive correlation with Ba in all records, but no correlation with P and U (Supplemental Figure B.5). In the Late Glacial part of HLK2, Sr is positively correlated with Ba and negatively correlated with P and U (Supplemental Figure B.5). This suggests that the variability of these trace elements was influenced by different processes during this period. The positive correlation with Sr suggests that Ba may also be influenced by PCP. This process should generally result in elevated Mg, Sr and Ba concentrations (Stoll et al. 2012) as well as increasing δ^{13}C values (Johnson et al. 2006). The positive correlation between Sr, Ba and Mg in the drip water (Figure 3.6) thus supports PCP and/or a higher degree of CO2 degassing during times of low drip rates (Johnson et al. 2006). Drip water δ^{13}C values have a different trend than drip water Mg, Sr and Ba content (Figure 3.6) indicating a different process dominating the δ^{13}C signal (discussed in detail below). In the stalagmite records, Sr and Ba are positively correlated, whereas Mg is negatively correlated with Ba and negatively or even not correlated with Sr (Supplemental Figure B.5). This suggests that PCP did either not occur during the Holocene or was masked by another process, which has a more pronounced effect on the trace element signals.

If PCP is dominant, a positive correlation between Mg and Sr would be expected due to suppressed incorporation of Mg and Sr into calcite in comparison to Ca. This effect is

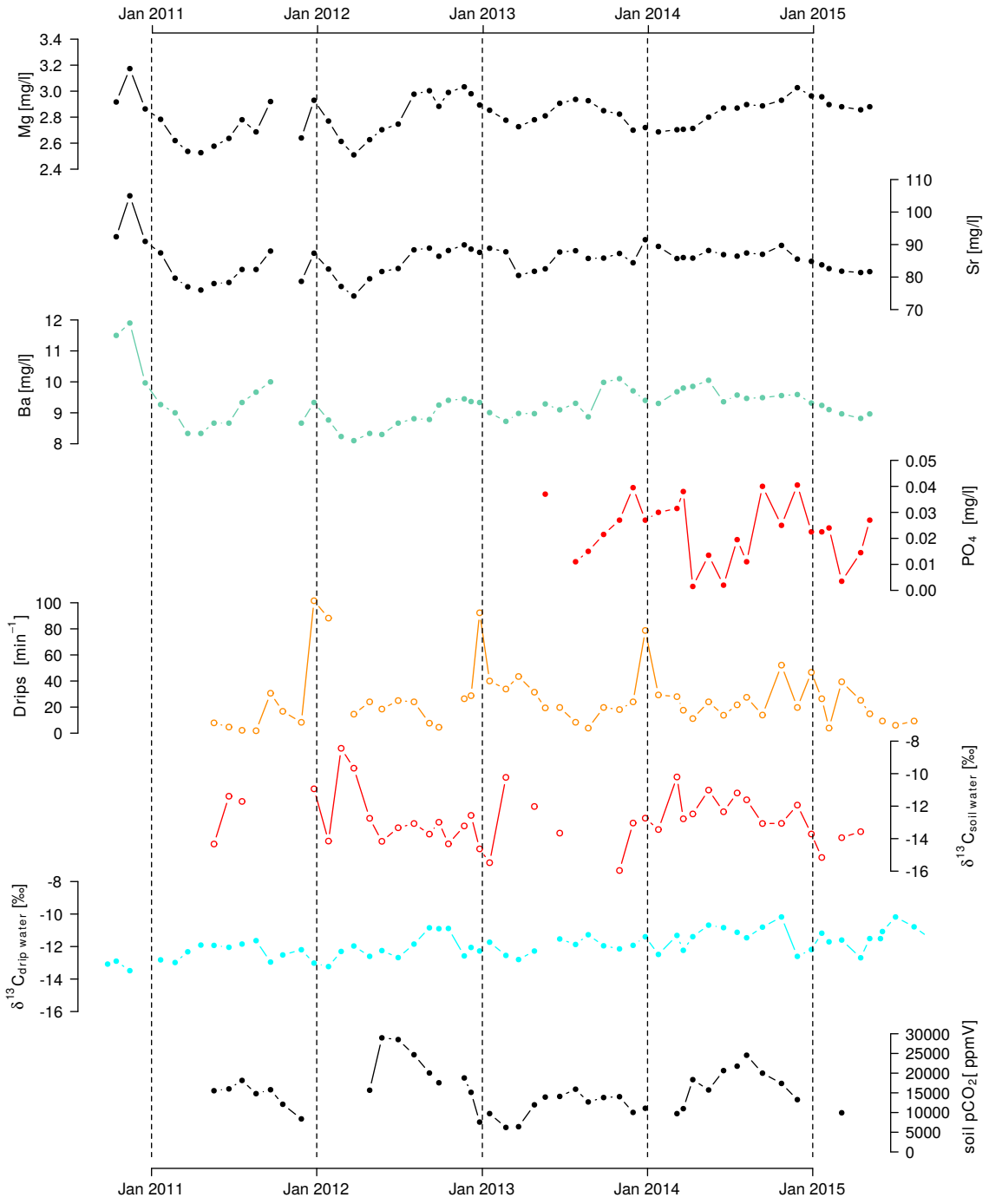

Figure 3.6: Multiannual changes in Mg, Sr, and Ba and PO_4 concentrations of the drip water at the Herbstlabyrinth cave system. Also shown are drip rate, $\delta^{13}C$ values of the DIC of the soil and drip water as well as soil gas pCO_2.

enhanced during times of reduced rainfall since more air-filled voids in the aquifer increase the potential for PCP (Huang et al. 2001; Fairchild and Treble 2009). Another process resulting in a positive correlation between Mg and Sr is selective leaching of minerals in the soil (e.g., loess; Huang et al. 2001). A positive correlation between Mg and Sr is only observed in the Late Glacial part of stalagmite HLK2 (Supplemental Figure B.5), suggesting that neither of these processes (PCP and selective leaching) were dominant during the Holocene. We observe a slight decrease in the Mg/Ca and Sr/Ca ratio of the drip water during the winter for the fast drip site (Supplemental Figure B.6). However, the total variability of the Mg/Ca and Sr/Ca ratios is relatively low. For the slow drip site, the Mg/Ca and Sr/Ca ratios decrease during winter months (Supplemental Figure B.6). This indicates the influence of PCP at the slow drip site during summer. This contrasts winter, when the aquifer is filled with water the effect of PCP is diminishing. However, since Sr and Mg are not correlated in the Holocene stalagmite records, PCP was either of minor important or masked by other processes.

All stalagmite records show a long-term decrease in Sr content during the Holocene (Figure 3.3). A potential explanation for this trend is that both Mg and Sr originate from a thin loess cover that was deposited during the Last Glacial, which has then been progressively leached during the Holocene. Fohlmeister et al. (2012) observed a similar long-term trend in Mg content during the Holocene in a speleothem record from nearby Bunker Cave and proposed a similar mechanism.

Speleothem δ^{13}C values are negatively correlated with P, Ba and U, which is visible in the Holocene records of HLK2 and TV1 as well as the older part of NG01 (Supplemental Figure 5). The δ^{13}C values of the host rock are between 1.6 and 2.9 ‰, and the vegetation above the cave consists mainly of C3-plants. The corresponding δ^{13}C values of the soil air should therefore be between -26 and -20 ‰. The δ^{13}C values of the stalagmites range from -10.4 to -6.6 ‰. These values, thus, reflect a partially open system, where the δ^{13}C values are influenced by both the soil CO_2 respired by the C3-plants and the host rock (McDermott 2004). Modelling studies suggest a relationship between the δ^{13}C value of the drip water and soil pCO_2, with more negative δ^{13}C values corresponding to higher soil pCO_2 (Fohlmeister et al. 2011). This relationship is also clearly reflected in the seasonal cycle of the δ^{13}C values of the soil water and soil pCO2 at HL (Figure 3.6). The most negative δ^{13}C values of the soil water are measured shortly after the highest values in soil pCO2. In contrast, no clear relationship between soil pCO2 and the δ^{13}C values of the cave drip water is observed (Figure 3.6). This is probably related to mixing and retention of the recharge water inside the aquifer. Since the monitored drip sites exhibit continuous dripping throughout the year, they are probably fed by a large reservoir in the epikarst. This is also confirmed by the study of Mischel et al. (2015), who estimated a mixing time in the epikarst of about 12 months and a transmission time (i.e., the time the water needs to travel through the host rock) of about 10 months. The effect of mixing leads to a smoothing of the seasonal proxy signals in the drip water. The long-term trend shows increasing δ^{13}C values from the early to the mid-Holocene,

and decreasing values until the present day (Figure 3.2). Processes occurring on shorter time scales, such as changes in cave ventilation and/or disequilibrium stable isotope fractionation (Scholz et al. 2009; Deininger et al. 2012), are unlikely to affect the δ^{13}C signals on millennial time scales. A mature soil containing large amounts of soil organic matter is characterised by higher soil pCO2 values and consequently low soil δ^{13}C values (Fohlmeister et al. 2011). A potential explanation for the observed millennial-scale changes in the δ^{13}C values during the Holocene, thus, is a progressive change in soil thickness and composition above the cave. An alternative explanation is a change in the type of vegetation above the cave. However, since the observed changes in δ^{13}C values are small (in the range of 2-3 ‰, Figure 3.2), major changes in the type of vegetation (e.g., from C3 to C4-plants) are unlikely.

3.4.3 Principal Component Analysis

In order to gain further insight into the behavior of the speleothem proxy data and the corresponding processes, we performed principal component analysis (PCA) using the trace element and stable isotope records of the three stalagmites. PCA was performed using R and the package psych (Revelle 2015). Prior to PCA, the data were detrended using an interpolating spline with five degrees of freedom (Figures 2-4) and normalized using standard methods. PCA analyses multivariate datasets and calculates the contribution of the individual signals to the total variance of the dataset. The number of variables is reduced to a lower number of new variables (i.e., the principal components, PCs) preserving as much of the variation of the original variables as possible. The PCs can be used to identify common structures in the data and are often more easily interpreted than the initial multivariate dataset (Jolliffe 2002). A scree-plot of the eigenvalues versus the PCs allows visual determination of how many meaningful PCs are required to explain the data (by detection of the kink, Supplemental Figure B.7, Jolliffe 2002). In all PCAs, the kink occurs at PC 2 (Supplemental Figure B.7) suggesting that at least two PCs are required to explain the data set. Whereas PC 1 explains ca. 50 % of the variance, PC 2 only explains ca. 20 % (Figure 3.7, Supplemental Table B.5). Thus, PC 2 is only briefly discussed in the following.

For the Late Glacial part of stalagmite HLK2, PC 1 explains 53 % of the variance. P and U have strong, negative loadings on PC 1, while Mg, Sr, Ba and δ^{13}C have a positive loading (Figure 3.7, Supplemental Table B.5). PC 2 explains 20% of the variance, and Sr and Ba have positive loadings, whereas δ^{13}C and Mg have a negative loading. The strong covariation of Mg, Sr, Ba and δ^{13}C in PC 1 indicates that PCP may have played a dominant role during the Late Glacial (Figure 3.7, Supplemental Table B.5). However, since other trace elements also contribute to PC 1, this explanation is not straightforward. The negative loadings of P and U indicate that PC 1 – at least to some extent – also reflects vegetation processes. PC 1 and PC 2 explain 72% of the total variance of the Late Glacial part of stalagmite HLK2 (Supplemental Table B.5).

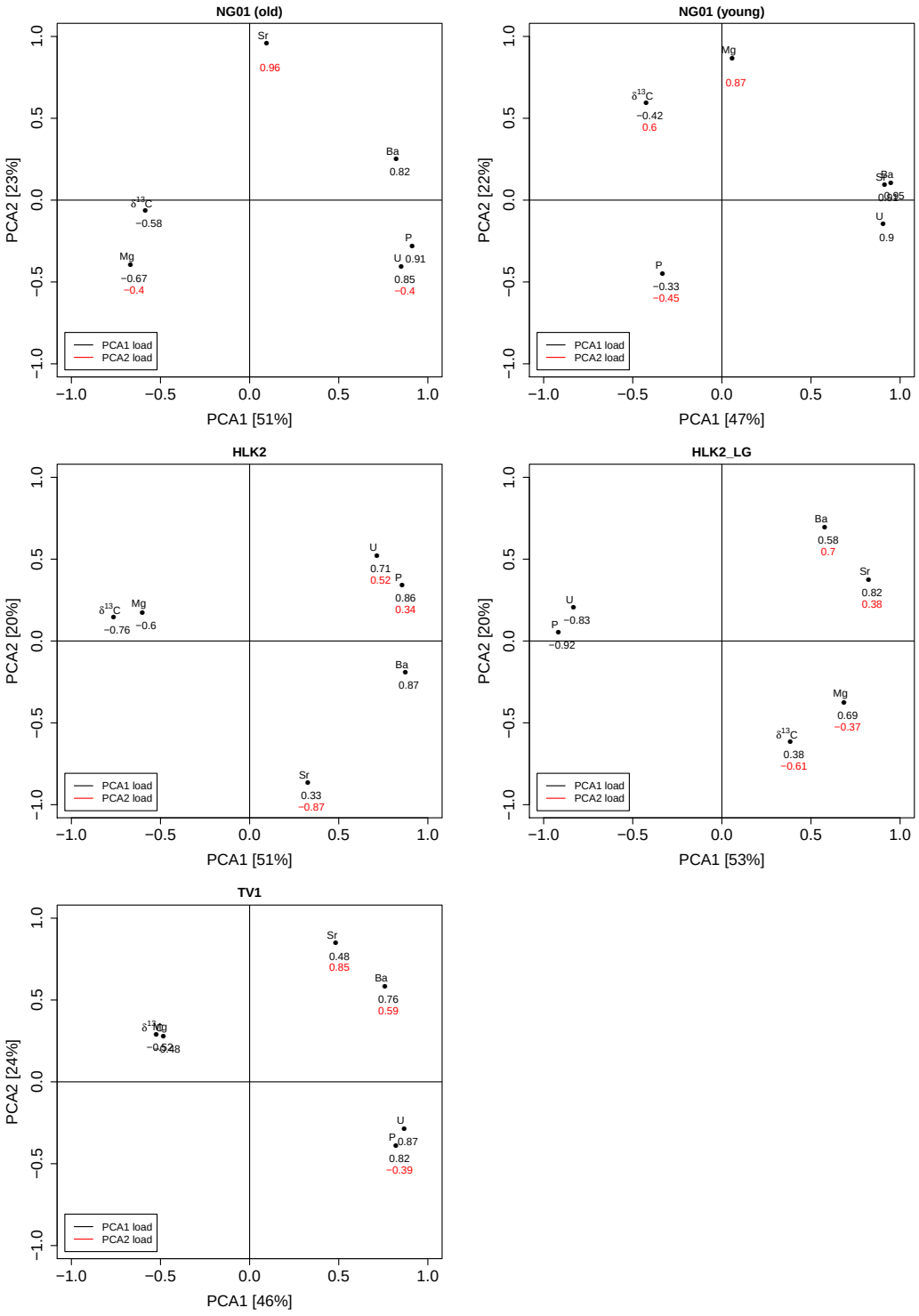

Figure 3.7: Results of PCA of the individual growth phases of stalagmites HLK2, TV1 and NG01. Black and red numbers express the loading on PC 1 and PC 2, respectively.

PC 1 of the Holocene section of stalagmite HLK2 explains 51% of the variance and is composed of P, U, Ba, Sr, δ^{13}C and Mg, with strong positive loadings of P, Ba and U, a strong negative loading of δ^{13}C, a medium positive loading of Sr and a medium negative loading of Mg (Figure 3.7, Supplemental Table B.5). As discussed above, the most likely process to explain this pattern is that P, Ba, U and δ^{13}C reflect changes in vegetation density. The PCA of TV1 has a similar pattern. PC 1 explains 46% of the variance and is also composed of P, Ba, U, Sr, and δ^{13}C and Mg (Figure 3.7, Supplemental Table B.5). As in stalagmite HLK2, Sr has a positive loading on PC 1, whereas Mg has a negative loading (Figure 3.7, Supplemental Table B.5). The positive relationship between Mg and δ^{13}C and the inverse relationship between Mg and P, Ba and U, indicate more humid conditions during times of more dense vegetation and enhanced nutrient recycling. This also confirms that PCP, which should result in a positive relationship between Mg and Sr, did not play a dominant role for the HL speleothems during the Holocene. Stalagmite NG01 is composed of two major growth phases with different growth rates (Figure 3.1 and Supplemental Figure B.4). Growth rate can have a substantial effect on proxy signals. For instance, the incorporation of trace elements into calcite can be different at higher growth rates (McMillan et al. 2005; Fairchild and Treble 2009). Furthermore, at higher recharge (and consequently higher speleothem growth rates), more particles and colloids are commonly flushed into the cave and incorporated into the speleothem (Fairchild and Treble 2009). Therefore, the two growth phases are analyzed separately. PC 1 of the oldest growth phase of NG01 explains 51% of the variance and is composed of P, Ba and U, which have a strong positive loading, and Mg and δ^{13}C, which have strong negative loadings (Figure 3.7, Supplemental Table B.5). As discussed above, this probably reflects changes in the productivity of vegetation, in agreement with the other stalagmites. The negative relationship with Mg again suggests that periods of a more productive vegetation coincided with more humid conditions.

The youngest growth phase of NG01 shows the most contrasting PCs (Figure 3.7, Supplemental Table B.5). PC 1 is composed of Ba, U and Sr, having strong positive loadings, and P and δ^{13}C have weak negative loadings. The positive relationship of U, Sr and Ba may again indicate a relationship with vegetation productivity, but the negative relationship with P is different from all other growth phases (Supplemental Figures B.4, B.5, and B.7). PC 2 is composed of δ^{13}C and Mg, having positive loadings, which may reflect PCP and drip rate-dependent isotope fractionation effects controlled by the recharge of the karst aquifer. The negative loading of P on PC 2 (Figure 3.7, Supplemental Table B.5) is also different from the behavior of this element during all other growth phases. In general, the patterns of this part of the stalagmite seem to be more complex than those of the other growth phases.

PC 2 generally explains a lower percentage of the complete variance of the proxy records (20-24%, Figure 3.7, Supplemental Table B.5). Therefore, the processes reflected by PC 2 are less clear and the results are only briefly summarized here. PC 2 of the Holocene section of stalagmite HLK2 explains 20% of the variance and is composed of Sr, P and U (Figure 3.7,

Supplemental Table B.5). Whereas Sr has a strong negative loading, U and P have intermediate negative loadings. PC 2 of stalagmite TV1 explains 24% of the variance and is composed of Sr, Ba and P (Figure 3.7, Supplemental Table B.5). PC 2 of the oldest growth phase of NG01 explains 23% of the variance and is mainly composed of Sr, which has a strong positive loading. Mg and U have negative loadings.

In summary, PCA shows a common pattern for all stalagmites, whereby PC 1 explains about 50% of the total variance in Holocene growth phases. PC 1 is composed of P, Ba and U, which have positive loadings, and δ^{13}C and Mg, which have negative loadings. Therefore, PC 1 is interpreted as a proxy for the productivity of vegetation and precipitation, with higher values of Ba, U, and P and lower values of Mg and δ^{13}C reflecting a more productive vegetation and higher rainfall. A potential explanation for this pattern is that wetter climate fosters more productive vegetation. Conversely, during drier phases with decreasing vegetation (indicated by low P, U and Ba as well as high Mg and δ^{13}C values), the soil and aquifer above the cave contain less water allowing increased ventilation. As a consequence, the karst dissolution regime may change towards a more open system. This has been demonstrated for speleothem records on annual, decadal and even centennial time scales (Fohlmeister et al. 2011; Griffiths et al. 2012; Noronha et al. 2014). A more open system results in lower δ^{13}C values of the drip water and speleothem calcite (Fohlmeister et al. 2011). The δ^{13}C records from the HL show the opposite behavior with higher δ^{13}C values during phases with elevated Mg and lower P, Ba and U concentrations. A potential explanation could be lower soil gas δ^{13}C values due to water stress on plants (Cerling 1984). Another explanation is a change in carbonate chemistry. Lower soil pCO_2 due to reduced vegetation density results in higher pH values of the drip water saturated with respect to calcite and higher δ^{13}C values of the drip water and thus, in the speleothem (Fohlmeister et al. 2011). As periods of lower vegetation density coincide with drier conditions at the HL, the elevated δ^{13}C values could also result from isotope fractionation under disequilibrium conditions or enhanced PCP (Johnson et al. 2006; Deininger et al. 2012). The latter would also be consistent with the positive correlation between δ^{13}C and Mg.

3.4.4 Comparison of the different stalagmite records

In the previous section, we studied each stalagmite separately, which revealed consistent patterns in all samples, such as the positive relationship between U, P and Ba, which is interpreted as reflecting past changes in vegetation productivity. These elements are often negatively correlated with δ^{13}C, further corroborating this relationship. However, the PCA also revealed differences in the behavior of the individual proxies between different stalagmites and even different growth phases of the same stalagmite. These differences may be related to differences in the hydrological pathways feeding the individual drip sites, which is also evident from the very different growth rate of stalagmite NG01. Replicated proxy records are, thus, very useful to separate site-specific from climate-driven processes.

In order to identify common features of the individual records and to eliminate site-specific effects, we compare the principal components rather than individual proxy signals. Figure 3.8 shows a comparison of the first PC of all three speleothems. Since the sign of the columns of the rotation matrix obtained by the PCA is arbitrary, the meaning (explanation) of the PC has to be established separately for each element (see description of the R package prcomp, R Core Team 2016). Comparison of PC 1 with the individual trace element and stable isotope records allows deriving an interpretation of PC 1 (Supplemental Figure B.8). PC 1 of HLK2 has positive peaks when the proxies for vegetation productivity (P, Ba, U) have low values, and the δ^{13}C values and the Mg concentration are elevated (Supplemental Figure B.8). This suggests that higher values of PC 1 correspond to a lower productivity of vegetation. In contrast, PC 1 of TV1 has higher values for elevated P, Ba and U values and lower δ^{13}C values (Supplemental Figure B.8). Thus, higher values of PC 1 of this stalagmite correspond to more productive vegetation. PC 1 of the older part of NG01 has the same pattern as TV1 (Supplemental Figure B.8).

3.5 Comparison with supra-regional climate variability

Figure 3.8 shows a comparison of PC 1 of the three stalagmite records with the record of hematite-stained grains (HSG) from North Atlantic deep-water sediments (Bond et al. 2001). Periods of high HSG values correspond to higher amounts of drift ice and, thus, reflect cool phases in the North Atlantic (Bond et al. 2001). Based on this relationship, Bond et al. (1997; 2001) distinguished nine cooling events (the "Bond events", labeled 0-8 in Figure 3.8) occurring approximately every 1.5 ka, which were shown to be closely related to central European winter temperatures (Mangini et al. 2007). Interestingly, most HSG maxima have corresponding peaks in PC 1 of the three HL stalagmite records (Figure 3.8). This becomes even clearer if the dating uncertainties of all records are taken into account. High percentages of HSG correspond to low values in PC 1 of stalagmite TV1 and NG01 and high values in PC 1 of stalagmite HLK2 (inversely plotted in Figure 3.8) suggesting a less productive vegetation and drier climate at the cave site during Bond events.

Bond events 8 to 6 are clearly visible in the stalagmite records from HL (Figure 3.8). Bond et al. (2001) marked two peaks of high percentages of HSG as Bond event 5. Since the duration of this event is ca. 1000 years long (Figure 3.8), we propose to divide this event up into two separate events on the basis of our stalagmites (labeled 5a and 5b, Figure 3.8). Both events have corresponding peaks in PC 1 of stalagmite TV1. PC 1 of stalagmite HLK2 has a small negative peak during event 5b, and a clear negative peak during event 5a. Stalagmite NG01 has a hiatus in this phase. Both stalagmites (HLK2 and TV1) suggest a relatively low vegetation productivity interrupted by short-term events. Interestingly, the 8.2 ka event occurs during this phase, but both stalagmite records do not suggest a major drop in the productivity of the vegetation. Between Bond events 5 and 4, the HSG record also has a

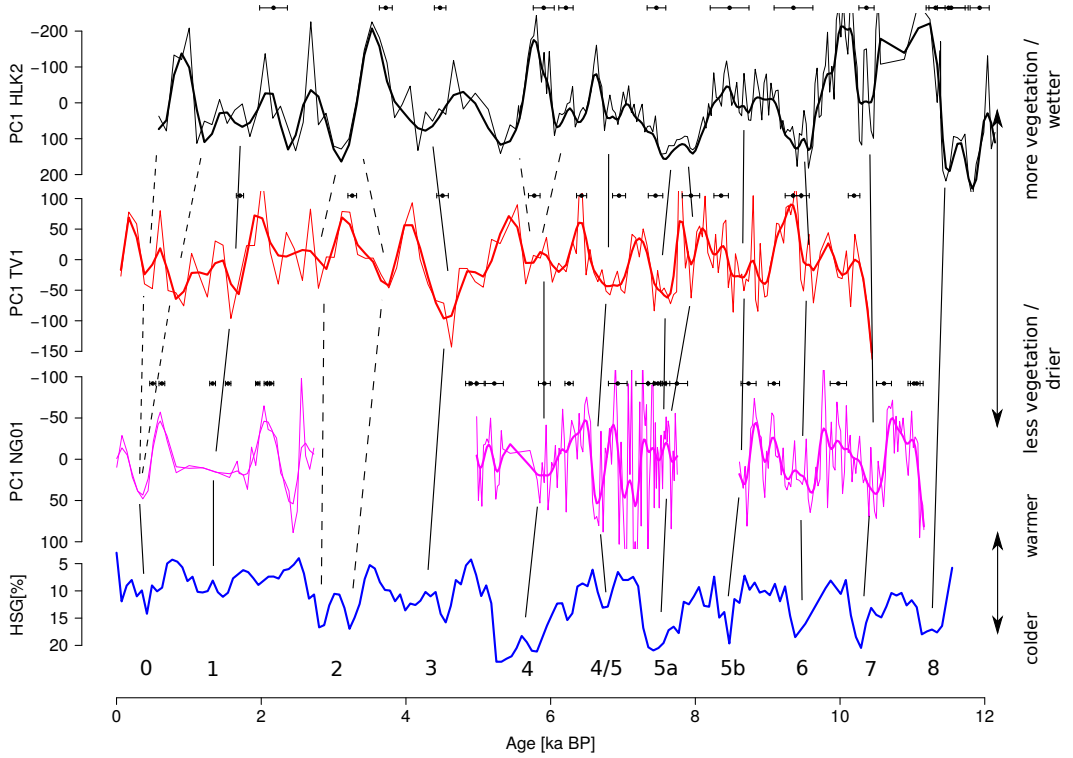

Figure 3.8: Comparison of the PC 1 of stalagmites HLK2 (black), TV1 (red) and NG01 (magenta) with the HSG record (blue, Bond et al. 1997; 2001). Since the interpretation of PC 1 of stalagmite HLK2 is opposite than that of TV1 and NG01 (see main text), the y-axis is inverted for this record. The y-axis of the HSG record is also inverted. ^{230}Th\U-ages with corresponding errors are plotted on top of the individual stalagmite records. Individual Bond events are labelled. The event 4/5 is suggested to be an additional Bond event. Vertical lines indicate phases of lower vegetation productivity potentially corresponding to Bond events. Dashed lines indicate events, which cannot be clearly assigned to a specific Bond event, but may possibly be related to Bond events considering the relatively large dating uncertainties.

small peak (labeled 4/5 in Figure 3.8), which has not been labeled as a Bond event. This event has a clear expression in our speleothem records. On this basis, we assign this phase as an additional short-term Bond event. Bond events 4 and 3 are clearly visible in all speleothem records (Figure 3.8). Event 4 seems to be interrupted by a productive vegetation phase in speleothem HLK2. Bond event 2 seems to have lasted longer than recorded by the HSG record. The relatively short Bond event 1 is visible in PC 1 of all speleothems. However, the age models of the stalagmites are associated with relatively large uncertainty in the youngest section (Figure 3.1). Bond event 0 is reflected in all speleothems (Figure 3.8). As for event 1, the correspondence in stalagmite HLK2 is uncertain, which may be related to the large uncertainties of the age model (Figure 3.1). In summary, each Bond event has a corresponding peak in PC 1 of at least one HL stalagmite. Some events are reflected in all records. Since PC 1 is interpreted as reflecting the productivity of vegetation and precipitation, this suggests an influence of North Atlantic climate variability on vegetation density in central Germany. In case of cooler climate, the vegetation is less productive and vice versa. However, based on the variability of PC 1 (Figure 3.8), the HL stalagmites record more phases of reduced vegetation density than suggested by the Bond et al. (2001) record. For instance, all stalagmite records suggest a phase of less productive vegetation between 7.0 and 6.2 ka BP (event 4/5 in Figure 3.8), which has only a relatively small counterpart in the HSG record. During Bond events 2 and 5, at least two peaks in PC 1 are visible in all stalagmite records (Figure 3.8). This suggests that these events may be divided up into two parts. In total, we identified eleven phases of less productive vegetation in our stalagmite records (Figure 3.8), which in most cases have equivalents in the Bond events.

3.6 Conclusions

Multi-proxy records from three speleothems from the HL cave system reflect several phases of less productive vegetation during the Holocene, which are manifested in lower P, Ba and U concentrations and more positive $\delta^{13}C$ values. The negative correlation of Mg with P, Ba and U and the positive correlation with $\delta^{13}C$ also indicates less recharge during phases of less productive vegetation, probably due to drier conditions. These patterns are clearly reflected in both the correlation analysis and the PCA.

The majority of the observed phases of reduced vegetation productivity and drier climate coincide with cooler periods in the polar North Atlantic as reflected by a higher abundance of HSG (Bond et al. 1997; 2001). This suggests a close relationship between terrestrial climate in central Europe and the polar North Atlantic, even if the timing and duration are slightly different for some of the events. We also identified additional phases of less productive vegetation, which do not have a counterpart in the HSG record, indicating a different (maybe regional) trigger for these phases.

During the Younger Dryas, no stalagmite growth is observed at the HL, which is prob-

ably related to the lower temperatures and reduced precipitation during this interval. The speleothem $\delta^{18}O$ records are in general agreement with the NGRIP $\delta^{18}O$ record on the millennial time scale, which is, for instance, reflected by increasing $\delta^{18}O$ values between the Younger Dryas and ca. 10 ka BP. This suggests that speleothem $\delta^{18}O$ values at the HL reflect large-scale climate variability of the North Atlantic region. This is also confirmed by the 8.2 ka event, which is clearly visible as a pronounced negative excursion in the speleothem $\delta^{18}O$ values. However, in all other proxies, the 8.2 ka event is not well reflected.

In summary, this multi-proxy speleothem study suggests a close relationship between climatic conditions in the polar North Atlantic and central Europe during the Holocene and highlights the potential of speleothem trace element records for high-resolution paleoclimate reconstruction.

Acknowledgements

Thorough and stimulating reviews by Jens Fohlmeister and Tim Atkinson were very helpful to improve the manuscript. SM and DS are thankful to the German Research Council for funding this project (DFG-SCHO1274/3-1, DFG-SCHO1274/9-1). We also thank Augusto Mangini and René Eichstädter from the University of Heidelberg for providing preliminary TIMS ages for HLK2. The assistance of Beate Schwager, Brigitte Stoll and Ulrike Weis during sample preparation and LA-ICPMS is highly appreciated. We furthermore thank Sylvia Bonzio for performing the phosphate measurements. Finally, we are thankful to the local caving club Speleologische Arbeitsgemeinschaft Hessen eV. (SAH eV.) for support and P. Winck and numerous other people for surveying the HL cave system.

4 TERMITE - An R script for fast reduction of LA-ICPMS data and its application to trace element measurements

Simon A. Mischel · Regina Martz-Kraus · Klaus Peter Jochum · Denis Scholz

Abstract

Here we present a script (TERMITE) for reduction of laser ablation inductively coupled plasma spectrometry (LA-ICPMS) data written in the statistical language R. TERMITE is currently capable of reducing both spot and line scan measurements performed with two different mass spectrometers (ThermoFischer Element2 and Agilent 7500ce). Several important parameters can easily be adjusted by the user, who does not need prior knowledge in R. Currently, ten reference materials for calibration of the LA-ICPMS data are implemented, and the user can add additional reference materials if required. TERMITE provides an optional outlier test and calculates elemental concentrations for, ca. 100 sample measurements in less than a minute. The results are provided graphically (as a pdf-file) as well as numerically (as a csv-file). The script itself and step by step instructions for the application of TERMITE including an example data set are provided in the supplemental material. We tested the performance of TERMITE using a speleothem sample from the Herbstlabyrinth cave system, Central Germany, and compare the results with the commercial software GLITTER. Both programs give comparable results in the final concentration. Nevertheless, TERMITE uses the median for the calculation of the background signal and is therefore less prone to artificial spikes in the background signal. One advantage of TERMITE is the ability to use multiple reference materials at once for the correction of the laser ablation data to improve the accuracy of the results.

Keywords: R · LA-ICPMS · trace elements · data reduction · software

4.1 Introduction

Trace element concentrations and ratios determined at high spatial resolution using laser ablation inductively coupled plasma spectrometry (LA-ICPMS) are of great interest for a variety of geological and environmental studies. For example, trace element (e.g. Mg, Sr, Ba, U) to calcium ratios in inorganic as well as biogenic carbonates have been shown to provide valuable information on past climate variability (e.g. Felis et al. 2004; Mertz-Kraus et al. 2009; Yang et al. 2014; Jochum et al. 2012; Fairchild and Treble 2009) and have been established as important climate proxies in various climate archives. In speleothems, trace element concentrations can be used to distinguish between calcite and aragonite because the incorporation mechanisms of these elements into the corresponding minerals are very different (Wassenburg et al. 2012). Other applications include ore deposit research (e.g., Hettmann et al. 2014), mantle petrology (e.g., Foley et al. 2013), and gemological studies (e.g., Zwaan et al. 2015). Trace element data determined by LA-ICPMS have also been used in forensic studies (e.g., Deconinck et al. 2006), archeology (e.g., Gluhak and Rosenberg 2013) and studies of soils and sediments (e.g., Arroyo et al. 2010).

Typically, solid samples are analyzed at a spatial resolution of 10 – 150 µm using single spot measurements. Alternatively, a continuous trace element profile can be measured as a line scan with scan speeds ranging from 1 – 200 $\mu m\,s^{-1}$. Subsequently, the data, which are recorded as ion intensities by the mass spectrometer, have to be converted into element concentrations. This is conventionally done using commercial software or self-developed in-house spreadsheets.

Several commercial programs for handling LA-ICPMS trace element data are available. Each of these software packages has its specific advantages and disadvantages. Probably the most widely used software is GLITTER (www.glitter-gemoc.com, Griffin et al. 2008), which allows calculating the concentrations from single spot measurements using one reference material for calibration and is hosted on Windows. SILLS (Guillong et al. 2008) is available for free from the ETH, Zürich, and can, in addition to data reduction of homogeneous materials, be used for analysis of fluid, melt and mineral inclusions and offers the possibility to use multiple reference materials for calibration. SILLS is MATLAB-based (The MathWorks, Inc.) and has a graphical user interface. Another commercial software commonly used for reduction of LA-ICPMS trace element data is IOLITE (Hellstrom et al. 2008), which is built using modules and requires an Igor Pro license that must be obtained together with the software. (Solari and Tanner 2011) published an R script for reduction and calculation of LA-ICPMS data for U-Pb geochronology. This script runs only under Windows and the purpose is solely the calculation of U-Pb ages. (Rittner and Mueller 2012) published an add-on package (LAICPMS) for 2D mapping of LA-ICPMS trace element distributions using R. This package is not available any more using the standard CRAN servers (pers. Comm. Müller W., RHUL, UK).

Here we present a script (TERMITE) for evaluation of LA-ICPMS trace element data based on an Excel in-house spreadsheet used at the Max Planck Institute for Chemistry (MPIC), Mainz. TERMITE is written in the statistical language R (R Core Team 2016), which is open-source software and provides several powerful statistical and graphical features as well as a strong user support by the R community. It is freely available from the Comprehensive R Archive Network (CRAN; https://cran.r-project.org/), which is an advantage compared to commercial software, such as Igor Pro or GLITTER. The aim of TERMITE is to satisfy the need for fast, open-source software for reduction of LA-ICPMS trace element raw data. Both spot analyses and line scan data can be evaluated, and the script can handle data from different mass spectrometers. The script is user friendly and allows all important parameters to be changed manually. In particular, TERMITE allows using several different reference materials, which are analyzed before and after the sample in order to correct for elemental fractionation and other potential effects occurring during ablation. The list of reference materials can easily be expanded and modified by the user. In addition, an optional outlier test is implemented, which minimizes the impact of artificial spikes introduced during the measurement. The calibrated data are provided both graphically and numerically. Data evaluation using TERMITE is much faster than with all other currently available software. The concentrations of more than 100 single spot measurements (we tested up to 24,000 spot measurements) can be calculated in less than a minute. Currently, TERMITE allows to reduce data recorded by two different mass spectrometers (Agilent 7500ce and Thermo Scientific Element2), which are widely used in the laser ablation community. However, the script can easily be adapted to other systems and file formats by the user.

4.2 TERMITE

TERMITE uses isotopic abundances and relative atomic masses provided on the website of the National Institute of Standards and Technology (NIST; http://nist.gov/pml/data/comp.cfm; Coursey et al. 2015) and includes reference values for various reference materials. Currently implemented are the reference materials BAM-S005B, MPI-DING ATHO-G, KL2-G, StHs6/80-G and T1-G, NIST SRM 610 and SRM 612, using the “preferred values” provided by the GeoReM database (http://georem.mpch-mainz.de.gwdg.de, Application Version 19; Jochum et al. 2005). For USGS MACS-1 and MACS-3, the preliminary reference values provided by the USGS (S. Wilson, USGS, unpublished, in Jochum et al. 2012) are used, which are in agreement with the compiled data of the GeoReM database. In the following, we outline and explain the individual steps performed by TERMITE in detail. Detailed step-by-step instructions for the installation of R and the application of TERMITE are given in the supplemental material.

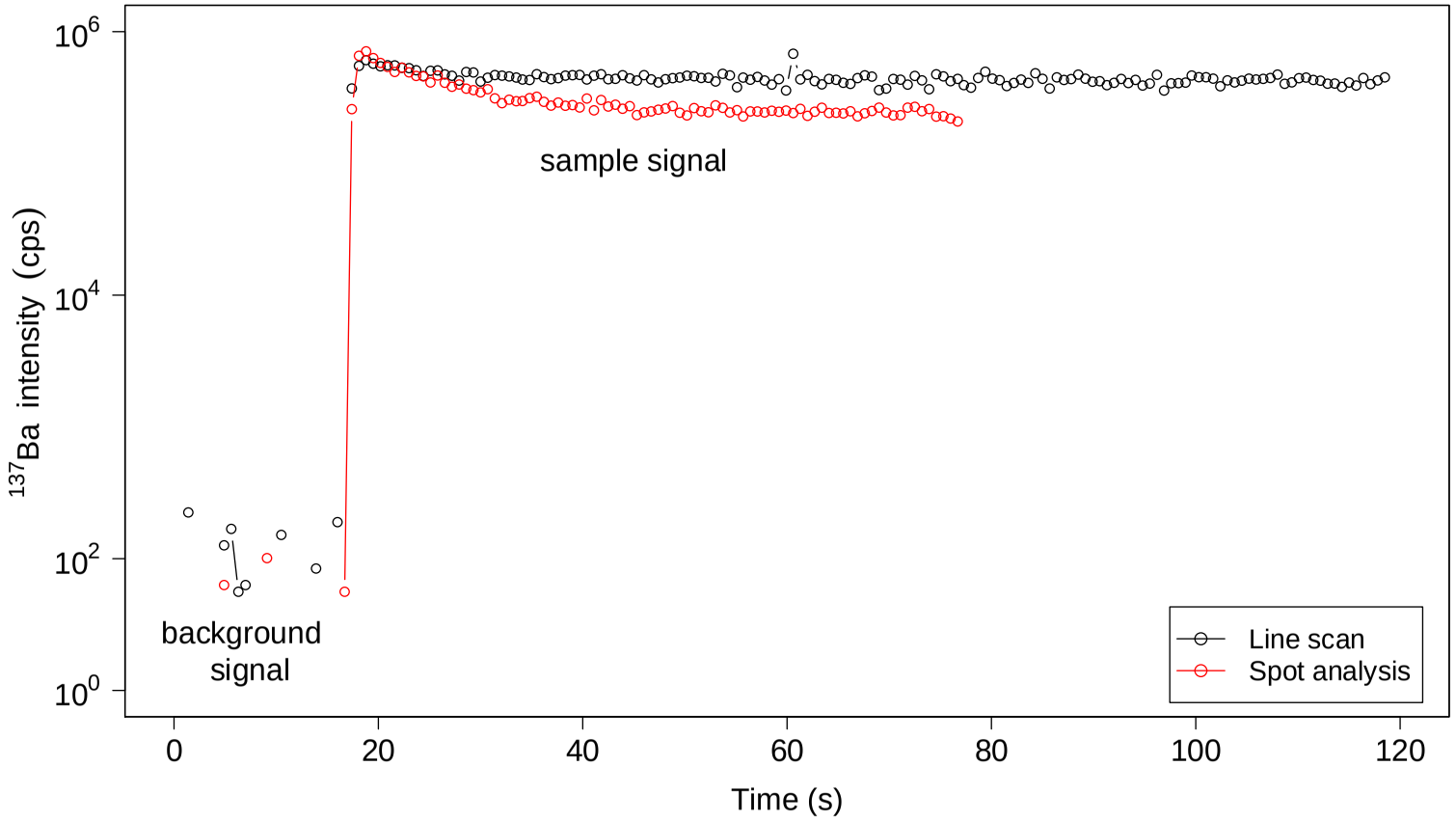

Figure 4.1: Typical evolution of a time-resolved LA-ICPMS signal. The background signal (laser firing with shutter closed) is clearly distinguishable from the sample signal (laser firing with shutter open). Shown are the intensities for ^{137}Ba from a line scan (black) using a scan speed of 5 µm s^{-1} and a spot size of 100 µm as well as from a single spot analysis (red) using a spot size of 100 µm, respectively. Both analyses were performed applying a pulse repetition rate of 10 HZ on the reference material NIST SRM 612 using a New Wave UP213 laser system coupled to a Thermo Scientific Element2 ICPMS.

4.2.1 Laser ablation signals

Figure 4.1 shows a typical time-resolved signal obtained during LA-ICPMS analysis for an arbitrarily selected mass, with the background and the sample signal highlighted.

Prior to each ablation, the background signal is recorded. The intensity of the background signal has to be determined (Longerich et al. 1996) by calculating the mean or the median of the measured count rates (Figure 4.1) of the corresponding interval. We suggest using the median since it is more robust in the presence of outliers. However, TERMITE offers both options.

For spot measurements, TERMITE uses the same values for the beginning and the duration of an analytical run (e.g., begin and end of background measurement and ablation) for all spots measured on the reference materials and samples, respectively. Furthermore, the script assumes that the same analytical parameters were used for all samples and reference materials (e.g., background time, ablation time). To avoid a potential bias of the calculated concentrations by potential surface contamination to the signal of interest, a specific amount of data points at the beginning of each ablation should be truncated (Figure 4.2). The same is advised for the background signal, where typically the first two and the last two values are truncated (Figure 4.2). This is especially important if a lot of isotopes are measured, since the laser needs some sweeps to settle.

For line scans and speleothem analysis, the ablation on the sample is usually longer than on the reference materials. However, for specific samples, such as dust (e.g. Macholdt et al. 2014), ostracods (e.g. Yang et al. 2014) or inclusions (e.g. Kotzeva et al. 2011), the line scan on the sample may also be shorter than the measurements on the reference material. Figure 4.3 shows an example where a line scan measurement on a stalagmite sample (HLK2) is compared with the signal of a line scan measurement on a reference material. The speed of the movement of the laser ablation stage and the time step of the ablation allows plotting the line scan data against distance. In contrast to spot measurements, the first values of a line scan measurement are commonly not truncated since most laboratories routinely perform a preablation scan on the sample, minimizing surface contamination (Figure 4.3).

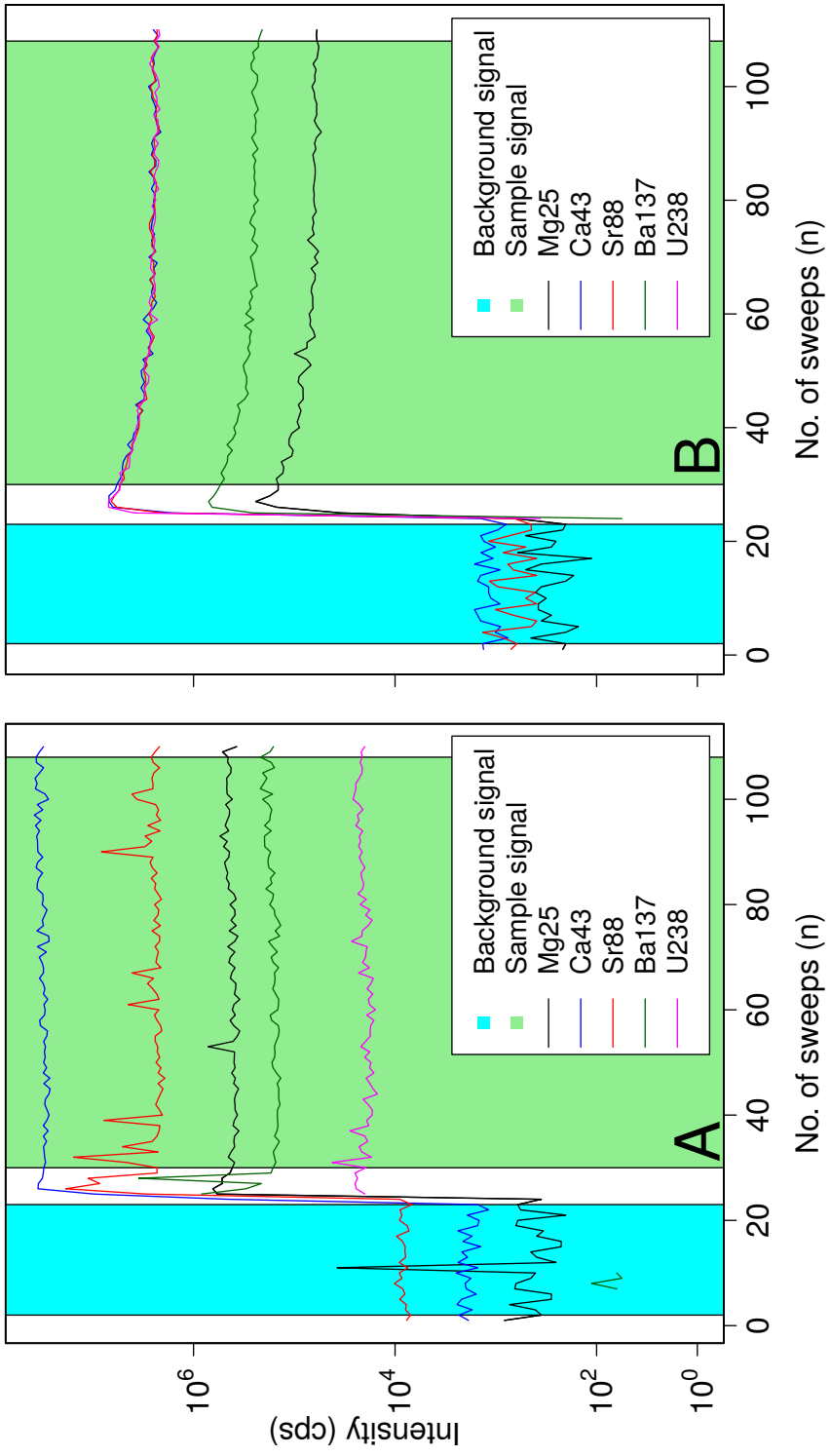

Figure 4.2: Temporal evolution of the raw intensities of a spot measurement on a stalagmite sample (A) and NIST SRM 612 (B), respectively. The boxes indicate the sections used for the calculation of the background (blue) and the ablation signal (green), respectively. For clarity, only selected isotopes are shown.

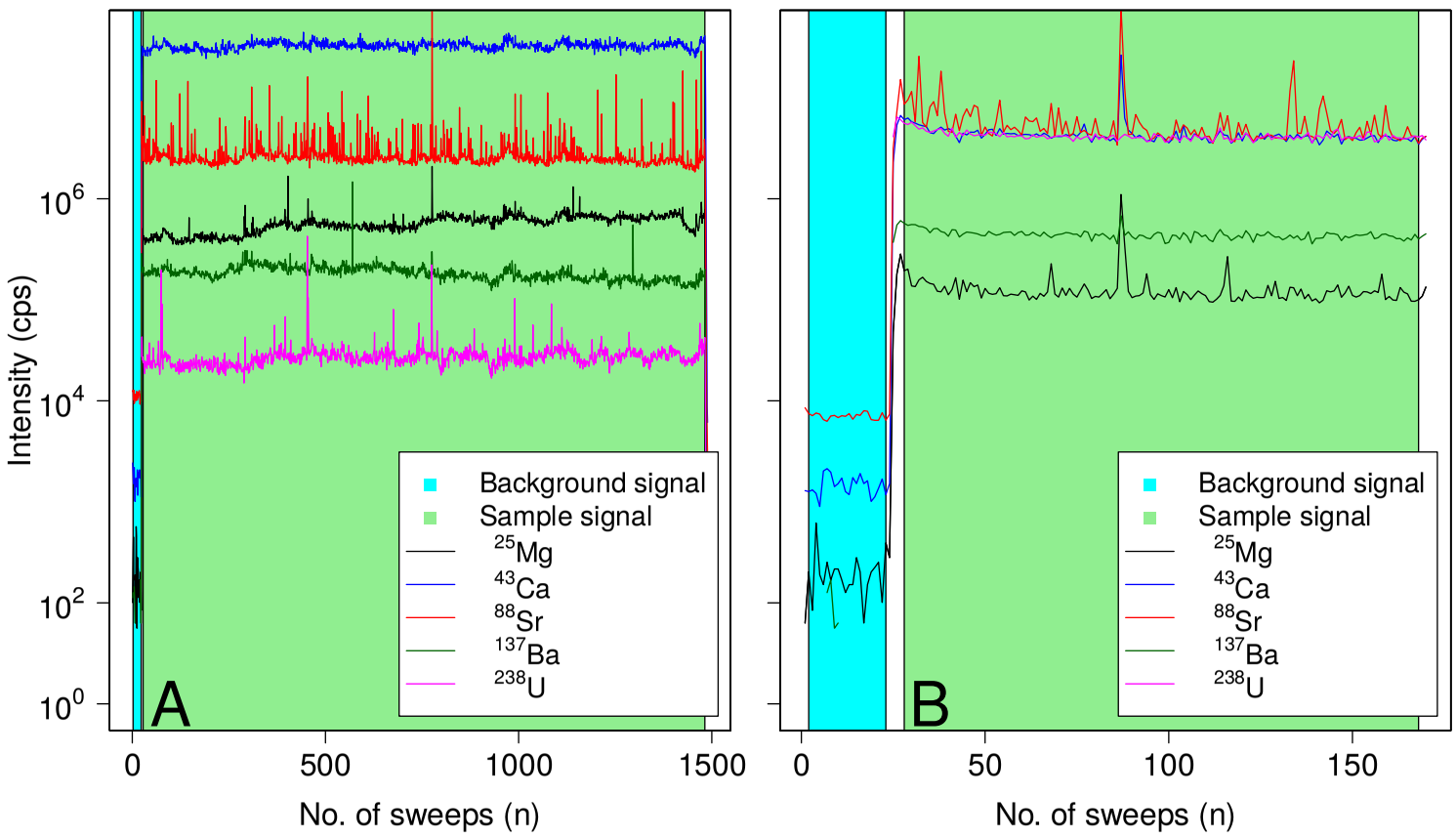

Figure 4.3: Temporal evolution of the raw intensities of a line scan measurement on a stalagmite sample (A) and NIST SRM 612 (B), respectively. The boxes indicate the sections used for calculation of the background (blue) and ablation signals (green), respectively. Note that the number of sweeps (n) of the background signal is the same for both measurements (17 s, n=24). However, the number of sweeps for the line scan measurement on the sample (1038 s, n=1490) is much larger than for NIST SRM 612 (118 s, n=170). For clarity, only selected isotopes are shown.

4.2.2 Calculations performed during data reduction

In this chapter, we briefly summarize the calculations performed by the TERMITE. A detailed description of the corresponding calculations is, for instance, given by Longerich et al. (1996) and Jochum et al. (2012). Firstly, the background signal is subtracted from the sample signal for all measured isotopes. Furthermore, all measured ion intensities of one experiment are normalized to the (background corrected) signal of the internal standard (Equation 4.1):

$$I_{norm} = \frac{I_{sample\ raw} - BG}{I_{IS} - BG_{IS}} \tag{4.1}$$

where $I_{sample\ raw}$ is the raw intensity of a selected isotope, BG is the median of the background signal of the corresponding isotope, I_{IS} is the raw intensity of the internal standard, and BG_{IS} is the median of the background signal of the internal standard. The user can also choose to apply the mean background value. In order to prevent calculation of a zero limit of detection, all values of 0 cps are replacedby 1 cps prior to the calculation of the background (Longerich et al. 1996).

In the next step, an outlier test can be performed for both the samples and the reference materials (Equation 4.2):

$$I_{out} = median(I_{norm}) \pm median(I_{norm}) * \frac{m}{100} \tag{4.2}$$

where $median(I_{norm})$ is the median of the corresponding isotope normalized to the internal standard, and the parameter m defines the upper and lower boundary of the outlier test.

Figure 4.4 shows an example of the outlier test, with the rejected values highlighted. In this example, m is set to 30, which means that all values exceeding the 30 % range above and below the median of the signal are rejected. A lower value of m results in more rejected values, a higher value rejects fewer values. Outlier tests are best performed on homogeneous samples.

In the next step, an "uncorrected concentration" ($C_{El,uncorr}$, Equation 4.3) for each element is calculated using the mean of the values resulting from the outlier test (I_{out}, Equation 4.2):

$$C_{El,uncorr} = mean(I_{out}) * \left(\frac{IsoAb_{IS}}{IsoAb_{El}} * \frac{relAM_{EL}}{relAM_{IS}} \right) \tag{4.3}$$

where $IsoAb_{IS}$ is the isotopic abundance of the internal standard isotope, and $IsoAb_{El}$ is the isotopic abundance of the isotope of interest. $relAM_{El}$ is the relative atomic mass of the corresponding element, and $relAM_{IS}$ is the relative atomic mass of the internal standard element.

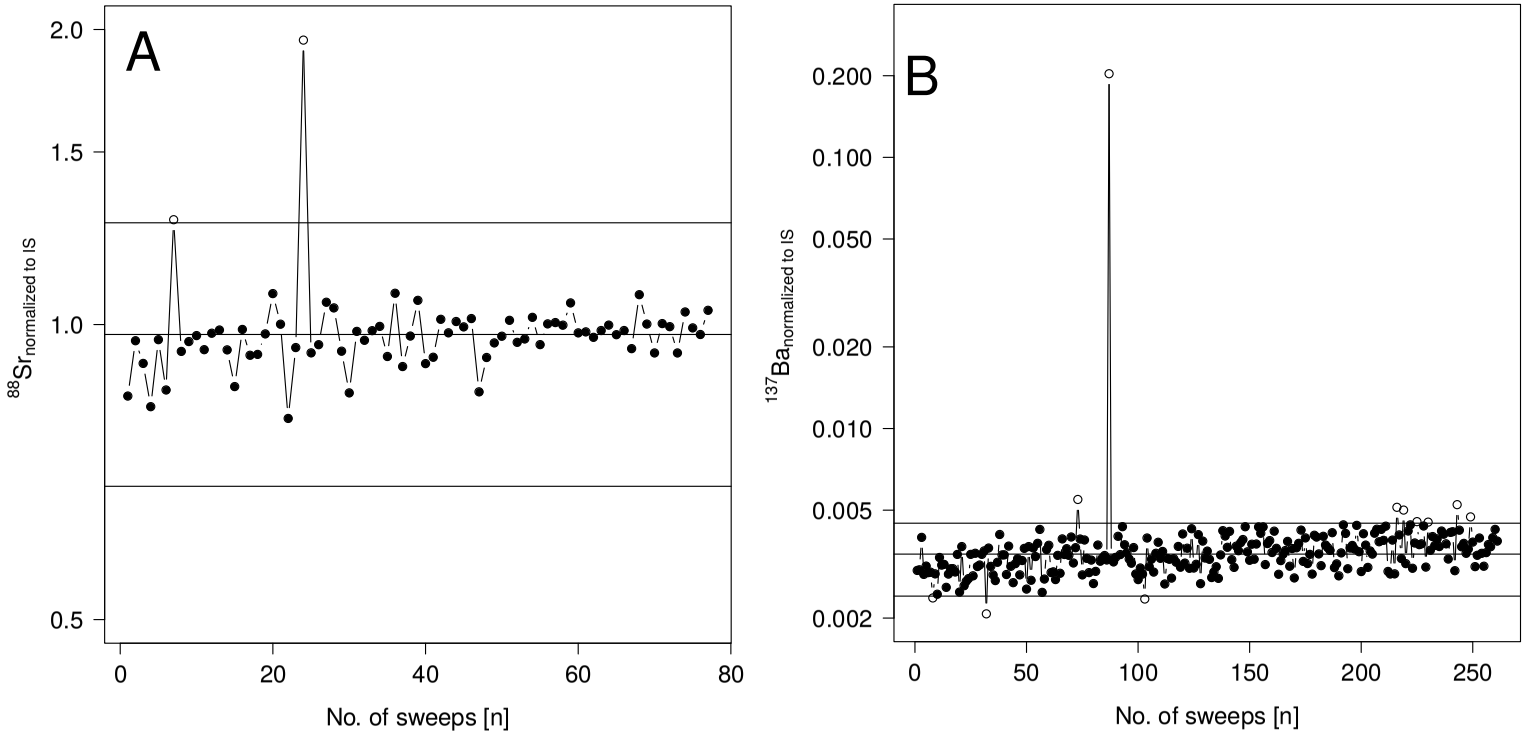

Figure 4.4: Effect of the outlier test performed during data reduction using a value of m=30%. Exemplarily shown is I_{norm} for ^{88}Sr on NIST SRM 612 (A) and ^{137}Ba (B) on a stalagmite sample. The filled black dots represent the values included by the test. The upper and lower horizontal lines indicate the 30 %-range around the median (middle horizontal line). The internal standard is ^{43}Ca.

Then, the uncorrected concentration of each element is compared with the "true" concentration of the element in the reference material (Longerich et al. 1996), and a relative sensitivity factor for each isotope (Equation 4.4) is calculated (Jochum et al. 2012):

$$RSF_{El} = \frac{C_{El,uncorr}}{C_{El,true}} \tag{4.4}$$

where $C_{El,uncorr}$ is the uncorrected concentration of the element obtained on the reference material, and $C_{El,true}$ is the "true" concentration of the reference material (i.e., the reference value listed in the GeoReM database). Figure 4.5 shows a comparison of the RSF values obtained for different isotopes during data acquisition. The RSF_{El} are finally used for the calculation of the concentrations of the individual elements (Equation 4.5) of the samples:

$$C_{corr} = \frac{C_{El,uncorr}}{RSF_{El}} \tag{4.5}$$

where $C_{El,uncorr}$ is the uncorrected concentration of an isotope measured on the sample, and RSF_{El} is the corresponding relative sensitivity factor for the isotope.

Finally, the "Limit of Detection" (LoD) is calculated according to Equation 4.6. The LoD uses the background signal to calculate the minimum concentration of a specific element, which can be distinguished from noise. The triple standard deviation of the background signal is used for the calculation of the LoD:

$$LoD = \frac{3 * SD(BG)}{mean(I_{sample\ raw})} * C_{El,true} \tag{4.6}$$

where SD(BG) is the standard deviation of the background, mean($I_{sample\ raw}$) is the mean of the signal during ablation, and $C_{El,true}$ is the concentration of the reference material. TERMITE uses the concentrations of the first reference material analyzed (in the example shown in Figure 4.5, NIST SRM 612) to calculate the LoD. If the concentration of a specific element is below the LoD, the value is set to NA (the logical constant for missing values in R).

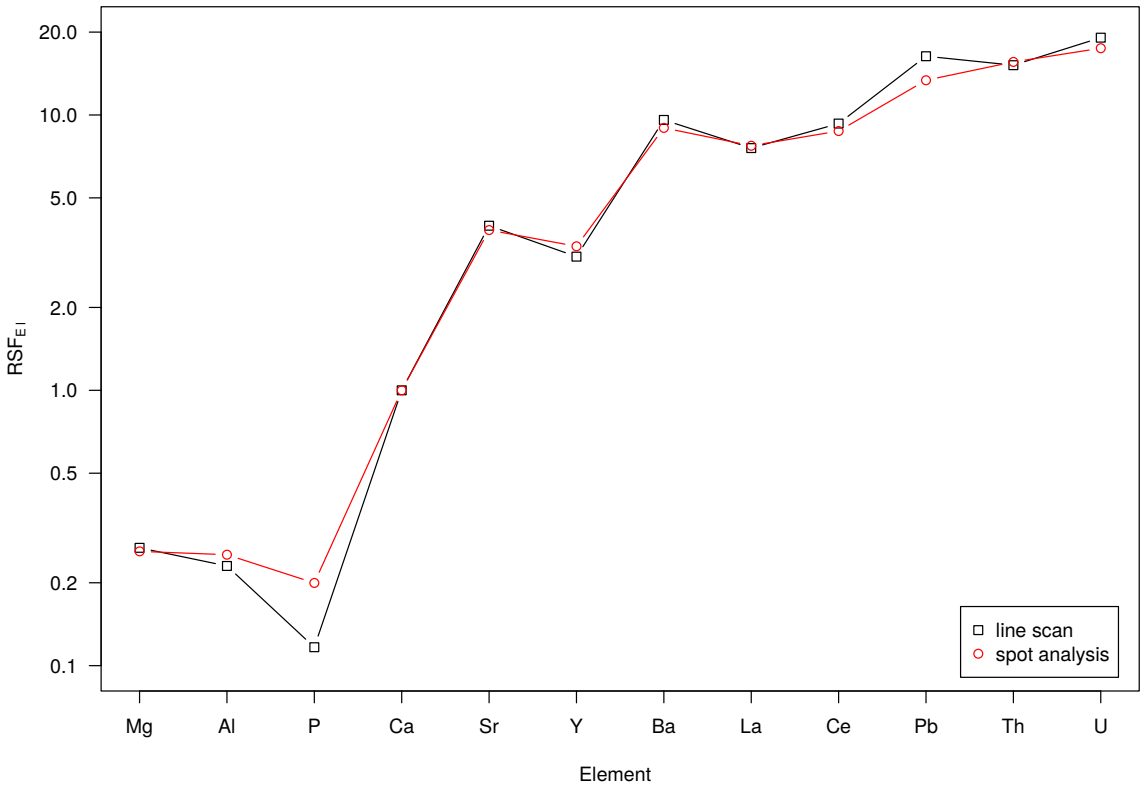

Figure 4.5: Relative sensitivity factors (RSF_{El}) calculated for different isotopes. Black squares show RSF_{El} obtained during a line scan measurement with a scan speed of 5 µm s^{-1}, whereas red spots represent RSF_{El} obtained during spot measurements. Both experiments were performed using a New Wave UP 213 laser ablation system coupled to a ThermoFischer Scientific Element2 ICPMS.

4.2.3 Output of data

The output of TERMITE comprises the following graphical (as .pdf-files) and numerical (as .csv-files) information:

1. The temporal evolution of the raw intensity of every isotope is presented in individual plots compiled in a .pdf-file. This is a visualization of the data recorded by the mass spectrometer. The timing and duration used to calculate the mean or median of the background and the sample signal, respectively, are indicated by vertical lines (Supplemental Figure C.1).

2. The LoD, calculated according to Equation 4.6 based on the first reference material

3. The relative sensitivity factors (RSF), calculated according to Equation 4.4.

4. The corrected element concentrations based on the measured isotopes

Currently, the script is capable of processing data from the two mass spectrometers used in this study (i.e., Element2 and Agilent 7500ce). The corrected data (i.e., the final results) are stored in .csv-files, which can be imported into a wide range of software for data analysis and visualization.

4.3 Comparison with other software for data reduction

For data reduction of LA-ICPMS data, a variety of software is available. Here we compare the performance of TERMITE with GLITTER 4.4.1 and an in-house Microsoft Excel spreadsheet used at the MPIC and the Johannes Gutenberg University, Mainz (JGU). The calculations performed by TERMITE are based on this spreadsheet (for details, see Jochum et al. 2007), and TERMITE is regularly used at JGU. Thus, the results are identical if the same parameters are used. Detailed information on the different software is provided in Table 4.1.

Table 4.1: Comparison of different software for data reduction of trace element measurements.

	TERMITE	GLITTER	Microsoft® Excel
Host environment	R	IDL	Microsoft® Office
Open source	Yes	No	No
Freeware	Yes	No	No
Operating System	Microsoft Windows Mac OS X Linux	Microsoft Windows Mac OS X Linux	Microsoft Windows Derivates on Mac OS X Unix
Spot analysis	Yes	Yes	Yes
Line scan analysis	Yes	No[1]	Yes

[1] Line scan measurements can be treated like spot measurements (see main text for details).

4.3.1 The in-house Excel spreadsheet

As explained above, TERMITE is an implementation of the in-house Excel sheet used at the MPIC and the JGU in R. Thus, both scripts calculate exactly the same results if all parameters are specified identically. The major difference between both methods is the way the data are handled. The Excel spreadsheet can only handle one dataset from the mass spectrometer at once. In addition, to enable calculation of the RSF, the reference materials need to be processed first. Then, the concentrations of the sample measurements can be calculated in another sheet. This procedure is very time consuming as well as prone to errors. Another disadvantage of the in-house Excel sheet is the need to individually open and save every processed data file separately. In addition, since every data file needs to be separately pasted into the calculation file, most of the time required for correction of the sample data is used by “Copy and Paste”. Another potential source of errors is that all equations are

applied to multiple rows and columns of a sheet. Thus, the results will be biased if columns and/or rows are missed. Most importantly, the spreadsheet needs to be adjusted to every new experiment in terms of analyzed isotopes, number of sweeps and reference materials used.

In summary, data reduction using the in-house Excel sheet is both time consuming and prone to errors due to the mechanical routine of copying and pasting data. An advantage of the Excel sheet, however, is that each element can be corrected individually, i.e., the timing and duration of the background and the sample analysis can be adjusted separately. For specific measurements, such as small and heterogeneous samples (e.g., for ostracod shells, Yang et al. 2014) this can be very useful. On the other hand, this practice may result in biasing the concentrations towards personal preferences on the basis of the personal understanding of the temporal evolution of the laser signal.

4.3.2 GLITTER

The software GLITTER is embedded in Microsoft Windows and, as a consequence, the main interfaces are organized in windows. This may be considered as an advantage of GLITTER because the users do not have to adapt to software they are not familiar with, as might be the case for R. The reference materials are found in the "Standards" menu, and the user has to select the reference material used for calibration from a drop down menu. Only one reference material per data reduction scheme can be used for calibration. The reference values are stored internally in the data library of GLITTER and can be updated by the user using a text editor. As with the in-house Excel sheet, the user can define the timing and duration used for the background and the sample calculations manually for each single spot measurement. This is done based on a visualization of the data in the "Review" window, which enables the user to define the corresponding values. These values are then used for all elements measured during the corresponding spot analysis. The user can adjust important parameters, and all calculations are performed on-line. The theory behind the calculations of GLITTER can be found in the manual for GLITTER Version 4.4, which can be accessed on the GLITTER homepage. A major disadvantage of GLITTER is that it can only be used to evaluate spot measurements. Line scan measurements can be evaluated, but are treated as spot measurements, resulting in an average concentration per scan. However, if the user is interested in the temporal evolution of the signal along the line, for instance, in paleoclimate studies with (sub)-annual resolution or small scale changes in fabrics, this is not useful.

GLITTER allows the user to define the timing and duration used for the calculation of the background and the sample signal, respectively, for each individual measurement (Figure 4.6B). This may be useful for some applications, but also bears the risk of biasing the concentrations towards personal preferences. In other words, different users may obtain different results if they have different opinions/philosophies about how to evaluate the data (e.g., including or excluding spikes from the signal selection, Figure 4.6B). In order to quan-

tify this effect, we asked differently experienced users to evaluate the same data set using GLITTER and compared the results with TERMITE. Figure 4.6 shows a comparison of the Ba concentration measured using single spot analyses on a stalagmite sample from Central Germany (HLK2) determined with TERMITE and by three different users using GLITTER Figure 4.6A). The results are very similar. The exception is one large peak in the Ba concentration (Spot #24), which is only visible in the profile evaluated using GLITTER and only by users #2 and #3. This peak is caused by spikes in the laser signal, which have not been truncated by the users (Figure 4.6B), resulting in a higher concentration than calculated by TERMITE. The same applies to spot #40, where a large spike occurs in the background section of Ba (Figure 4.6C). Nevertheless, this spike has been included by all GLITTER users. This results in an artificially elevated background (mean background: 2427 cps, Figure 4.6C), which, in turn, results in a lower final concentration (Figure 4.6A).

This example shows that such artificial spikes or outliers may result in final concentrations varying in this case by a factor of ∼2. As tested by the authors, TERMITE calculates a similarly biased concentration if the mean is used for calculation of the background. Since the median is less susceptible to exceptionally large values in the background data than the mean, we advise to use the median for calculation of the background values. This also implies that it is not necessary to manually adjust the range used for the background determination. In addition, the outlier test performed by TERMITE detects and removes outliers in the sample signal to obtain robust final results.

4.4 Application

4.4.1 Methods

We briefly demonstrate the application of TERMITE using laser ablation data obtained at the MPIC. The measurements were conducted with a Thermo Scientific ELEMENT2 ICP single-collector sector-field mass spectrometer coupled with a New Wave Research Nd:YAG UP213 nm laser system, which is equipped with a Large Format Cell (LFC). All instrumental parameters were optimized prior to analysis as described by (Jochum et al. 2007; 2012).

4.4.2 Samples

We analyzed a section of the Holocene stalagmite HLK2 from the Herbstlabyrinth (HL) cave system, Central Germany. HLK2 is 15 cm long and grew on top of a slightly movable block in a small chamber inside the cave system. Further details about the HL cave system and stalagmite HLK2 are provided in (Mischel et al. 2015; accepted). We chose a small subsection of HLK2, composed of milky, opaque calcite suddenly changing to clear, translucent material (Figure 4.7). This section has previously been analyzed by (Mischel et al. accepted). Here we re-analyzed the subsection using both spot measurements (100 µm spot size) and line scans

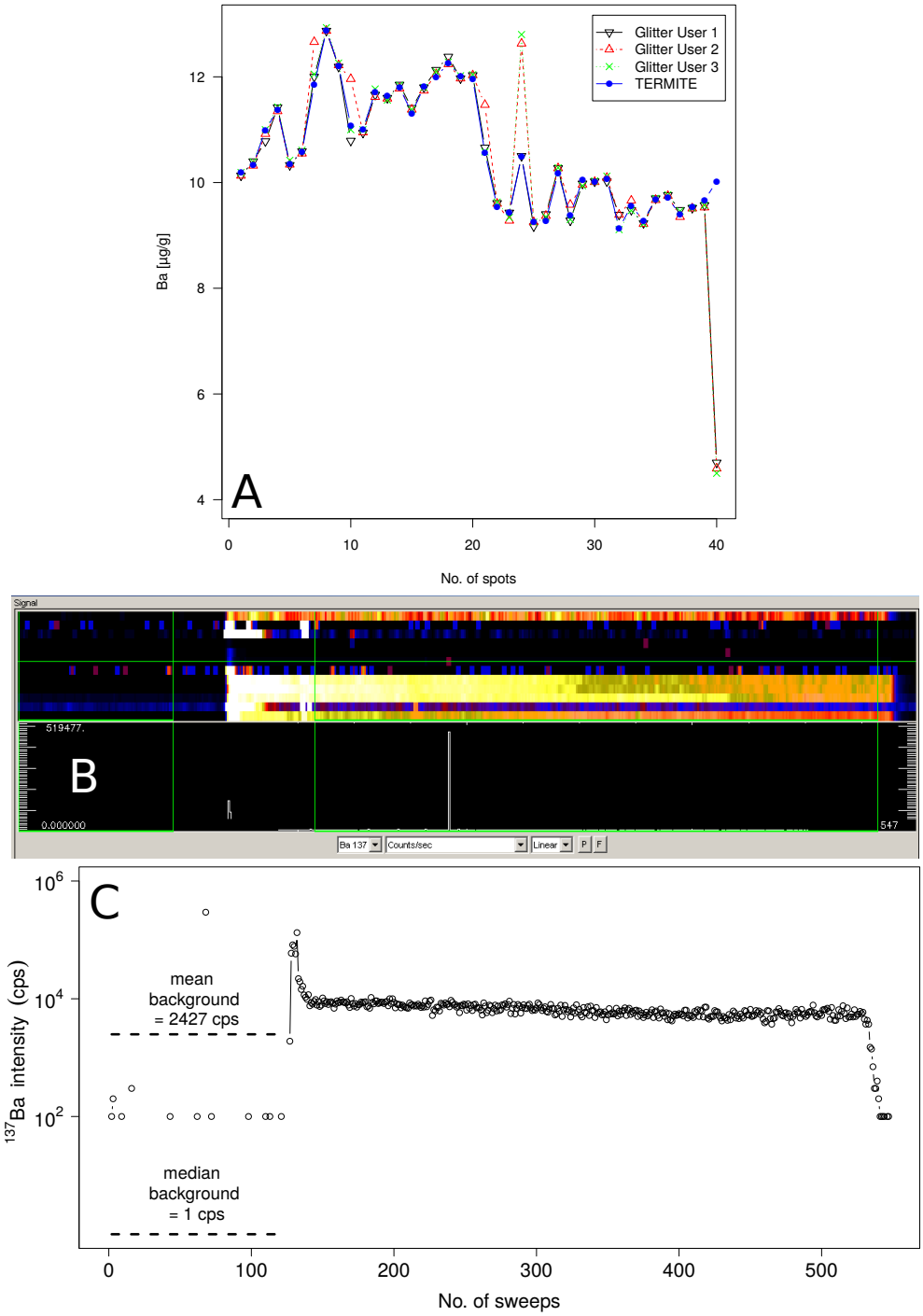

Figure 4.6: A: Comparison of Ba concentration measured on stalagmite HLK2, evaluated by TERMITE and three different users using GLITTER. All measurements were calibrated against NIST SRM 612. B: "Review signal" window of GLITTER showing the raw count rate for ^{137}Ba, where users can decide, which part of signal is used for data reduction. Signal shown corresponds to spot #24 on speleothem HLK2. C: Evolution of raw count rate for spot #40 on speleothem HLK2. Also shown are mean and median of background signal.

with a scan speed of 5 µm s^{-1}. As the speleothem is a heterogeneous natural sample, small scale differences in the elemental composition of parallel tracks cannot be excluded.

4.4.3 Results

Figure 4.8 shows the Mg concentration of HLK2 obtained by the different methods as calculated by TERMITE. In general, the results are very similar for the spot and the line scan analyses. The line scan data show some distinct large peaks. Potential reasons for these peaks are the release of artificial particles from the transport tubing or the laser ablation cell (Liu et al. 2001; Wang et al. 2006), which are detected by the mass spectrometer. During the data reduction of line scan data, no outlier test is performed. Thus, we emphasize that the user should be cautious to interpret these spikes as real fluctuations in the trace element content of their sample and potentially delete them subsequent to data reduction. The spot measurements obtained by the LA-ICPMS system reproduce the general trend of the line scan data (Figure 4.8). Evaluating a line scan with GLITTER would result in an average concentration similar to the mean of the line scan. However, as the speleothem sample is a heterogeneous sample, this result is not useful. Another important fact to mention is the different temporal resolution of line scans compared to spot measurements. Speleothem HLK2 shows growth rates of about 10 µm a^{-1} in the analyzed section (Mischel et al. accepted). Therefore, one spot equals 10 years, and the spacing of 125 µm results in one measurement every 12-14 years. The ablation time for one year of stalagmite growth approximates 2 seconds.

4.5 Conclusions

We developed an R script (TERMITE) to evaluate LA-ICPMS data. The major advantages of TERMITE are:

I. Even large datasets can be handled (we tested a data set consisting of more than 24,000 single spot measurements).

II. TERMITE can evaluate data obtained using single spot analyses as well as line scan measurements.

III. TERMITE performs an optional statistical outlier test with a flexibly adjustable range.

IV. Once the parameters required for evaluation have been specified, the evaluation is extremely fast (less than a minute for ca. 100 single spot measurements).

V. TERMITE allows using up to 10 reference materials for calibration at once, and further reference materials can easily be implemented. Compiled/preferred values for various reference materials as provided by the GeoReM database are included. This file can be updated by the user.

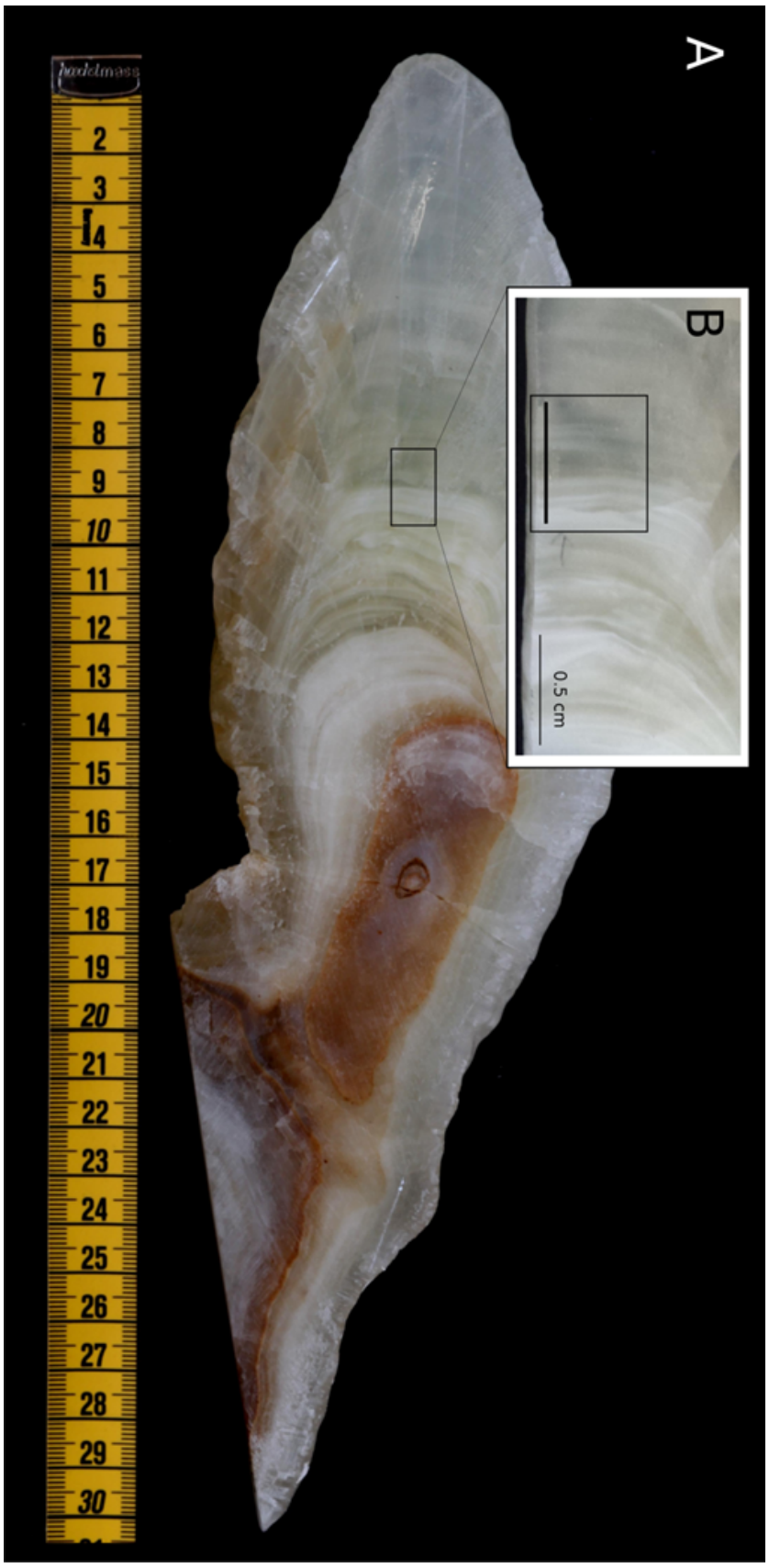

Figure 4.7: A: Photograph of stalagmite HLK2 after cutting. Further details are given in (Mischel et al. accepted). B: Detail of analyzed section framed by a black box and black line indicating laser ablation track.

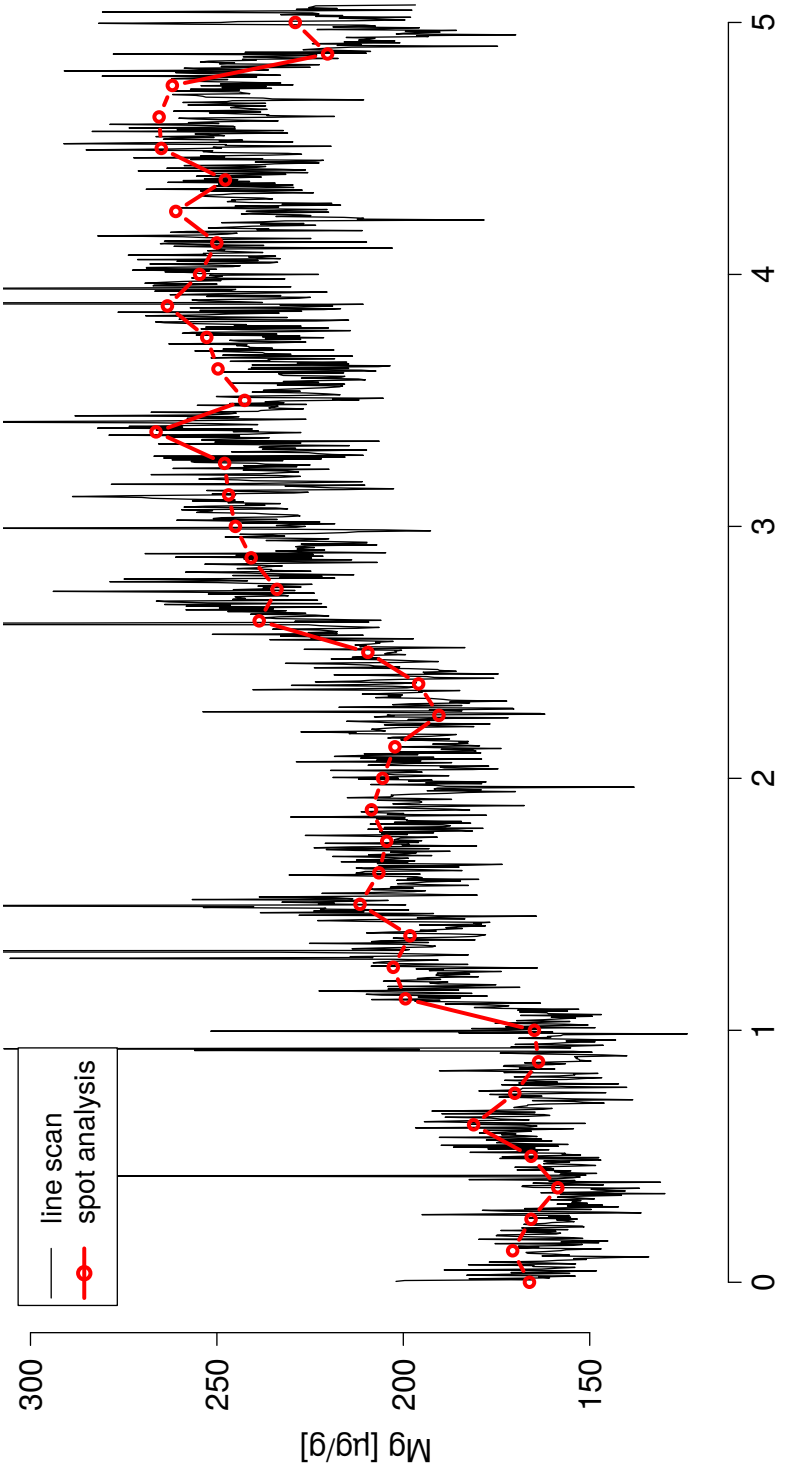

Figure 4.8: Concentration of Mg along a transect analyzed on stalagmite HLK2. Black curve shows concentration resulting from a line scan with a scan speed of $5\,\mu m\,s^{-1}a^{-1}$. Red dots are spot analyzes with a spot size of 100 µm and a midpoint spacing of 125 µm.

VI. The resulting data are provided both in graphical and numerical form and can be exported for further evaluation using other software.

VII. TERMITE provides reproducible results, which cannot be biased due to potential preferences of individual users.

VIII. TERMITE is written in the statistical software R, which is open-source software and can be obtained at no charge from CRAN.

Acknowledgments

Simon A. Mischel and Denis Scholz are thankful to the German Research Foundation (DFG) for funding (SCHO 1274/3-1, SCHO 1274/9-1). We also thank Brigitte Stoll and Ulrike Weis, MPIC, for assistance during LA-ICPMS analysis and fruitful discussions. We thank the Speläologische Arbeitsgemeinschaft (SAH eV.) for support at the Herbstlabyrinth cave and Maria Mischel for helpful discussions.

5 Conclusion

Working with speleothems from the HL cave system has several advantages. Almost all parts of the HL cave system are decorated with different kinds of speleothems. Preliminary work showed that all white and translucent speleothems grew during the Holocene. The opportunity of sampling Holocene material for paleoclimate research is unprecedented.

One aim of this work was the combination of cave monitoring data with the geochemical proxies of the speleothems. Therefore, an extensive cave monitoring was set up in a small chamber, the "Kleine Kammer", next to speleothem HLK2. Monthly aliquots of precipitation, soil water and different cave drip waters were sampled and geochemically analysed. After 5 years of monitoring a clear seasonal cycle became visible in the drip water δ^{18}O values and the data measured by various loggers at the cave site. Using these data investigations started by developing a forward model which uses meteorological climate station data situated around the cave. With this data extending the cave monitoring data to a series of 144 years of cave site corrected data was possible. All important parameters for the drip water δ^{18}O model were available and on that basis a detailed investigation on the influence of the NAO and the cave drip water δ^{18}O values was possible. The modelled results highlights the importance of well choosen research areas for reconstructing the NAO . Even though the research area of the HL cave system is situated in a NAO sensitive region, reconstruction of the NAO using speleothems from that area remain challanging, due to the fact, that the clear winter signal of the NAO is biased due to summer rainfall events. In addition, the NAO varies from year to year, therefore climate archives with sufficient resolution, e.g. sub-annual and seasonal, are urgently needed for reconstructing the NAO. The results of stalagmite HLK2 revealed slow growth rates of approximately 10 µm a^{-1}, pointing to the fact that reconstructions of the inter-annual NAO remains challanging using speleothems from the HL cave system. This is owed to the fact that the speleothems from the HL grew slow but rather constantly.

Speleothem HLK2 grew during the Holocene, covering the Late Glacial and the complete Holocene, it was obvious, that replicate records of Holocene climate variabilty can be obtained from the cave. Coeval stalagmites are needed to show to what extend the speleothems from the HL cave system could reach into the past. To achive this, two additional stalagmites from the HL cave system were sampled and analysed in detail. This enabled us to compare three Holocene samples from different parts of the cave with each other. One important method to achive this was by performing Principal Component Analysis (PCA). Apparently, the PCA showed striking similarities in all three stalagmites, which can be directly linked to

the productivity of the vegetation at the cave area. This analysis also revealed important connections between the polar North Atlantic with the cave site.

A powerful tool in analysing large data sets, namely in this work all logger data and speleothem proxy data, is the graphical and statistical language R. This software is more a toolbox than a single piece of software and it has almost no limitations in possible tasks which can be performed. Powerful statistical calculations can easily be performed as well as plotting time resolved data on standardized POSIX format. R was used for the calculation of the drip water $\delta^{18}O$ model as well as for analysing the cave monitoring and the speleothem proxy data. During the analysis of the stalagmites one widely used application is LA-ICPMS. As there is only spreadsheet software or commercial software available for data reduction, an obvious task was the implementation of the calculations in a script written in R. The final product TERMITE is a fast way of calculating trace element concentrations. TERMITE provides a tool for the analysis of trace element data obtained with two different mass spectrometers and a main advantage of the software is the capability of using more than one reference material for the correction of the data. In addition, the software is open-source and is made available for public use. New features can easily implemented and the script can extended to fit the need of the users.

5.1 Outlook

Using speleothems from the HL cave system offer great potential for paleoclimate reconstructions, which can enhance our understanding of past climate variability. Knowledge of the past is important to understand futere climate change and predict future climate scenarios. With the present study a solid basis for the interpretation of speleothem data was build. These speleothems cover the Holocene and the Late Glacial. The statistical calculations offers a robust way of extracting paleoclimate information. Nevertheless, these methods can further expanded by performing different multivariate analysis and analysing data sets using frequency analysis or similar methods used for the examination of time series in greater detail.

The HL cave system consist of passages with 11 km length shared on multiple levels with a lot of speleothems, more samples of different times during the Quaternary can be analysed. For example one interesting sample is the bottom part of HLK2, dated to an age of 58 to 65 ka BP. Another promising sample is one stalagmite which grew between 92 and 106 ka BP. Unfortunately, MIS 5e, the Eemian, the last warm period comparable to the Holocene, is still missing. Nevertheless, some promising samples are already available for further analysis. The speleothems from the HL cave system should be compared in detail with other speleothems from German cave systems.

The cave monitoring program set up in the cave for the last 5 years gave an extensive data set. Most of the already published data consists of monthly data. Some promising small scale processes occuring at the short time scale (e.g., hours to days) still need more consideration

to be interpreted. The loggers record relevant cave climate parameters with hourly resolution and these data can be combined to analyse such processes. Most of the data of this PhD thesis is gathered in the second level of the cave system. The upper and lower levels are just briefly analysed in terms of cave climate monitoring and the speleothem sampling location is also at the second level.

Maps from the isotopic distribution over central Germany for different time slices throughout the Holocene can be reconstructed using speleothem data. Together with cave monitoring data distribution maps of past rainfall and past vegetation distribution can be obtained. The data from the speleothems can help to refine computer simulated climate models of past climate and they can help to enhance our understanding of future climate change.

Using R for trace element data reduction is quite a fast way of obtaining reliable results for speleothem analysis. The script TERMITE should be directly coupled with the algorithm StalAge to be able to combine these important tools in speleothem research. Multivariate statistics can be calculated using R. The datasets from the proxy records of the speleothems are suitable for detailed anaylsis in terms of statistical methods. The PCA of the stalagmites revealed a 1.5 ka cycle of the productivity of the vegetation. With the knowledge of the influenceing factors and the processes affecting the trace elements and stable isotope values of the speleothems a detailed research should be conducted using frequency analysis.

A Electronical Supplement - δ^{18}O values of cave drip water

A.1 Appendix A

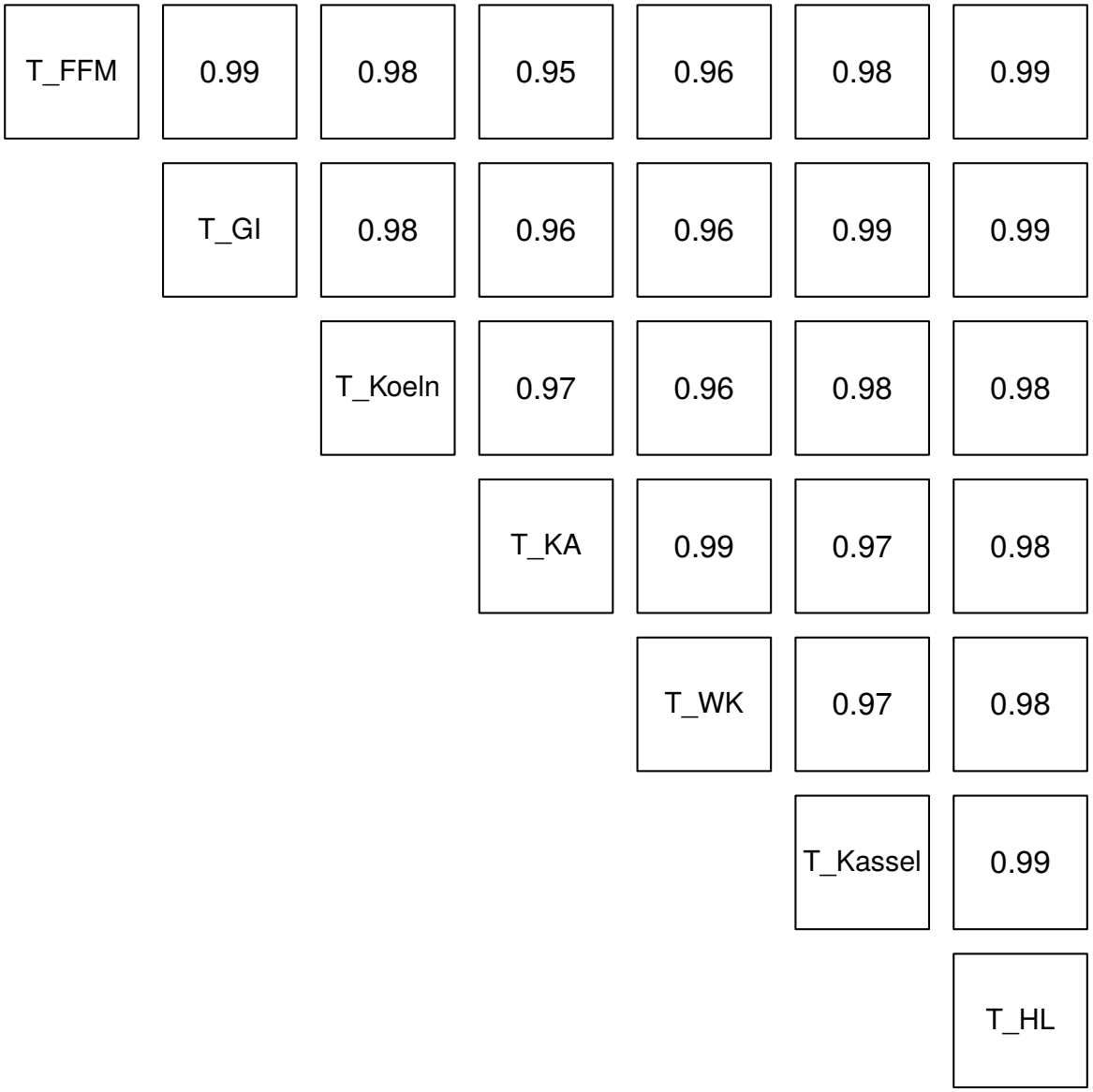

Figure A.1: Correlation matrix between daily temperature from the climate stations used in this study for the years 1949 - 2014. FFM: Frankfurt am Main; GI: Giessen; Koeln: Köln; KA: Kahler Asten; WK: Wasserkuppe/Rhön; Kassel: Kassel; HL: Herbstlabyrinth-Adventhöhle cave system. All correlations are significant with $p < 0.01$

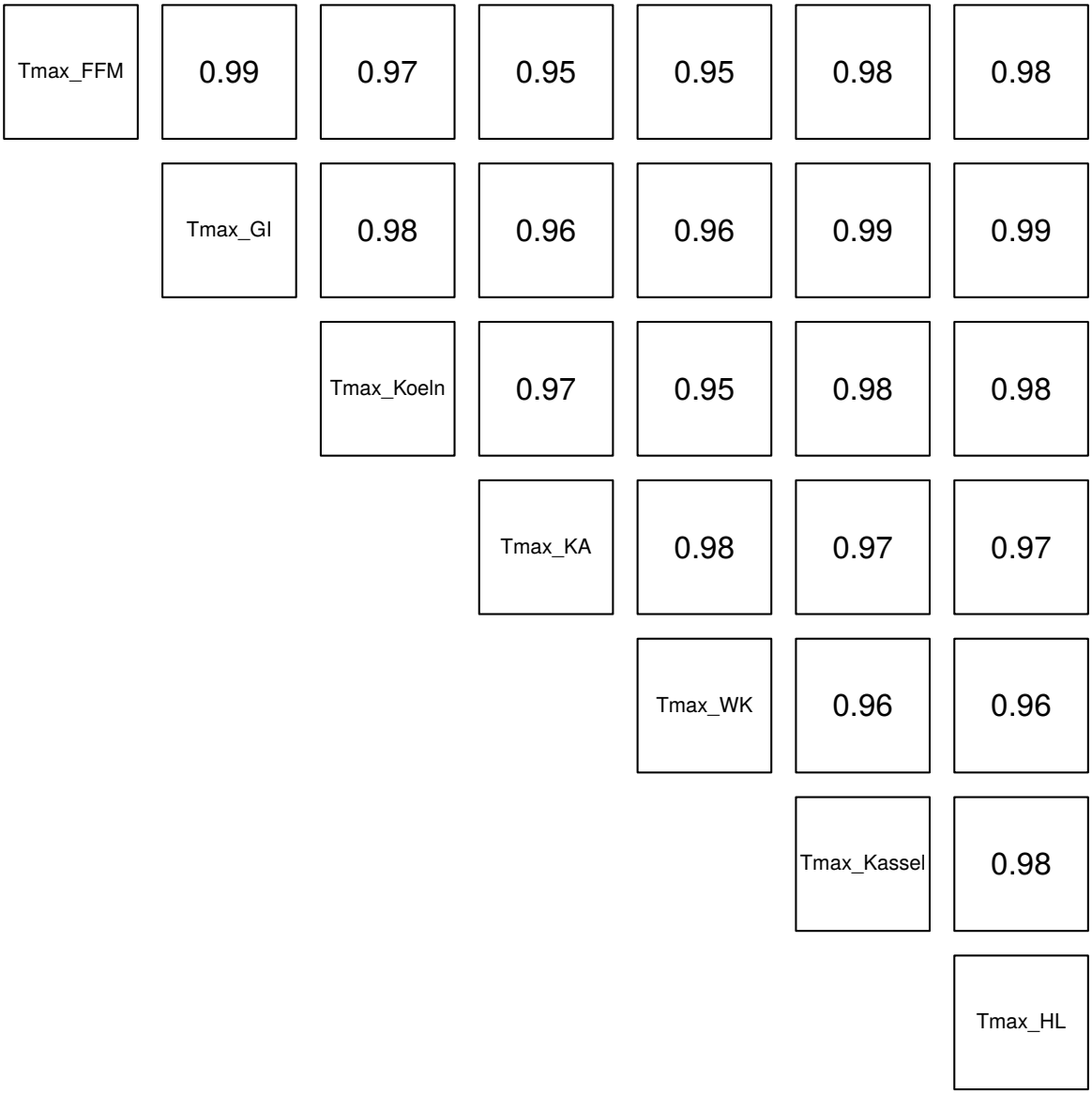

Figure A.2: Correlation matrix between maximum daily temperature from the climate stations used in this study for the years 1949 - 2014. FFM: Frankfurt am Main; GI: Giessen; Koeln: Köln; KA: Kahler Asten; WK: Wasserkuppe/Rhön; Kassel: Kassel; HL: Herbstlabyrinth-Adventhöhle cave system. All correlations are significant with $p < 0.01$

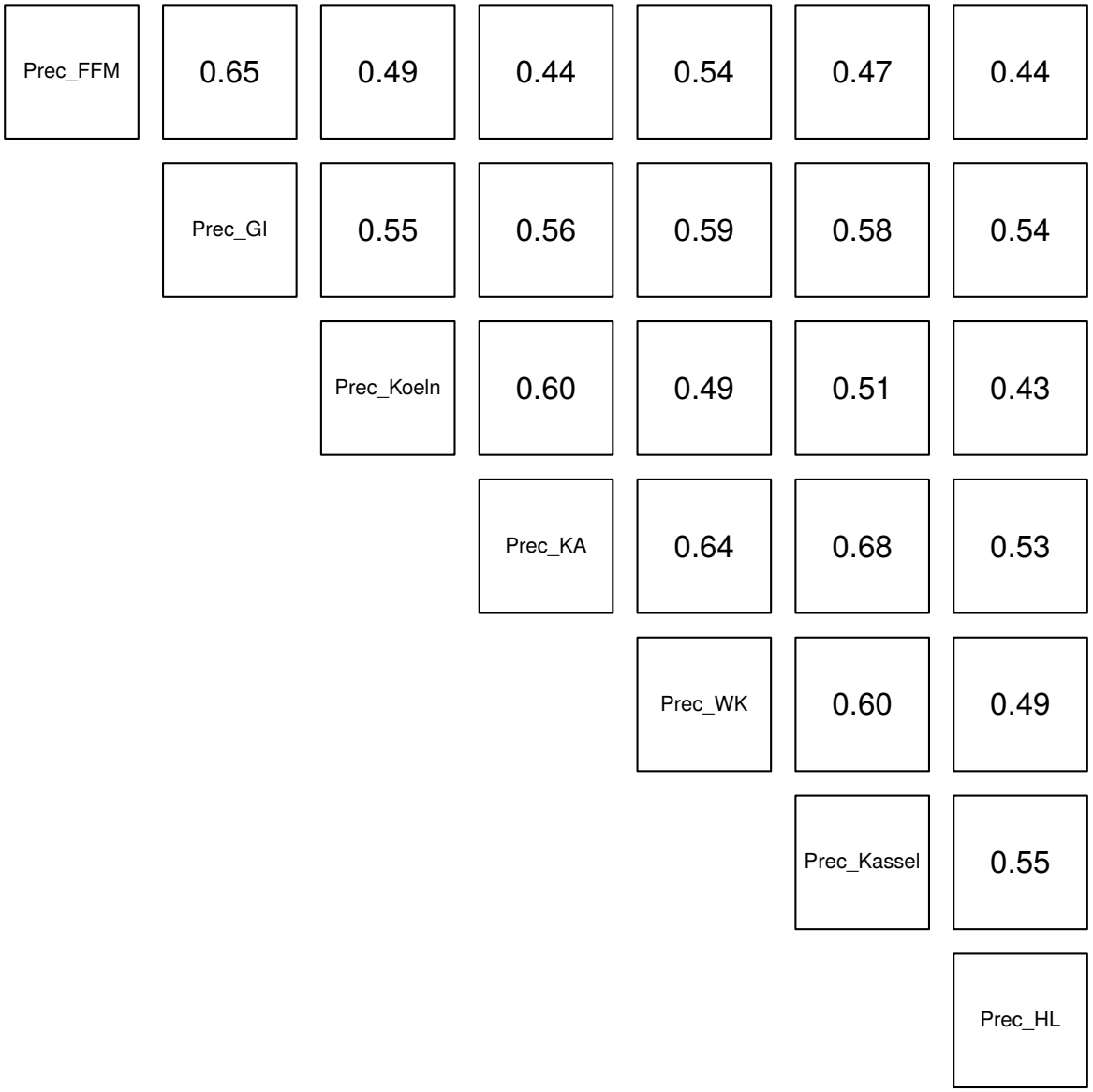

Figure A.3: Correlation matrix between daily precipitation for the climate stations used in this study for the years 1949 - 2014. FFM: Frankfurt am Main; GI: Giessen; Koeln: Köln; KA: Kahler Asten; WK: Wasserkuppe/Rhön; Kassel: Kassel; HL: Herbstlabyrinth-Adventhöhle cave system. All correlations are significant with $p < 0.01$

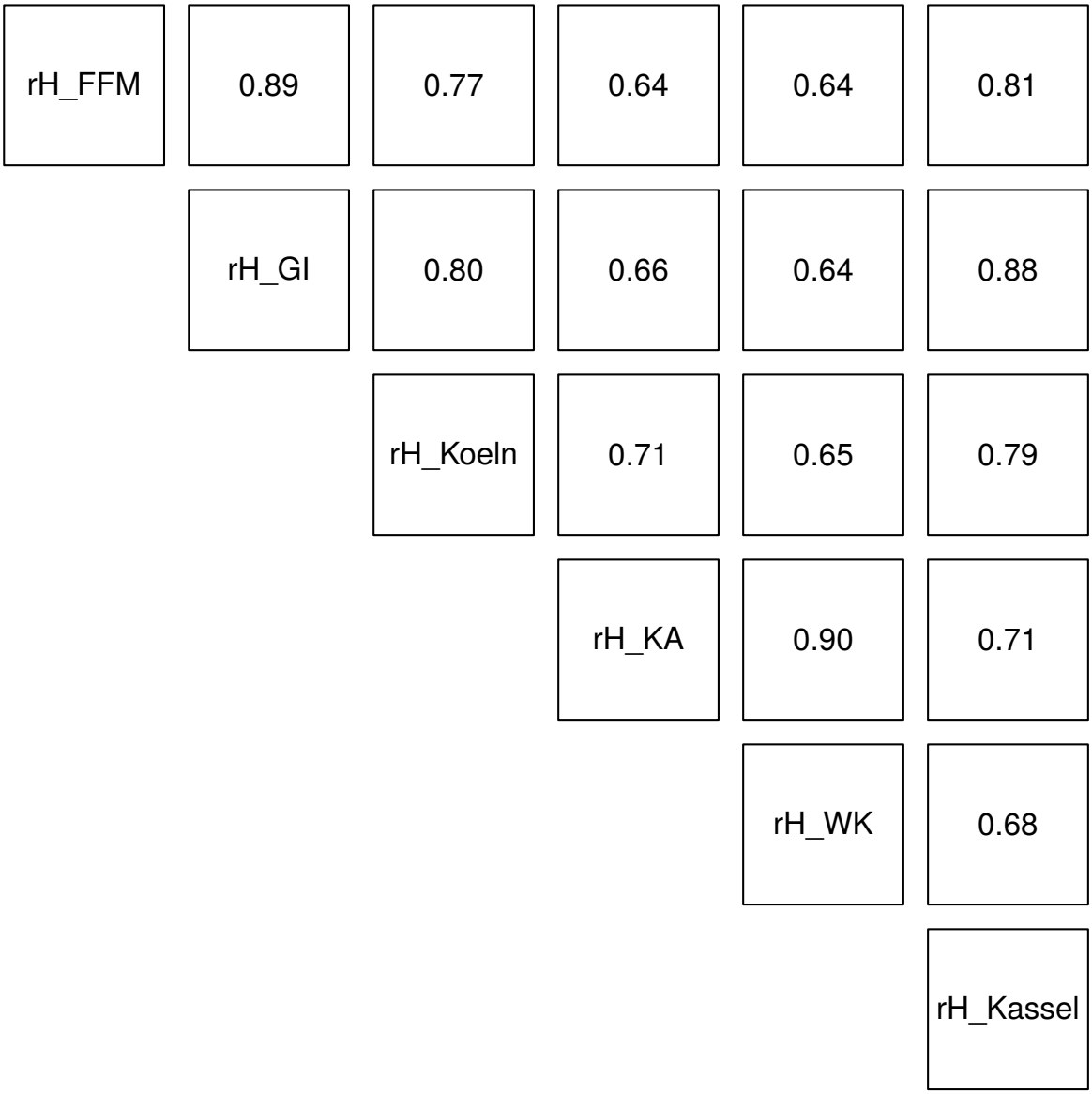

Figure A.4: Correlation matrix between daily relative humidity from the climate stations used in this study for the years 1949 - 2014. FFM: Frankfurt am Main; GI: Giessen; Koeln: Köln; KA: Kahler Asten; WK: Wasserkuppe/Rhön; Kassel: Kassel. All correlations are significant with $p < 0.01$

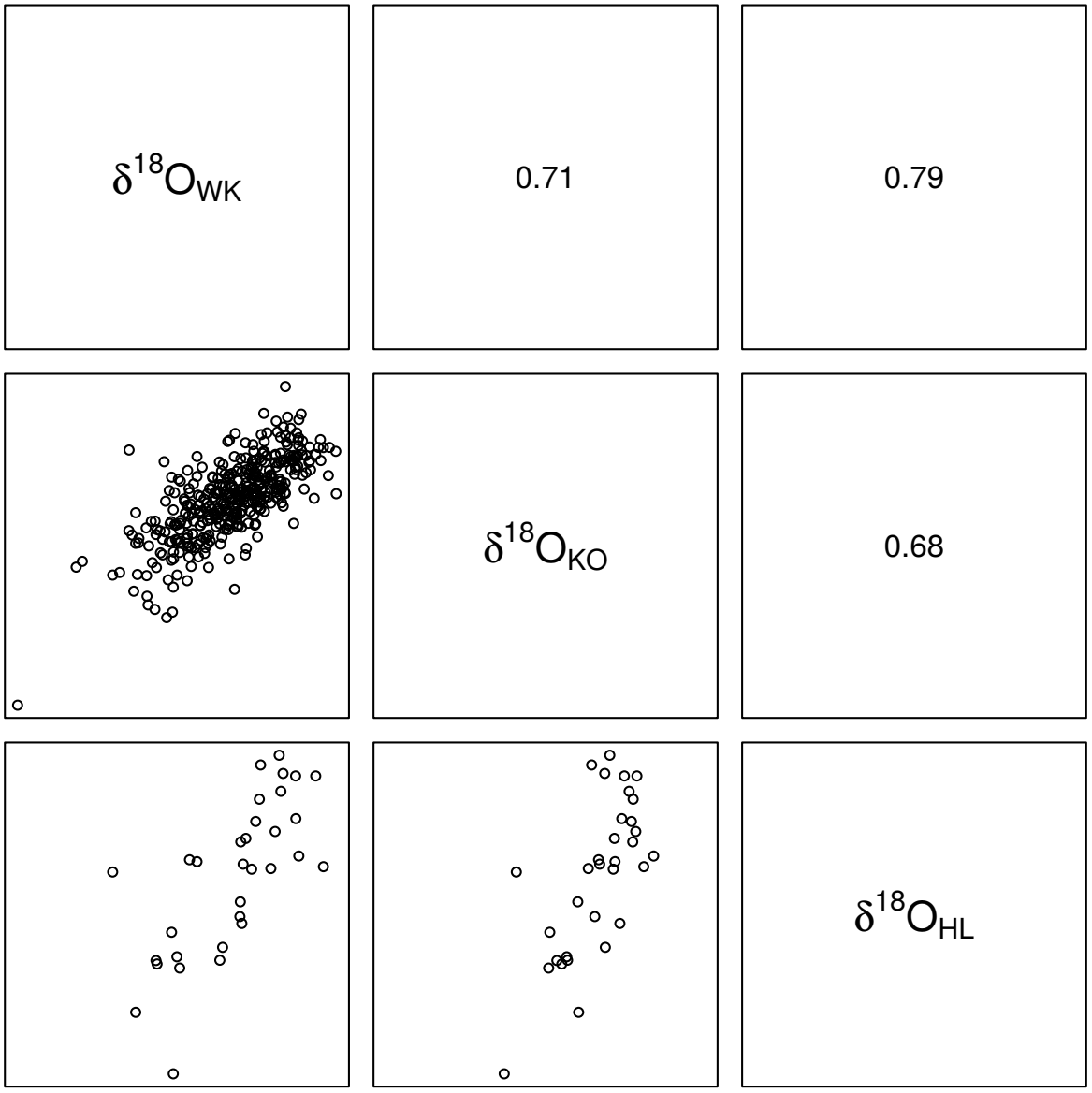

Figure A.5: Spearman's rank correlation coefficients of the δ^{18}O values of the GNIP climate stations Wasserkuppe/Rhön (WK), Koblenz (KO) and the Herbstlabyrinth-Adventhöhle HL cave system. All correlations are significant with $p < 0.01$

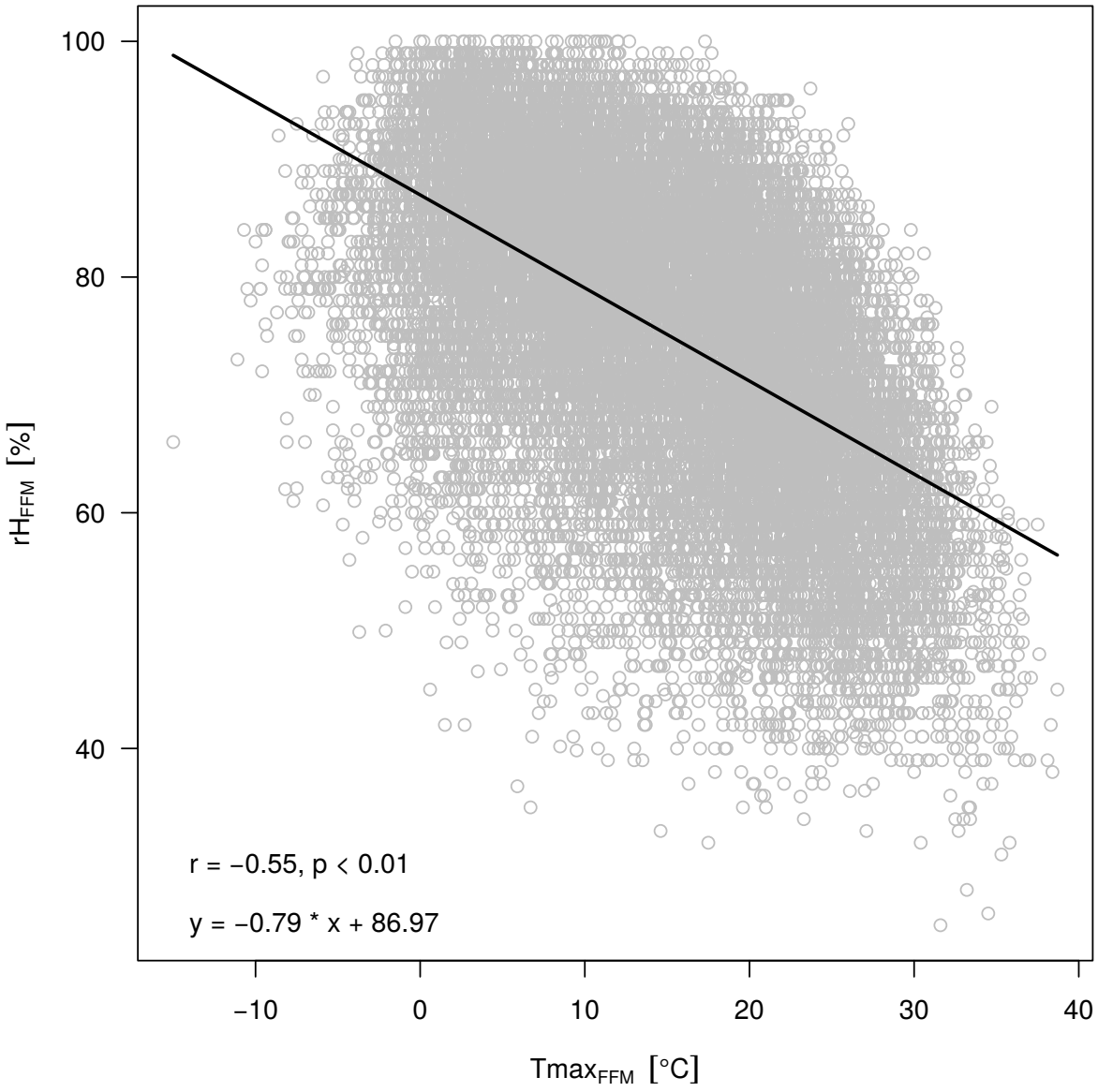

Figure A.6: Linear regression between daily relative humidity and maximum daily temperature for the climate station Frankfurt am Main for the years 1949 - 2014

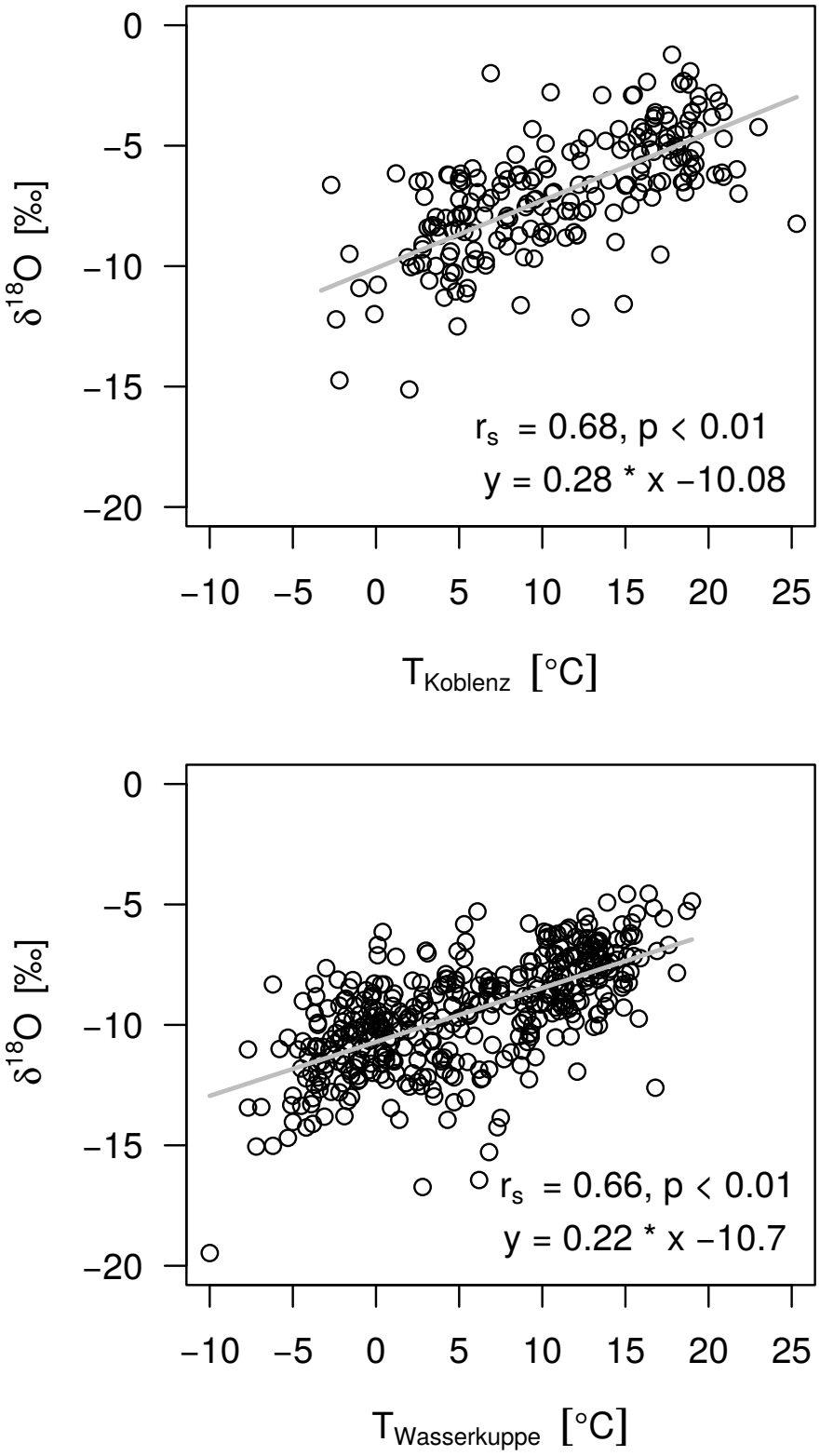

Figure A.7: Linear regression models between the $\delta^{18}O$ values of precipitation and temperature for the GNIP stations Koblenz and Wasserkuppe/Rhön

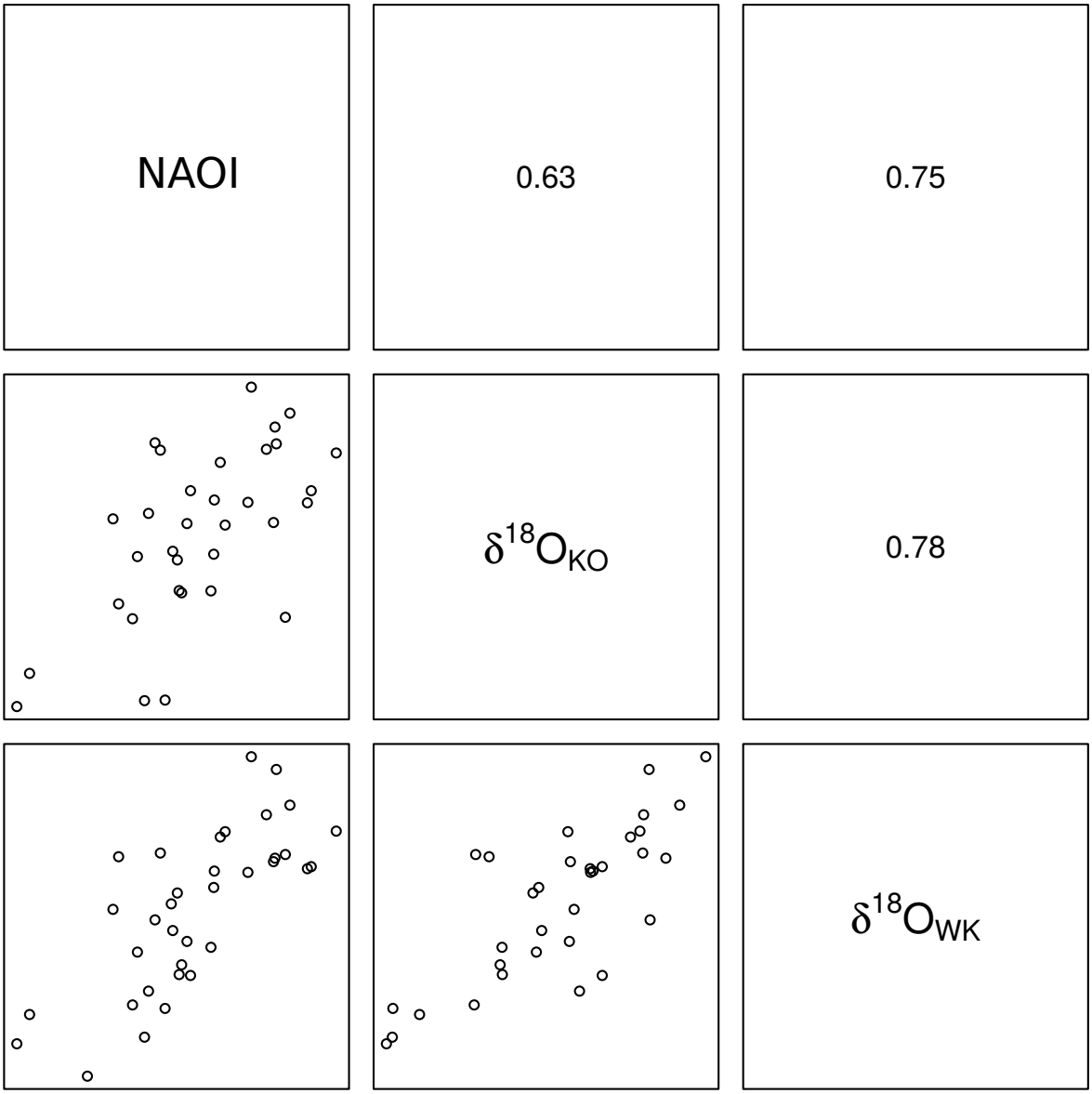

Figure A.8: Spearman's rank correlation matrix of the NAOI and the δ^{18}O values of the GNIP stations Koblenz and Wasserkuppe/Rhön for the winter season (DJFM). All correlations are significant with $p < 0.01$

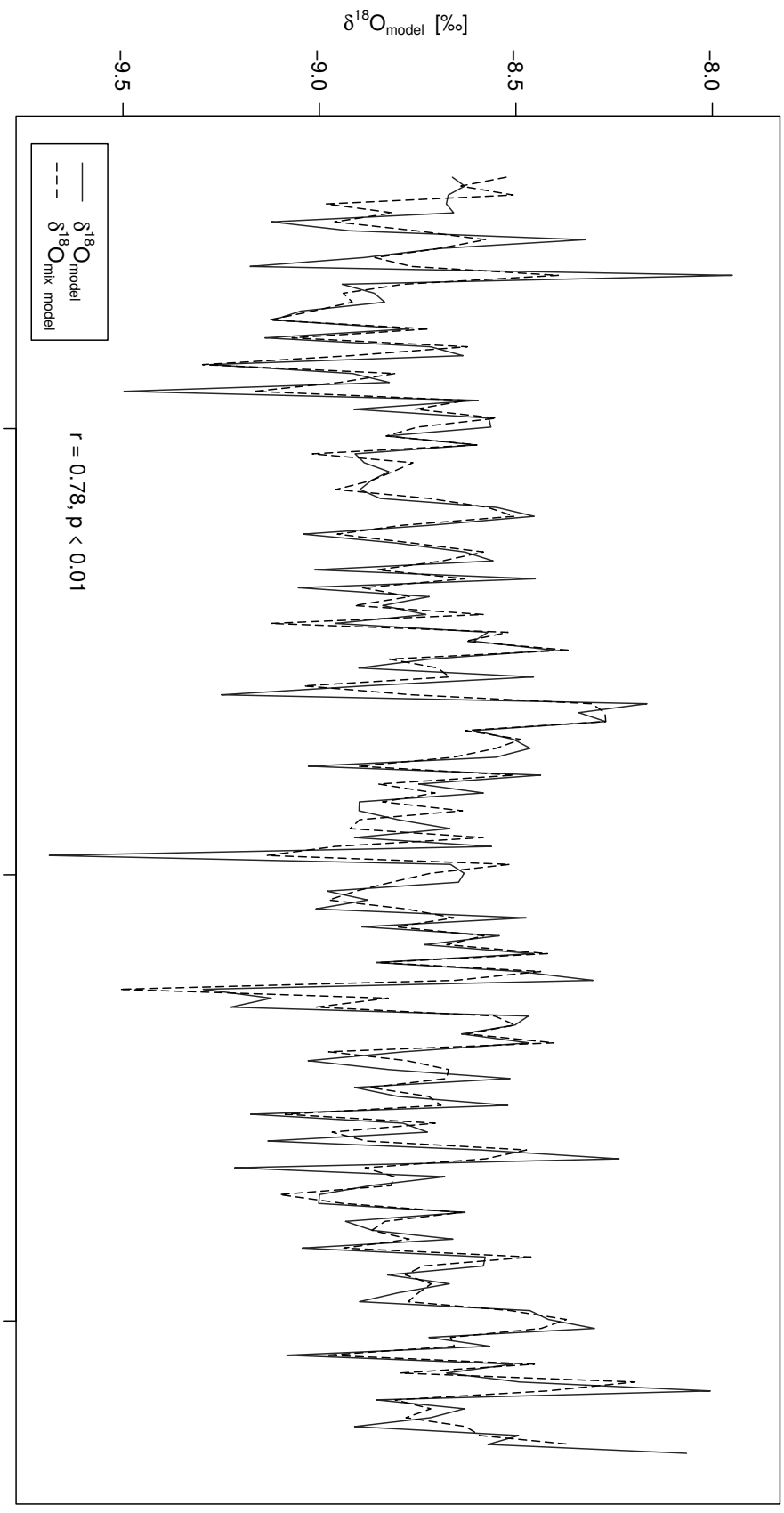

Figure A.9: Comparison of the modelled $\delta^{18}O$ values of the non-mixing (black line) and the mixing model (dashed line) assuming a mixing time of 12 months

B Electronical Supplement - Holocene climate variability

B.1 Appendix B

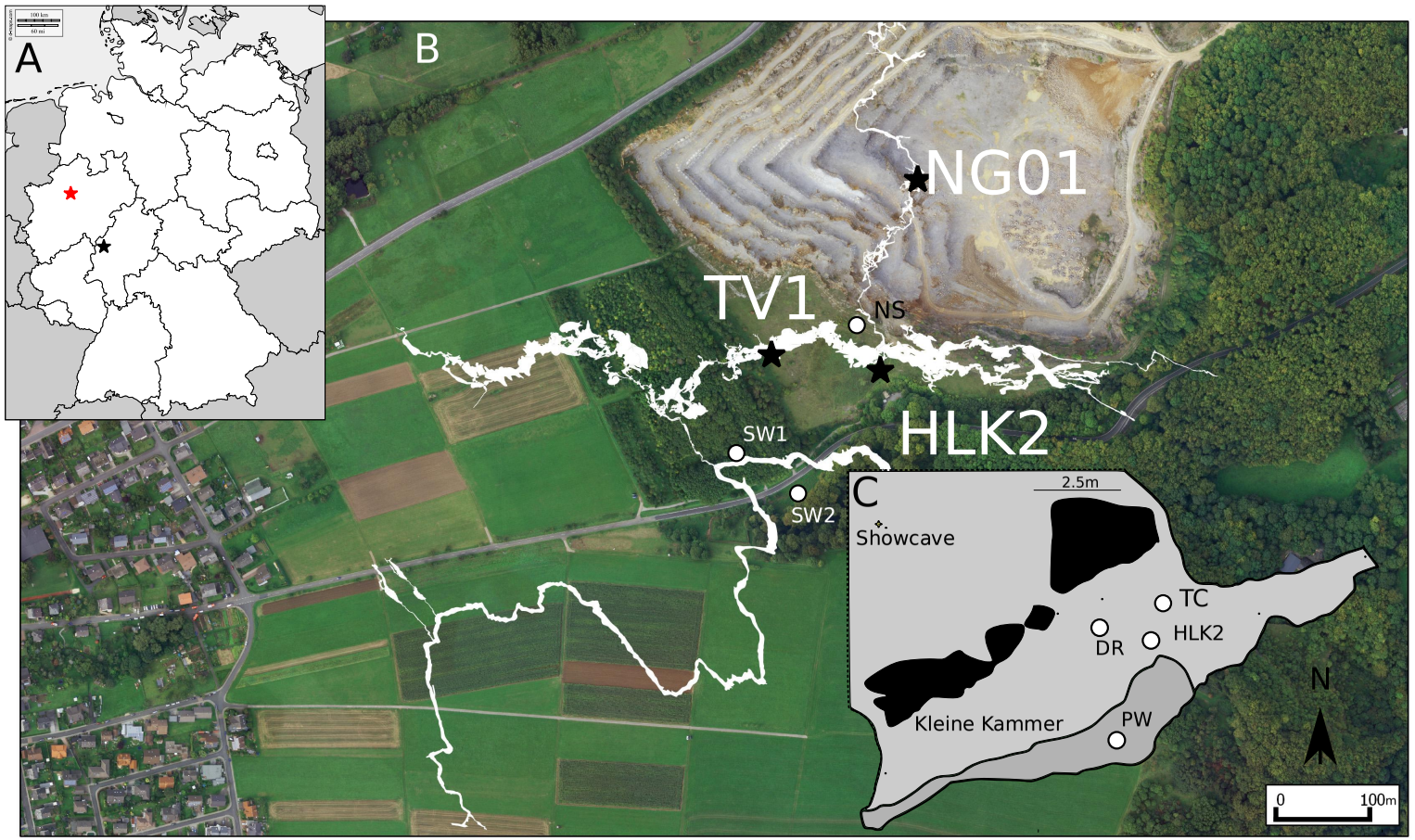

Figure B.1: A Map of Germany, the black asterisk marks the research area enlarged in (B). The red asterisk marks the location of Bunker Cave. B Arial photograph of the cave area. The cave is indicated in white. (NG01) Sampling location of stalagmite NG01. (HLK2) Sampling location of stalagmite HLK2. (TV1) Sampling location of stalagmite TV1. (NS) Location of the weather station. (SW1) Soil water (forest). (SW2) Soil water (meadow). C Enlarged map of the "Kleine Kammer". (TC) Location of the CORA logger. (DR) indicates the drip sites and (PW) the cave pool. HLK2 is the sampling location of stalagmite HLK2.

Figure B.2: The stalagmites “in situ”. A NG01 (white arrow). B HLK2, C TV1.

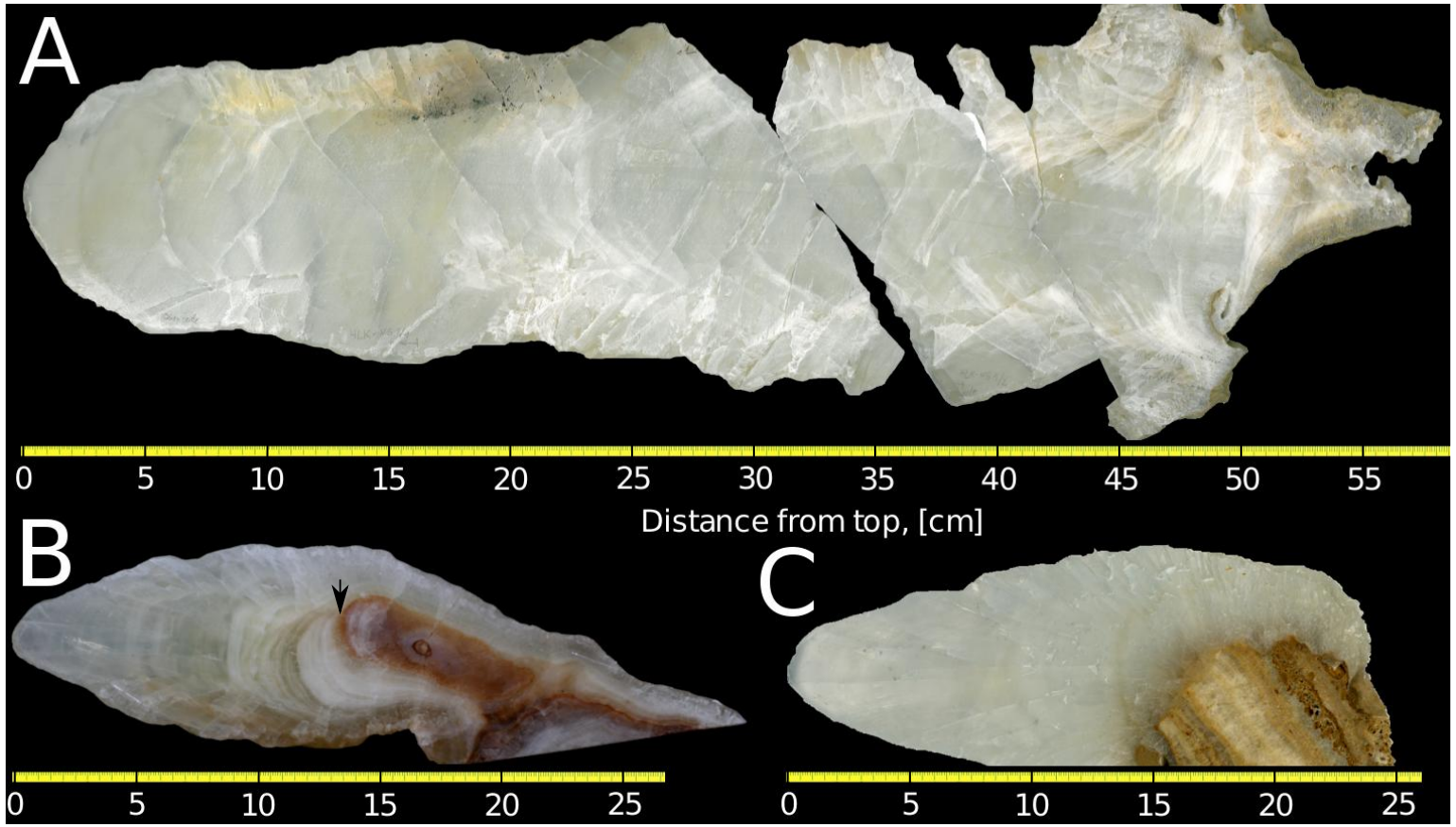

Figure B.3: Pictures of the slabs from the three stalagmites subsequent to cutting. A NG01. B HLK2, the black arrow marks the clay layer. C TV1.

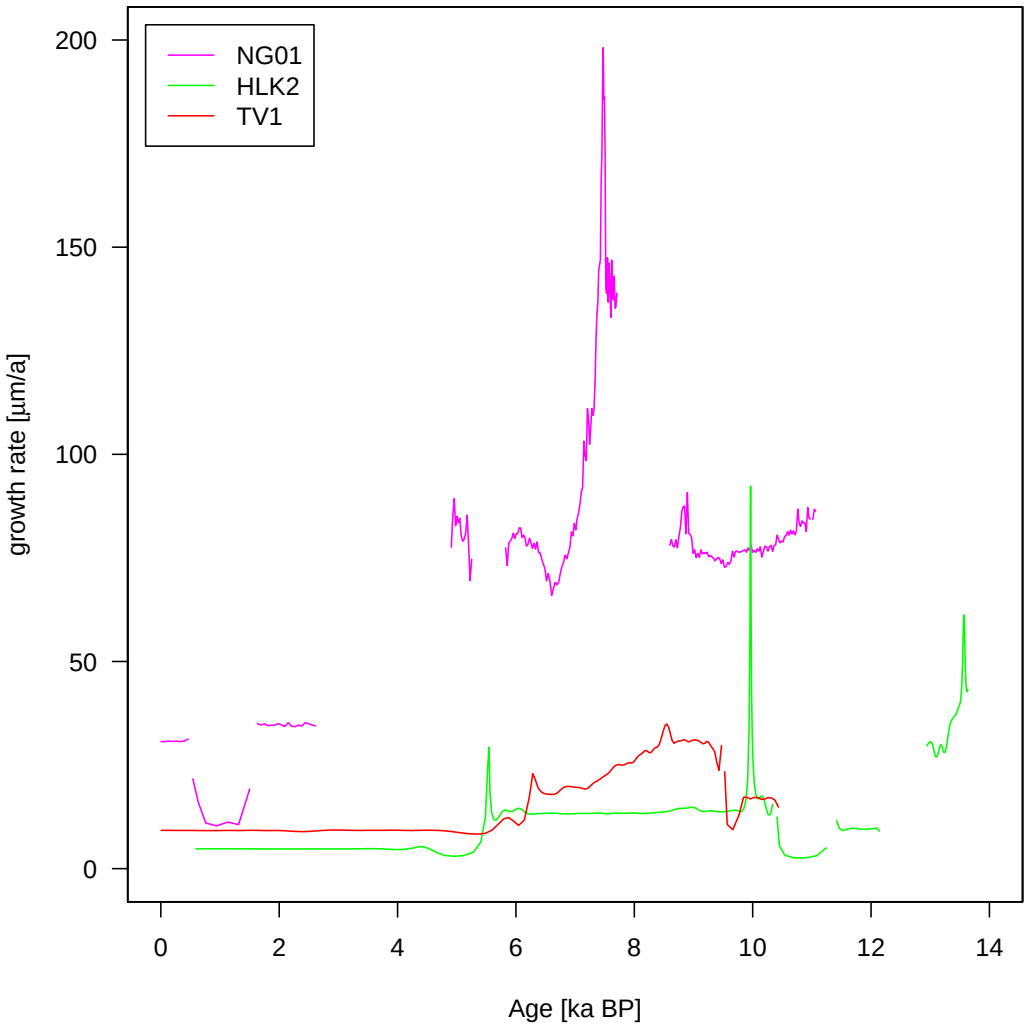

Figure B.4: The growth rate of the stalagmites calculated by StalAge. The short-term artificial spikes are introduced by the algorithm (Scholz et al. 2012).

Figure B.5: The correlation matrix for the individual growth phases of the stalagmites. The grey boxes mark significant correlations ($p<0.01$) and are inserted for improved readability.

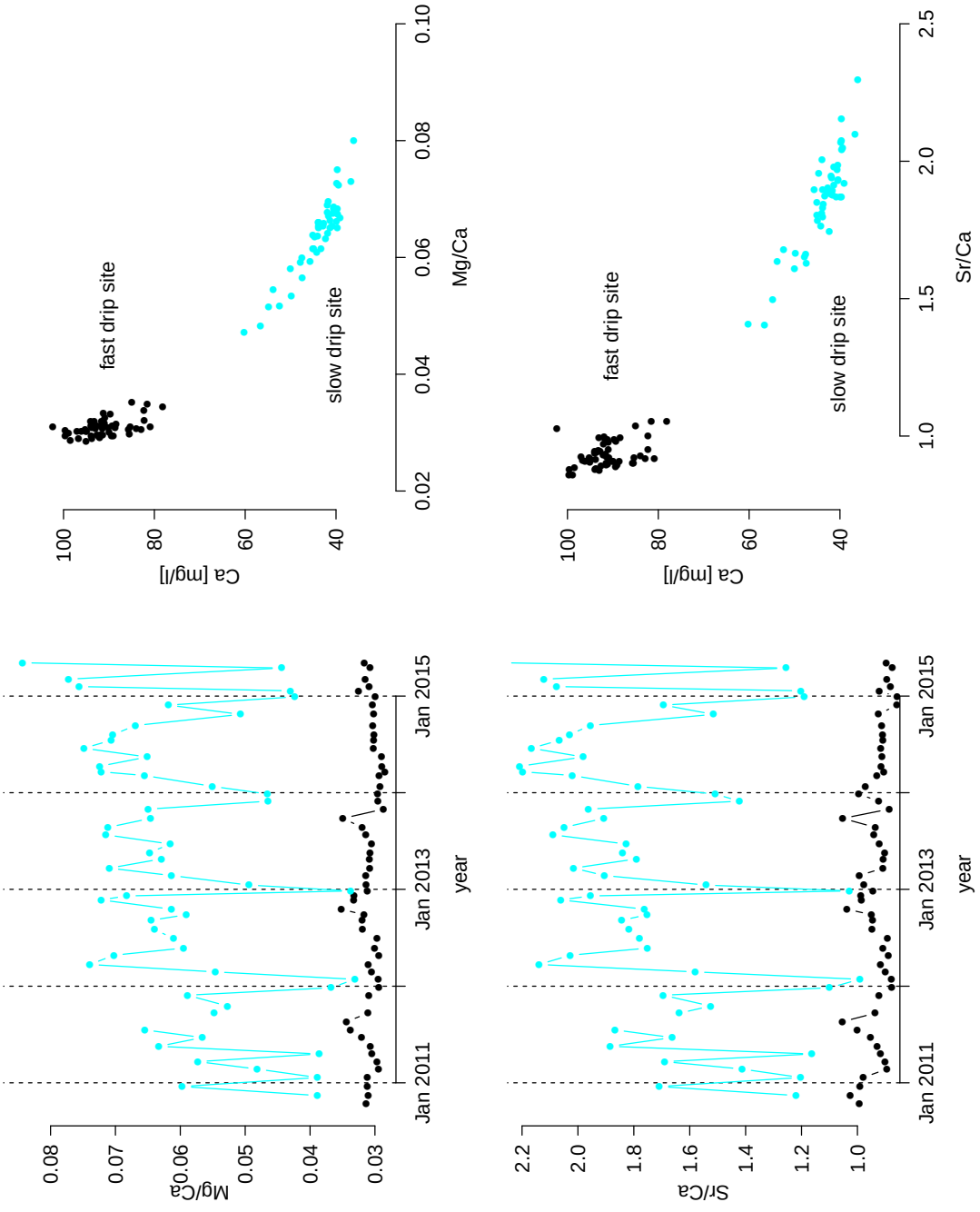

Figure B.6: The Mg/Ca and Sr/Ca ratios for the fast (black dots) and the slow drip site (cyan dots) potted against time and Ca concentration.

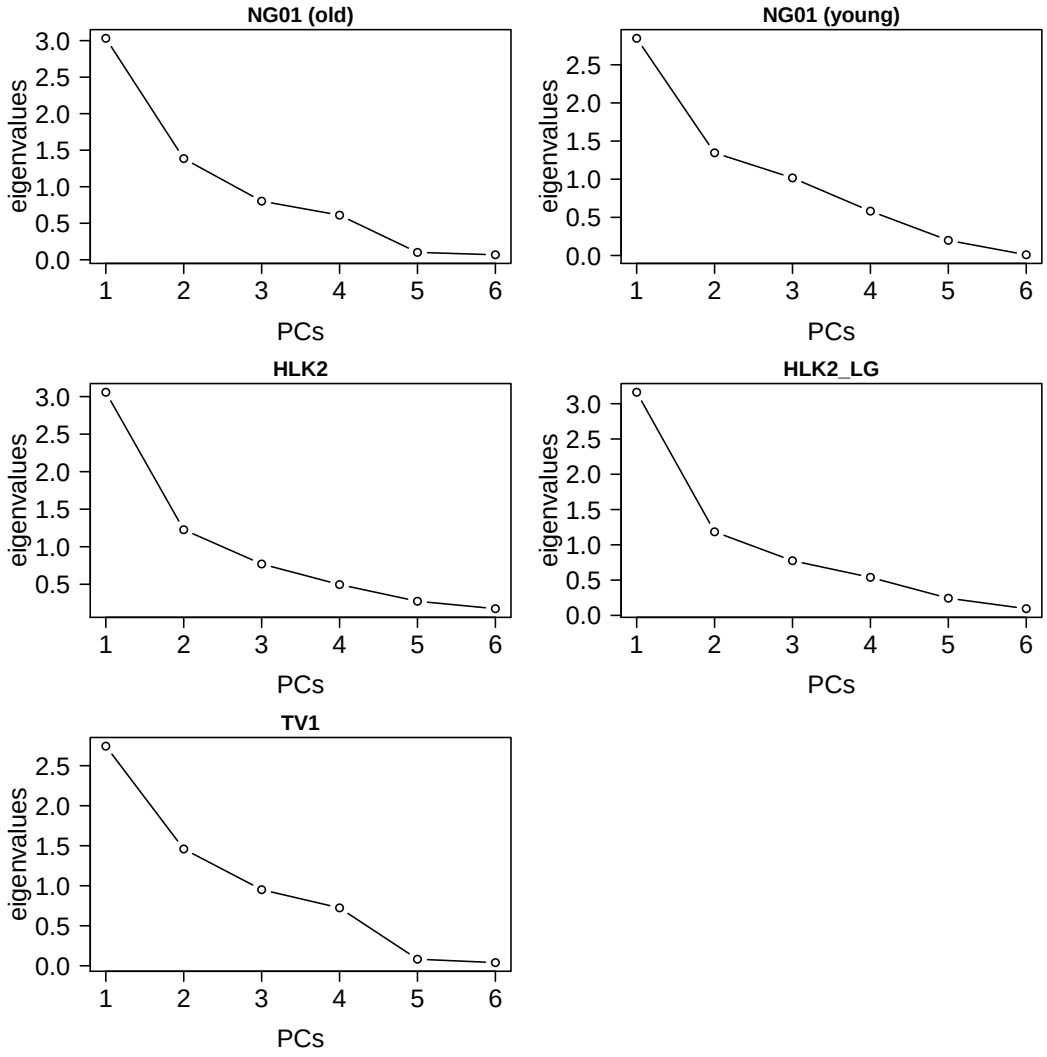

Figure B.7: Scree plot of the eigenvalues of the individual sections of the stalagmites.

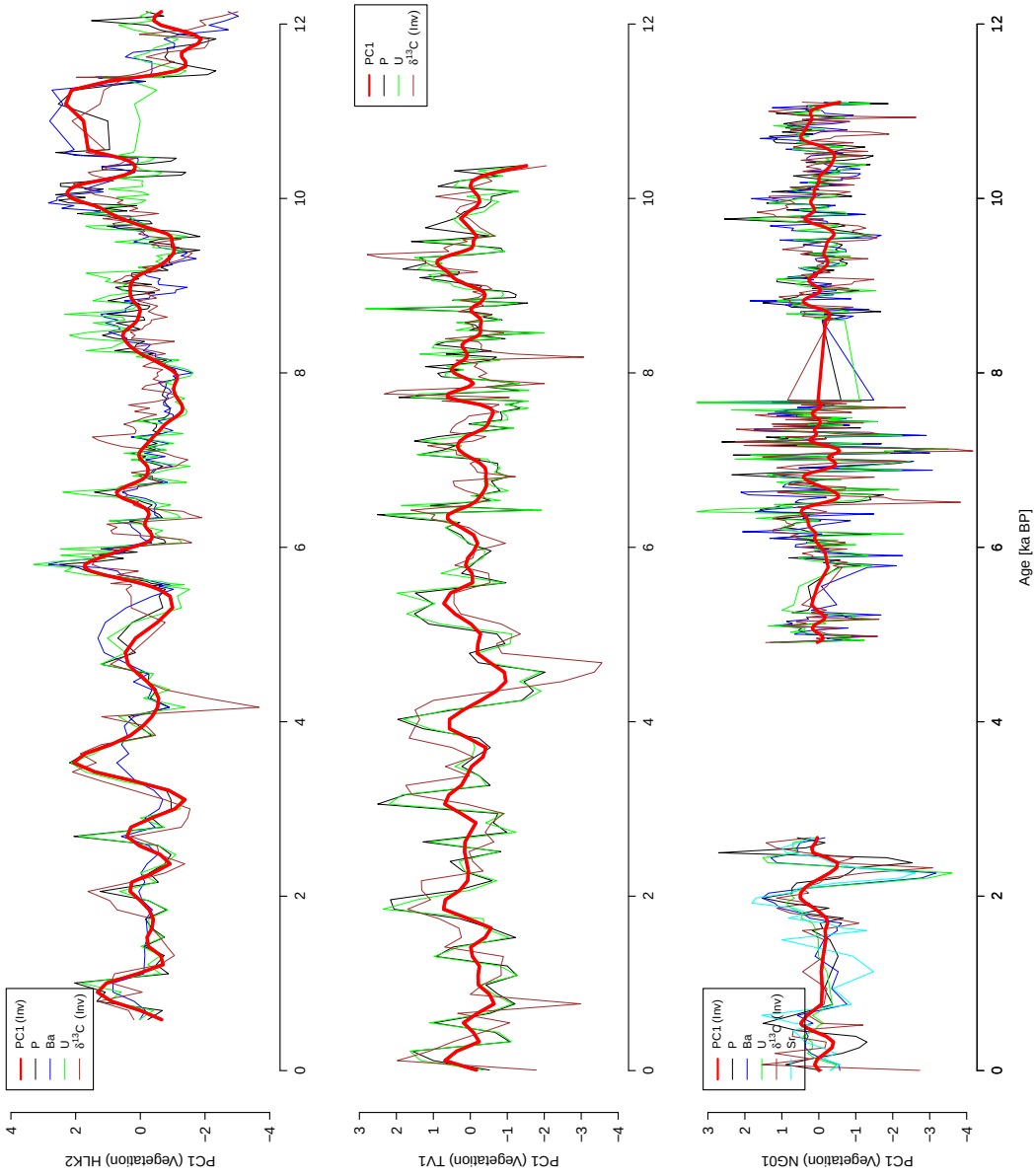

Figure B.8: Comparison of the first principal component (PC1) with the trace element and stable isotope records of the stalagmites.

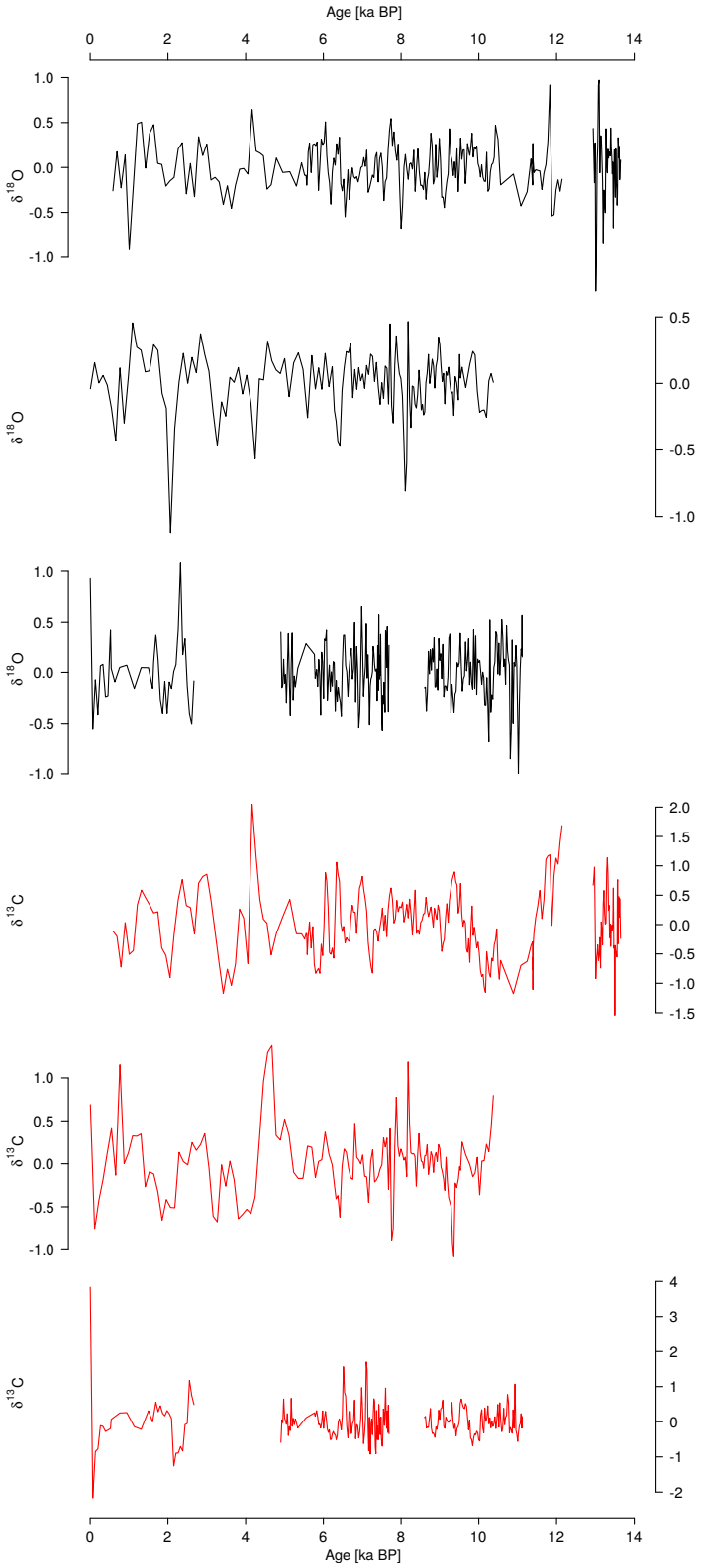

Figure B.9: Temporal evolution of the δ^{18}O and δ^{13}C values of stalagmites HLK2, TV1 and NG01. The black lines show the long-term trends of the data.

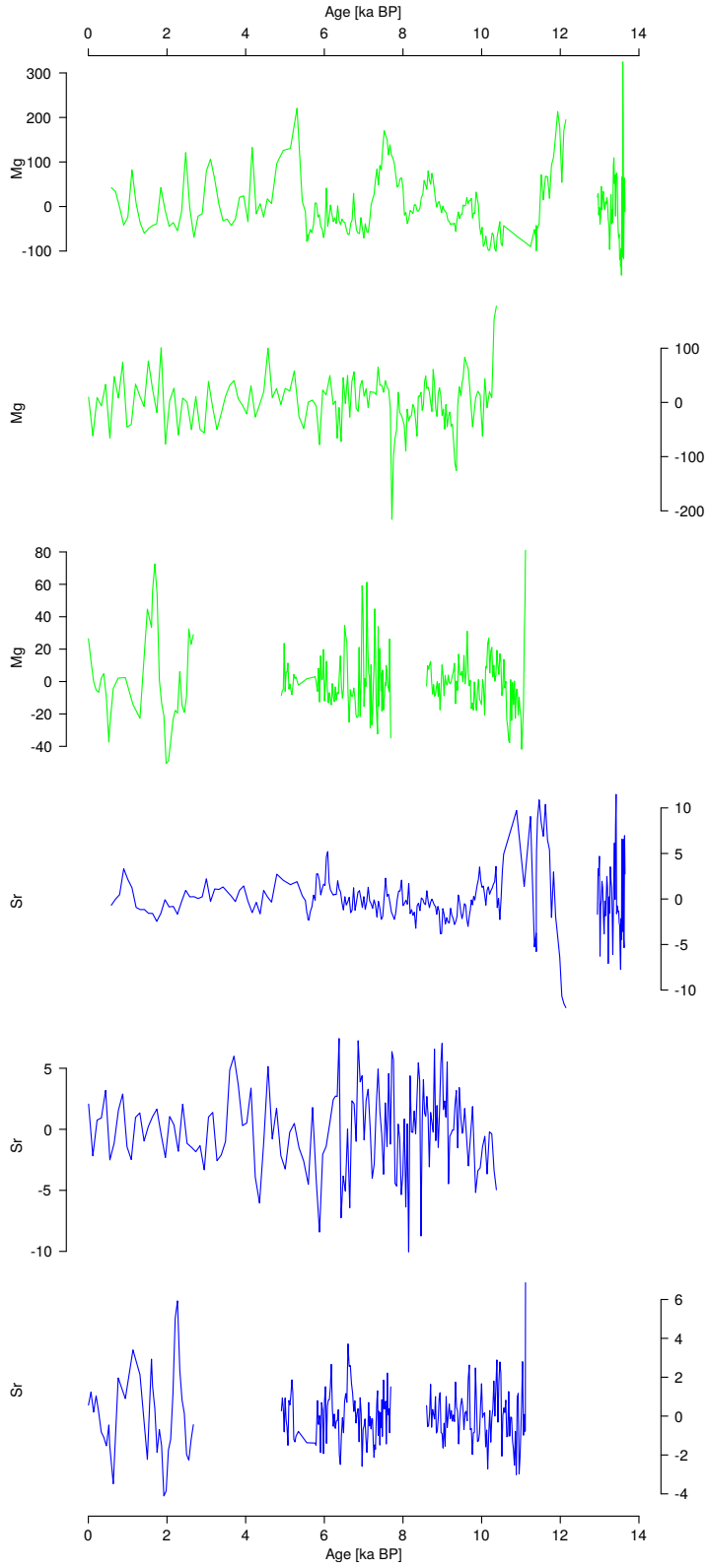

Figure B.10: Temporal evolution of the Mg and Sr concentrations of HLK2, TV1 and NG01. The black lines show the long-term trends of the data.

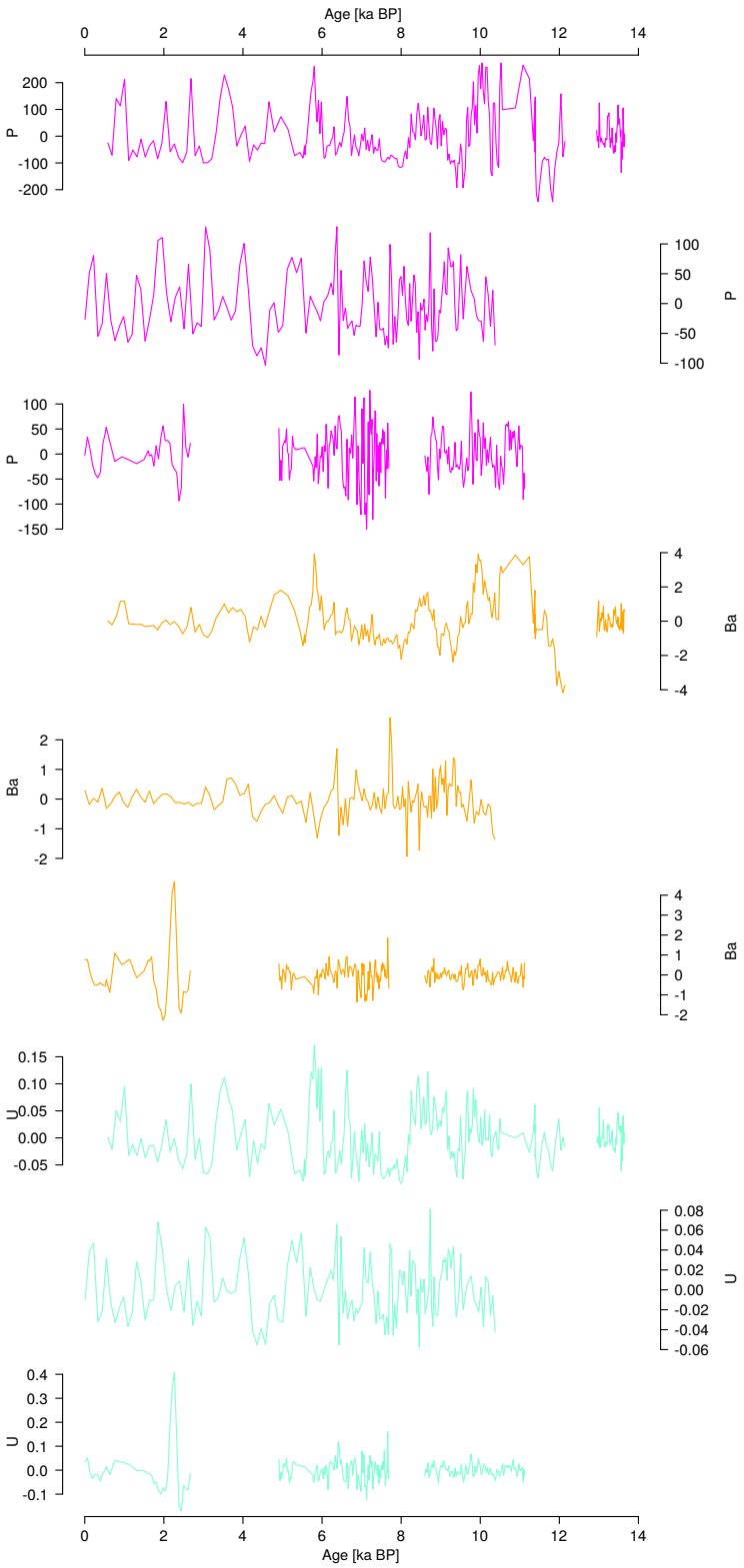

Figure B.11: Temporal evolution of the P, Ba and U concentrations of HLK2, TV1 and NG01. The black lines show the long-term trends of the data.

Table B.1: Results of ^{230}Th\U-dating of stalagmite NG01.

Sample name	Depth [mm]	^{238}U [µg g^{-1}]	2 σ error	^{232}Th [ng g^{-1}]	2 σ error	(^{234}U\$^{238}$U)	2 σ error
SM17	12	0.0822	0.0005	0.11	0.001	1.3176	0.0019
SM54	20.5	0.142	0.001	0.093	0.003	1.335	0.011
SM105	27.5	0.238	0.001	0.313	0.005	1.3603	0.0023
SM13	36	0.0953	0.0007	0.128	0.002	1.376	0.0041
SM106	46	0.305	0.002	0.364	0.004	1.3802	0.002
SM25	50	0.213	0.001	0.404	0.004	1.3812	0.0021
SM26	64	0.1507	0.0008	0.0482	0.0005	1.3707	0.0022
SM18	71.5	0.1178	0.0007	0.077	0.001	1.4581	0.0022
SM36	78	0.124	0.001	0.0366	0.0005	1.472	0.014
SM55	98.5	0.155	0.002	0.081	0.002	1.473	0.016
SM37	116	0.16	0.001	0.127	0.002	1.4897	0.0099
SM19	150	0.178	0.001	0.077	0.001	1.514	0.0027
SM38	191.5	0.186	0.002	0.0567	0.0008	1.544	0.016
SM56	229	0.181	0.002	0.0236	0.0005	1.548	0.018
SM39	237	0.144	0.002	0.02	0.0004	1.556	0.016
SM14	250	0.0944	0.0006	0.0264	0.0004	1.5456	0.0036
SM27	260	0.194	0.001	0.0633	0.0007	1.5488	0.0023
SM28	271.5	0.227	0.001	0.147	0.002	1.5501	0.0022
SM20	294	0.188	0.001	0.0208	0.0003	1.5858	0.0021
SM21	336	0.17	0.001	0.0338	0.0004	1.5974	0.0022
SM22	394	0.1508	0.0009	1.18	0.01	1.6101	0.0027
SM15	450	0.0598	0.0004	0.0199	0.0003	1.6211	0.004
SM23	480	0.1272	0.0008	0.136	0.002	1.6539	0.0022

SM29	498	0.1085	0.0006	0.266	0.003	1.6639	0.0027

Table B.2: Results of ^{230}Th\U-dating of stalagmite NG01, continued.

Sample name	Depth [mm]	(^{230}Th\$^{238}$U)	2 σ error	age uncorr. [ka]	2 σ error	age corr. [ka]	2 σ error
SM17	12	0.00685	0.00052	0.599	0.041	0.57	0.042
SM54	20.5	0.00849	0.0005	0.711	0.041	0.696	0.042
SM105	27.5	0.0173	0.00048	1.424	0.04	1.397	0.04
SM13	36	0.02018	0.00048	1.641	0.036	1.612	0.038
SM106	46	0.02533	0.0004	2.046	0.03	2.021	0.03
SM25	50	0.02689	0.00044	2.184	0.029	2.145	0.036
SM26	64	0.02735	0.00053	2.206	0.043	2.199	0.043
SM18	71.5	0.06496	0.00093	4.978	0.071	4.966	0.072
SM36	78	0.0666	0.0012	5.05	0.1	5.05	0.1
SM55	98.5	0.0699	0.0014	5.3	0.12	5.29	0.13
SM37	116	0.07965	0.00094	5.998	0.082	5.983	0.082
SM19	150	0.08544	0.00074	6.332	0.057	6.324	0.057
SM38	191.5	0.0962	0.0014	7	0.13	7	0.13
SM56	229	0.102	0.0019	7.42	0.17	7.42	0.17
SM39	237	0.1079	0.0017	7.82	0.15	7.81	0.15
SM14	250	0.103	0.0012	7.51	0.089	7.505	0.09
SM27	260	0.1039	0.0008	7.559	0.062	7.553	0.061
SM28	271.5	0.10532	0.00083	7.665	0.062	7.653	0.064
SM20	294	0.1234	0.0014	8.81	0.11	8.81	0.1
SM21	336	0.1291	0.001	9.158	0.078	9.155	0.078
SM22	394	0.1423	0.0015	10.184	0.09	10.05	0.11

SM15	450	0.1519	0.0014	10.68	0.1	10.68	0.1
SM23	480	0.1607	0.0011	11.11	0.08	11.092	0.083
SM29	498	0.1622	0.0012	11.171	0.087	11.13	0.088

Table B.3: Results of ^{230}Th\U-dating of stalagmite HLK2.

Sample name	Depth [mm]	^{238}U [µg g^{-1}]	2 σ error	^{232}Th [ng g^{-1}]	2 σ error	(^{234}U\$^{238}$U)	2 σ error
SM50	8	0.0619	0.0004	0.0223	0.0007	1.116	0.005
SM51	15.5	0.1355	0.0001	0.0141	0.0004	1.105	0.006
SM01	19	0.0648	0.0004	0.0088	0.0003	1.104	0.002
SM52	28.5	0.18	0.001	0.0129	0.0003	1.103	0.005
SM02	34	0.0589	0.0004	0.0028	0.0001	1.103	0.002
SM09	50.2	0.0321	0.0002	0.0031	0.0001	1.109	0.002
SM03	62.5	0.1382	0.0009	0.0051	0.0001	1.152	0.002
SM04	77	0.0888	0.0006	0.0151	0.0003	1.182	0.002
SM05	95	0.0949	0.0006	0.0143	0.0003	1.223	0.002
SM33	100	0.1428	0.0009	0.0305	0.0006	1.287	0.004
SM34	102	0.132	0.001	0.3402	0.003	1.295	0.008
SM53	104	0.114	0.001	0.2418	0.003	1.283	0.01
SM06	108	0.078	0.0005	0.0637	0.0008	1.281	0.002
SM35	113	0.0651	0.0006	0.237	0.003	1.305	0.01
SM30	120	0.0597	0.0003	0.0604	0.0007	1.308	0.002
SM10	121	0.0287	0.0002	0.242	0.003	1.327	0.003
SM11	128	0.0516	0.0004	0.094	0.001	1.311	0.004
SM31	132	0.1115	0.0006	0.202	0.002	1.317	0.002

SM12	137	0.019	0.0001	0.694	0.0079	1.3024	0.0053

Table B.4: Results of ^{230}Th\U-dating of stalagmite HLK2, continued.

Sample name	Depth [mm]	(^{230}Th\$^{238}$U)	2 σ error	age uncorr. [ka]	2 σ error	age corr. [ka]	2 σ error
SM50	8	0.023	0.002	2.249	0.189	2.24	0.19
SM51	15.5	0.0377	0.0008	3.793	0.091	3.791	0.092
SM01	19	0.045	0.0008	4.546	0.08	4.542	0.08
SM52	28.5	0.0588	0.001	5.976	0.145	5.974	0.146
SM02	34	0.0617	0.001	6.282	0.1	6.281	0.102
SM09	50.2	0.074	0.001	7.534	0.131	7.532	0.131
SM03	62.5	0.087	0.003	8.544	0.267	8.543	0.265
SM04	77	0.098	0.001	9.43	0.133	9.426	0.135
SM05	95	0.112	0.001	10.438	0.107	10.435	0.105
SM33	100	0.13	0.002	11.611	0.191	11.606	0.187
SM34	102	0.129	0.001	11.447	0.133	11.39	0.13
SM53	104	0.129	0.003	11.616	0.269	11.569	0.275
SM06	108	0.134	0.001	12.017	0.131	11.999	0.134
SM35	113	0.148	0.002	13.146	0.25	13.067	0.249
SM30	120	0.15	0.002	13.278	0.167	13.256	0.171
SM10	121	0.155	0.002	13.654	0.173	13.473	0.201
SM11	128	0.153	0.002	13.61	0.161	13.571	0.163
SM31	132	0.155	0.001	13.659	0.132	13.62	0.132
SM12	137	0.5499	0.0052	59.2	0.72	58.47	0.79

Table B.5: Results of ^{230}Th\U-dating of stalagmite TV1. bdl = below detection limit

Sample name	Depth [mm]	^{238}U [µg g^{-1}]	2 σ error	^{232}Th [ng g^{-1}]	2 σ error	(^{234}U\$^{238}$U)	2 σ error
SM90	16.5	0.0993	0.0005	0.0084	0.0004	1.892	0.003
SM100	29.5	0.0962	0.0005	bdl	bdl	1.89	0.003
SM91	42	0.0965	0.0005	0.0119	0.0004	1.925	0.003
SM101	53	0.1233	0.0007	bdl	bdl	1.907	0.003
SM102	62	0.1621	0.0009	bdl	bdl	1.845	0.003
SM92	71.5	0.0906	0.0005	0.003	0.0003	1.819	0.002
SM103	82	0.1361	0.0007	bdl	bdl	1.861	0.003
SM104	93	0.1386	0.0008	0.1049	0.002	1.673	0.003
SM93	105	0.1451	0.0008	0.0066	0.0003	1.856	0.003
SM94	135.5	0.2152	0.001	0.078	0.001	1.711	0.002
SM95	140.5	0.2026	0.001	0.208	0.003	1.849	0.003
SM96	150.5	0.18	0.001	0.534	0.005	1.898	0.003

Table B.6: Results of ^{230}Th\U-dating of stalagmite Tv1, continued.

Sample name	Depth [mm]	(^{230}Th\$^{238}$U)	2 σ error	age uncorr. [ka]	2 σ error	age corr. [ka]	2 σ error
SM90	16.5	0.0305	0.0009	1.776	0.05	1.775	0.05
SM100	29.5	0.057	0.001	3.327	0.06	3.327	0.06
SM91	42	0.079	0.001	4.577	0.08	4.575	0.08
SM101	53	0.0997	0.001	5.843	0.08	5.843	0.08
SM102	62	0.107	0.001	6.497	0.07	6.497	0.07
SM92	71.5	0.114	0.002	7.016	0.09	7.015	0.1

SM103	82	0.124	0.002	7.519	0.1	7.519	0.1
SM104	93	0.119	0.002	8.022	0.12	8.009	0.12
SM93	105	0.139	0.002	8.426	0.1	8.426	0.1
SM94	135.5	0.142	0.002	9.427	0.11	9.421	0.11
SM95	140.5	0.156	0.002	9.55	0.11	9.534	0.11
SM96	150.5	0.171	0.001	10.308	0.07	10.264	0.08

Table B.7: The trace element concentrations and stable isotope ratios from the two host rock samples AG1 and AG2 and the corresponding mean value.

Element	AG1	AG2	mean	Element	AG1	AG2	mean
Magnesium	2962	2567	2764.5	Yttrium	1.36	4.81	3.085
Aluminium	272	616	444	Lanthanum	0.72	2.90	1.81
Silicon	609	1105	857	Cerium	0.84	1.78	1.31
Phosphorous	13	23	18	Praseodymium	0.14	0.55	0.345
Sulphur	3.3	2.7	3	Neodymium	0.61	2.51	1.56
Calcium	400000	400000	400000	Promethium	NA	NA	NA
Iron	268	299	283.5	Samarium	0.14	0.53	0.335
Zinc	0.89	1.2	1.045	Europium	0.04	0.14	0.09
Rubidium	0.52	1.28	0.9	Gadolinium	0.16	0.68	0.42
Strontium	182	185	183.5	Terbium	0.02	0.08	0.05
Zircon	0.43	0.84	0.635	Dysprosium	0.14	0.57	0.355
Niobium	0.03	NA	0.03	Holmium	0.03	0.12	0.075
Cesium	0.04	NA	0.04	Erbium	0.09	0.32	0.205
Barium	3.1	5.7	4.4	Thulium	0.02	0.05	0.035
Lead	0.43	0.56	0.495	Ytterbium	0.07	0.22	0.145
Thorium	0.06	0.09	0.075	Lutetium	0.01	0.03	0.02
Uranium	0.14	0.14	0.14				
Isotope	AG1	AG2	mean				
δ^{13}C	1.6	2.9	2.25				
δ^{18}O	-4.8	-5.2	-5				

Table B.8: The trace element concentrations and stable isotope ratios from the two host rock samples AG1 and AG2 and the corresponding mean value.

	NG01_young		NG01_old		HLK2		HLK2_LG		TV1	
	PC1	PC2	PC1	PC2	PC1	PC2	PC1	PC2	PC1	PC2
Mg	<0.30	0.87	-0.67	-0.4	-0.6	<0.30	0.69	-0.37	-0.48	<0.30
Sr	0.91	<0.30	<0.30	0.96	0.33	-0.87	0.82	0.38	0.48	0.85
P	-0.33	-0.45	0.91	<0.30	0.86	0.34	-0.92	<0.30	0.82	-0.39
Ba	0.95	<0.30	0.82	<0.30	0.87	<0.30	0.58	0.7	0.76	0.59
U	0.9	<0.30	0.85	-0.4	0.71	0.52	-0.83	<0.30	0.87	<0.30
δ^{13}C	-0.42	0.6	-0.58	<0.30	-0.76	<0.30	0.38	-0.61	-0.52	<0.30
Variance	0.47	0.22	0.51	0.23	0.51	0.2	0.53	0.2	0.46	0.24
Cumulative Var.	0.47	0.7	0.51	0.74	0.51	0.71	0.53	0.72	0.46	0.70
Eigenvalues	2.85	1.35	3.03	1.39	3.06	1.23	3.16	1.18	2.74	1.46

C Electronical Supplement - TERMITE

C.1 Appendix C

This guide provides a step by step walk-through for TERMITE (Mischel et al. (submitted)): TERMITE - an R script for fast reduction of LA-ICPMS data and its application to trace element measurements). The reader should carefully work through this manual prior to the usage of TERMITE.

C.1.1 General marks

- A section for troubleshooting is provided at the end of this guide.
- Lines starting with # as well as everything in a line following # are commentaries.
- Variables consisting of text (e.g., "your_sample_name") **must** be provided with quotation marks.
- TERMITE will never change your raw data files. All files will just be read into R's internal memory, and the calculations will be performed within R.
- The files of the reference materials need to have an assigned, unique name in order for the script to work properly. The name must contain the definite text string provided in the reference material section of the script (Supplement Figure C.5, name in brackets ("NIST612", "GSD", "MACS3", "KL2-G", "BAM-B", "T1-G", "MACS1", "StHs", "ATHO-G" and "NIST610", also possible is "N610" and N612")). When only a single reference material is used, the line RefMat1 must be filled in, and all other lines must start with #. If two lines without # are indicated, those two reference materials will be used for calibration (see exemplarily Supplement Figure C.5). The reference materials must be in chronological order (e.g. Reference Material 1, Reference Material 2), no matter how many reference materials have been analysed during the analytical session. TERMITE calculates one RSF_{mean} from the RSF values for each of the selected reference materials. It is important to note that even if the files of two reference materials are copied into the ReferenceMaterial_directory, only the files, which are indicated in the reference material section of the script, are used. Experiments consisting of more than 10 spot measurements need one leading zero in the filename (e.g., Spot_01.asc,

Spot_02.asc). If the experiment consists of more than 100 spots, the user needs to rename the data files using two leading zeroes (e.g., Spot_001, Spot_002). This practice is mandatory to guarantee correct sorting of the spots on the sample. The output of the script is written into the Results_directory:

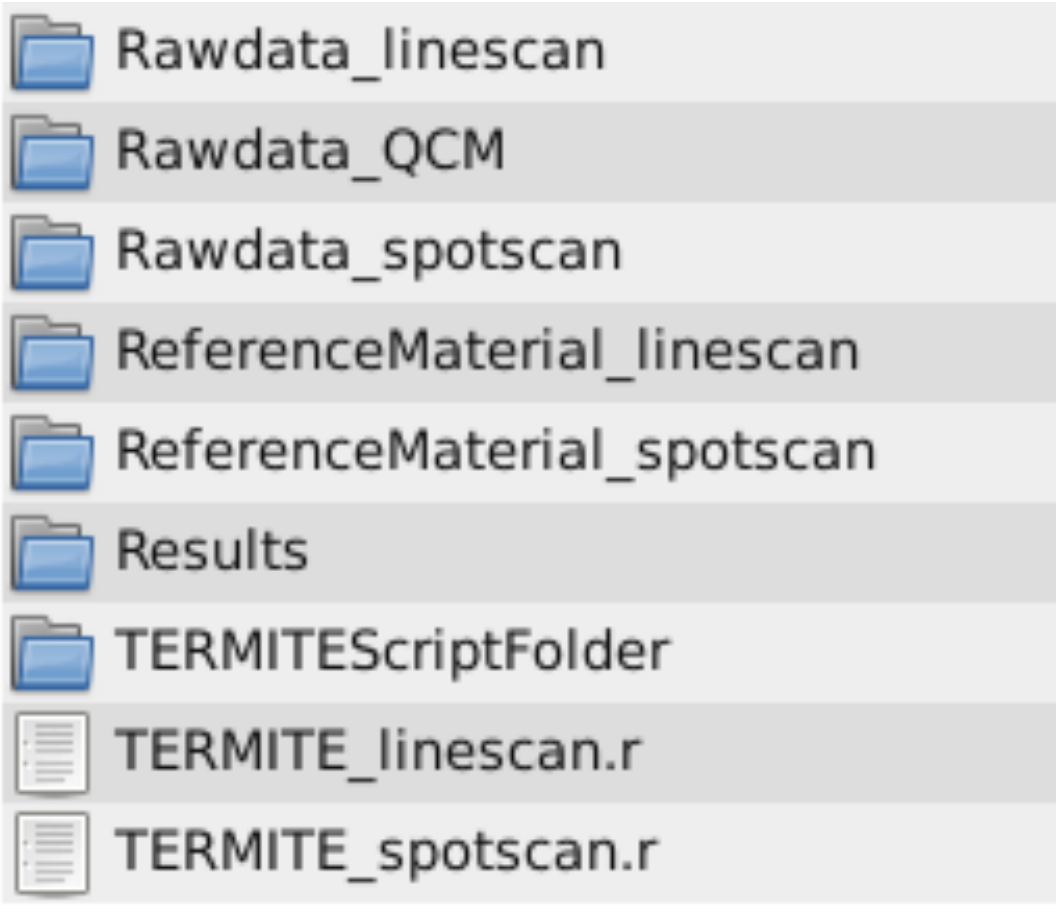

Figure C.1: Structure of the directories, which must be created by the user if not existing.

  - A pdf file with the raw count rates is plotted together with vertical lines indicating the sections used for the background determination and the sample signal as defined in the HelpValue sections of the script (rawCountrate_your_sample_name.pdf)
  - The results are saved as a csv and a pdf file.
  - The Limit of detection (LoD) is saved as a csv and a pdf file.
  - The RSF values are saved as a csv and a pdf file.

- If the user needs to update the Reference Material values provided together with the script, the file is found in the directory "TERMITEScriptFolder" and is named "Standards_GeoReM.csv". This file can be opened and edited with Excel, OpenOffice or any

other text editor. The values must be separated by commas, and white space is filled with NA for consistency.

C.1.2 Initial preparations

1. Download and install R (*https* : *//cran.r* − *project.org*). If problems arise during the installation, please use the documentation provided on this site.

2. Unzip the file your_main_directory.zip. This file contains the script TERMITE and all mandatory files for the script. It also contains an example of a line scan and 5 spot measurements.

3. For spot analyses, the file TERMITE_spotscan.r is used. For line scan analyses, the file TERMITE_linescan.r is used. Technically, these files are identical, but the example includes both types of experiments.

4. Navigate into your main directory.

5. Prepare, if not existing, additional folders in the main directory as shown in Figure C.1). The user can decide which names should be assigned to the directories.

6. Copy the raw data sample files of the laser ablation measurements into the corresponding directory (Rawdata_linescan or Rawdata_spotscan). If a line scan is evaluated, the Rawdata_linescan directory should only contain 1 file. It is important that one dataset must have the same internal standard concentration (e.g., for a stalagmite, Calcium: $\sim$400 000 µg g^{-1}). If, for example, a quality control material (QCM), such as MACS-3, is treated as an unknown sample, the concentration of the internal standard is different (MACS-3, Calcium: $\sim$376 900 µg g^{-1}). Therefore, the raw data files of MACS-3 have to be stored in separate folders (e.g., Rawdata_QCM).

7. Experiments consisting of more than ten samples need one leading zero in the filename (e.g., Spot_01.asc, Spot_02.asc). If the experiment consists of more than 100 samples, the two leading zeroes are required (e.g., Spot_001, Spot_002). This is required to guarantee correct sorting of the samples.

8. Copy the Reference Material data files used for calibration into the folder ReferenceMaterial_directory.

9. Open the file "TERMITE_script_linescan.r" or "TERMITE_script_spotscan.r" depending on the type of your experiment (spot or line scan analysis) and work through the script prior to data evaluation. The steps are explained in the following (Supplemental Figure 4.3, 4.5, 4.6).

10. The packages “miscTools” (Henningsen and Toomet 2013) and “matrixStats” (Bengtsson 2015) will be installed automatically if the corresponding lines are run (the three lines after the section “installs all required packages”, Supplemental Figure C.2). In case of any problems, try to choose a different download mirror or try using “http” instead of “https”. In case of errors, these packages can be installed manually by executing the commands install.packages(“matrixStats”) and install.packages(“miscTools”).

11. As a first step, the names of the folders must be passed into the script in the directory part (if not already there, Supplemental Figure C.2). It is important that the names are identical to the names assigned in step 5. Please note that R is case sensitive and distinguishes between lower and upper case letters. In addition, all directories must be provided using slash (/) instead of backslash (\).

12. The slash (/) in Figure 2 at the end in the object path is mandatory.

13. The name of the sample (sample.name, e.g. “your_sample_name”) should be assigned. This helps the user to identify the sample after data reduction because this text string is printed in all file names.

14. Prior to data reduction, the user should work through the section “HelpValues” and provide all important parameters for data reduction in the script (Supplement Figure C.3).

15. In the following, the HelpValue section is explained step by step:

    - Mode.of.Scan: insert “spot.scan” or “line.scan” depending on your experimental setup.
    - Line.of.Header is the line in the original raw data file, where the names of the isotopes are found in the data files (Supplement Figure C.4).
    - Line.of.Signal is the line, where the signal of the ablation run starts, normally starting with the background signal (Supplement Figure C.4).
    - Measured.isotopes is the number of all measured isotopes including the Internal Standard (IS).
    - Column.IS is the number of the column in the raw data file where the internal standard isotope (IS) is located (Supplement Figure C.4).
    - IS is the concentration of the internal standard in the sample and the reference material (e.g., Ca $\sim$400 000 µg g^{-1}).
    - The outlier test (for spot scan measurements and for reference materials) can be switched on and off. Please note that in case of a line scan, the outlier test will only be evaluated during the calculation of the reference materials.
    - m is the percentage of the range for the outlier test.

- number.sweeps.sample is the number of total sweeps recorded in the raw data file of the sample (Supplement Figure C.4).
- number.sweeps.Refs is the number of total sweeps recorded in the raw data file of the reference material. Typically, spot scans are measured with the same experimental setup (e.g., background and ablation time, etc.) as the reference materials. In this case, both values (number.sweeps.sample and number.sweeps.Refs) contain the same value.
- The string machine allows the user to decide which ICPMS instrument was used (provide "ThermoFischer" or "Agilent").
- Using the ThermoFisher Element2 mass spectrometer, the mode of resolution during ablation can be set to low ("LR"), mid ("MR") and high ("HR"). This text string must be provided to enable TERMITE to delete this text string from the header to obtain the names of the isotopes measured during ablation.
- The user can decide which background.correction for the background will be applied ("mean" or "median").
- The section "HelpValues for Linescans" needs to be completed if line scans are evaluated. In case of spot measurements, the values in this section will not be used during calculation and can be left unchanged.
- The values in the section "HelpValues for spot scans" and the reference material must always be provided according to the experiment.
- The first and last value (e.g., the line number) used for the blank calculation need to be filled in as well as the first and last value (e.g. the line number), which will be used for the calculation of the sample (Supplement Figure C.4). Typically, the first and the last one or two values are truncated to ensure consistency of the data. This is done in the section for the line scans as well as the spots.
- The first and the last values (e.g., the line number) used during the calculation of the sample concentration need to be provided in the section for the line scans as well as the spots.
- The scan speed of the laser needs to be provided in the line scan section as this value allows the calculation of the distance of the measurements using the time section of the raw data file.
- In the "Reference Material section" the user can decide which and how many reference materials are used for calibration. The script will only work properly if at least two reference material files from one material are present in the directory. One ablation of the reference materials should be performed before a set of spots (e.g., 30-45 spots) and one after the set. This enables to correct for the drift of

the machine during the analytical session. For each reference material, a Relative Sensitivity Factor (see Manuscript for details) is calculated. Finally, TERMITE applies the mean of the single RSF values to correct the measured element concentrations of the unknown sample.

- Figure 5 shows an example, where two reference materials are used for calibration (e.g., NIST SRM 612 and USGS MACS-3). If only one reference material (for example only NIST612) is used, RefMat line number 2 to 10 should start with a #. All reference materials should be in directly successive lines, i.e., if 3 reference materials are evaluated (e.g., NIST612, MACS3 and NIST610), the # before RefMat3 must be deleted and "KL2-G" must be replaced with "NIST610".
- If no reference material file containing the text string (e.g. "NIST610") is placed in the "ReferenceMaterial_directory", an error will be produced ("Error in file... No such file or directory"). If the correct files are in the directory, but the wrong line is used, an error is produced (e.g., "Error in eval: object "RefMat3" not found"). If these errors occur, the user should check the content of the directory as well as the Reference material section.

16. As a last step, the user should check the complete script again if all values are inserted correctly and then run the script either by executing the whole sequence or every single line individually. Running an R script can be performed either via a Terminal by executing the command 'Rscript TERMITE_spotscan.r' or 'R CMD BATCH TERMITE_spotscan.r' or by marking the whole script and pressing the RUN button (Rstudio).

C.1.3 Troubleshooting

General considerations: Warnings will not stop the script from execution, and the script should finish. Any error that occurs during data reduction will terminate the script and troubleshooting should start. The user is advised to try to understand the error messages provided by R either by reading the provided troubleshooting section or by using a search engine on the internet.

- If the raw data contain any E-values, which are errors introduced during the data saving process, these values will be set to NA prior to data reduction. In R, this will produce warnings, which can be displayed using the command warnings(). The message will be (in short): Warning message: In FUN(x[[i]], ...): NAs introduced by coercion.
- If you receive an "Error in file: cannot open the connection" together with an addition: Warning message: cannot open file, the user should first check if the spelling in the directory section is correct (Supplement Figure C.2).

- If an "Error in file: cannot open the connection with addition: Warning message: In file: cannot open file 'NA': No such file or directory" occurs, the most likely case is a wrong spelling in the Directory section (Supplement Figure C.2). Please also check the spelling of the directory on the hard-drive of your PC. Another reason for this error could be the spelling of the reference material files.
- An "error in pdf cannot open file" is most likely the result of a misspelled directory name. Therefore, the pdf cannot be written.
- An "error in file(file, "rt") : invalid 'description' argument" could occur when more than ONE file is present in the directory Rawdata_linescan (Supplement Figure C.1).
- If other errors occur, please check again all values in the sections for correctness.
- If, in rare cases, R will not stop the calculation for a long time, please consider the amount of data which is evaluated. 24000 spot measurement files will result in TERMITE to work for about 3 h. This will produce a raw count rate file with a size of several GB in size.

```
# ########################################################################## #
# ########################################################################## #
#                                                                            #
#                         TERMITE                                            #
#                                                                            #
#     An R-Skript for fast reduction of LA_ICPMS data and                    #
#       its application to trace element measurements                        #
#                                                                            #
#                         Version 1                                          #
#                                                                            #
#                       Simon Mischel                                        #
#                                                                            #
#   Speleothem Research Group, University Mainz                              #
#                                                                            #
#     eMail: simon.mischel@uni-mainz.de                                      #
#                                                                            #
# ########################################################################## #
# ########################################################################## #
### find . -name "*.csv" -type f -exec cp {} ~/your_folder \;

##### installs all required packages
rm(list=ls(all=TRUE))                                                  # delete the internal R memory to avoid duplicates
if (!require("miscTools"))   install.packages("miscTools", dependencies = TRUE)   # on first run package will be installed if not available
if (!require("matrixStats")) install.packages("matrixStats", dependencies = TRUE) # on first run package will be installed if not available

##### Directory section #####
path                 <- "~/your_main_directory/"               # defining the working-directory of the script
path.rawData.samples  <- "Rawdata_linescan"             # defining the directory of the raw-data-files
path.rawData.RefMat   <- "ReferenceMaterial_linescan"  # defining the directory of the reference material
path.corrData.results <- "Results/"                     # defining the directory for the overview-plots

sample.name           <- "your_sample_name_linescan"                      # is printed in the file-names
```

Figure C.2: Directory section of the script. Slash (/) at the end of the path is mandatory (black arrow).

```
##### general HelpValue Section #####
Mode.of.Scan                <- "line.scan"        # spot.scan or line.scan
Line.of.Header              <- 3                  # the line where the measured isotopes are listed
Line.of.Signal              <- 4                  # the line where the raw data start
measured.isotopes           <- 12                 # number of analysed isotopes
column.IS                   <- 5                  # column of internal standard in the rawdata-file
IS                          <- 400000             # [µg/g] internal standard
outlier.Test                <- "Y"                # "Y" or "N"
m                           <- 30                 # percentage for the range of the outlier test
number.sweeps.sample        <- 6996               # No. of sweeps (e.g. overall number of rows)
number.sweeps.Refs          <- 550                # No. of sweeps (e.g. overall number of rows)
resolution                  <- "(LR)"             # Resolution "(LR)""(MR)""(HR)" (needed for ThermoFischer Element2 ICP-MS)
machine                     <- "Agilent"          # ThermoFischer or. Agilent

background.correction       <- "median"           # method for background.correction (mean <-> median)


##### HelpValue for Linescans Section #####
first.blankValue.linescan   <- 5                  # first Blank-Value (e.g. line number) used for background-correction
last.blankValue.linescan    <- 124                # last  Blank-Value (e.g. line number) used for background-correction

first.sampleValue.linescan  <- 143                # first Laser-on-sample-Value (e.g. line number) used for analysis
last.sampleValue.linescan   <- 6890               # last  Laser-on-sample-Value (e.g. line number) used for analysis

laser.speed                 <- 5                  # laser scan speed in µm/s

##### HelpValues for spot scans and/or reference material Section #####
first.blankValue            <- 5                  # first Blank-Value (e.g. line number) used for background-correction
last.blankValue             <- 124                # last  Blank-Value (e.g. line number) used for background-correction

first.sampleValue           <- 130                # first Laser-on-sample-Value (e.g. line number) used for analysis
last.sampleValue            <- 545                # last  Laser-on-sample-Value (e.g. line number) used for analysis
```

Figure C.3: Section of the script, where all important parameters regarding structure of raw data are filled in. Please change only blue numbers or green text strings with quotation marks.

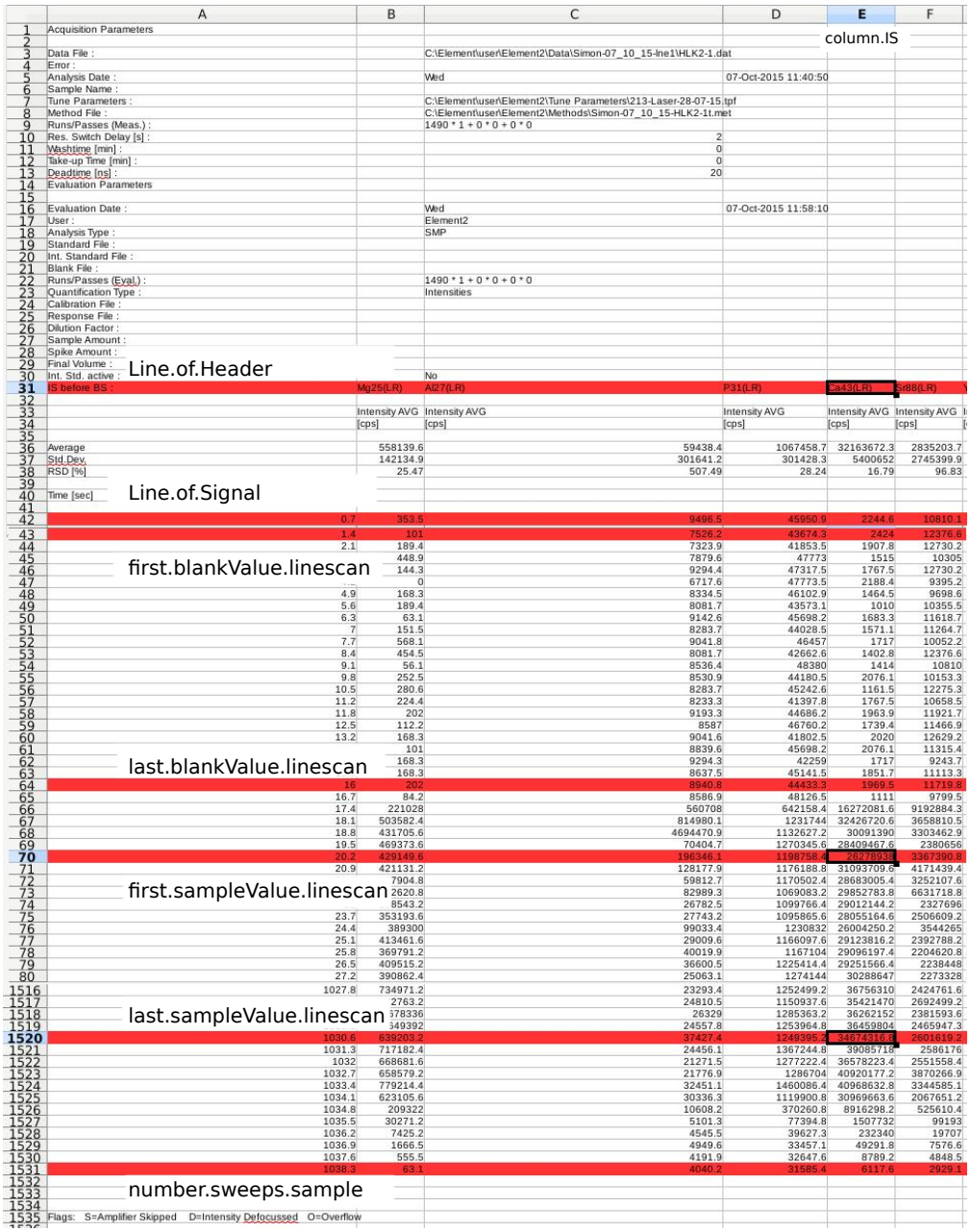

Figure C.4: Example of a raw data file obtained using the Thermo Scientific Element2 ICPMS opened in Microsoft Excel or OpenOffice. Indicated are lines of header, where names of measured elements are found ("Line.of.Header"), and beginning of recorded signal during one laser ablation session ("Line.of.Signal"), which needs to be specified in the script. Also highlighted is the column containing data of the isotope used as internal standard ("column.IS", ^{43}Ca in this example). Lines of first and last blank value used for the calculations are highlighted (first.blankValue.linescan & last.blankValue.linescan) as well as first and last value used for sample (first.sampleValue.linescan & last.sampleValue.linescan). The total number of lines recorded (number.sweeps.sample) is also indicated.

```
##### Reference material Section

##### Values from the GeoReM database (www.http://georem.mpch-mainz.gwdg.de)
##### MPI-DING ATHO-G (ATHO), MPI-DING KL2-G (KL2-G)
##### MPI-DING StHs6/80-G (StHs), MPI-DING T1-G (T1-G)
##### BAM-S005B (BAM-B)
##### USGS MACS-1 (MACS1), USGS MACS-3 (MACS3), USGS GSD-G1 (GSD)
##### NIST SRM 610 (NIST610), NIST SRM 612 (NIST612)

RefMat1     <- "NIST612"  ; Reference.Material <- c(RefMat1)                    # 1. referencematerial
RefMat2     <- "MACS3"    ; Reference.Material <- c(Reference.Material,RefMat2) # 2. referencematerial
#RefMat3    <- "GSD"      ; Reference.Material <- c(Reference.Material,RefMat3) # 3. referencematerial
#RefMat4    <- "KL2-G"    ; Reference.Material <- c(Reference.Material,RefMat4) # 4. referencematerial
#RefMat5    <- "BAM-B"    ; Reference.Material <- c(Reference.Material,RefMat5) # 5. referencematerial
#RefMat6    <- "T1-G"     ; Reference.Material <- c(Reference.Material,RefMat6) # 6. referencematerial
#RefMat7    <- "MACS1"    ; Reference.Material <- c(Reference.Material,RefMat7) # 7. referencematerial
#RefMat8    <- "StHs"     ; Reference.Material <- c(Reference.Material,RefMat8) # 8. referencematerial
#RefMat9    <- "ATHO-G"   ; Reference.Material <- c(Reference.Material,RefMat9) # 9. referencematerial
#RefMat10  <- "NIST610"   ; Reference.Material <- c(Reference.Material,RefMat10)  # 10. referencematerial

##### End HelpValues #####
```

Figure C.5: Section of the script, where all important parameters regarding structure of raw data are filled in. Please change only blue numbers or green text strings with quotation marks.

Bibliography

Alduchov, O. and Eskridge, R. (1996). Improved magnus form approximation of saturation vapor pressure, *J Appl Meterol* **35**(4): 601–609.

Arroyo, L., Trejos, T., Hosick, T., Machemer, S., Almirall, J. R. and Gardinali, P. R. (2010). Analysis of Soils and Sediments by Laser Ablation Inductively Coupled Plasma Mass Spectrometry (LA-ICP-MS): An Innovative Tool for Environmental Forensics, *Environ Forensics* **11**(4): 315–327.

Asrat, A., Baker, A., Leng, M. J., Gunn, J. and Umer, M. (2008). Environmental Monitoring in the Mechara caves, Southeastern Ethiopia: Implications for Speleothem Palaeoclimate Studies, *Int J Speleol* **37**(3): 207–220.

Asrat, A., Baker, A., Mohammed, M. U., Leng, M. J., Van Calsteren, P. and Smith, C. (2007). A high-resolution multi-proxy stalagmite record from Mechara, Southeastern Ethiopia: palaeohydrological implications for speleothem palaeoclimate reconstruction, *J Quat Sci* **22**(1): 53–63.

Ayalon, A., Bar-Matthews, M. and Kaufman, A. (1999). Petrography, strontium, barium and uranium concentrations, and strontium and uranium isotope ratios in speleothems as palaeoclimatic proxies: Soreq Cave, Israel, *Holocene* **9**(6): 715–722.

Baker, A., Wilson, R., Fairchild, I. J., Franke, J., Spötl, C., Mattey, D., Trouet, V. and Fuller, L. (2011). High resolution δ^{18}O and δ^{13}C records from an annually laminated Scottish stalagmite and relationship with last millennium climate, *Global Planet Change* **79**(3–4): 303 – 311.

Baldini, L. M., McDermott, F., Foley, A. M. and Baldini, J. U. L. (2008). Spatial variability in the European winter precipitation delta(18)O-NAO relationship: implications for reconstructing NAO-mode climate variability in the Holocene, *Geophys Res Lett* **35**(4): L04709.

Bengtsson, H. (2015). *matrixStats: Methods that Apply to Rows and Columns of Matrices (and to Vectors)*. R package version 0.14.2.

Björck, S., Kromer, B., Johnsen, S., Bennike, O., Hammarlund, D., Lemdahl, G., Possnert, G., Rasmussen, T., Wohlfarth, B., Hammer, C. and Spurk, M. (1996). Synchronized terrestrial-atmospheric deglacial records around the North Atlantic, *Science* **274**(5290): 1155–1160.

Boch, R., Spotl, C. and Kramers, J. (2009). High-resolution isotope records of early Holocene rapid climate change from two coeval stalagmites of Katerloch Cave, Austria, *Quat Sci Rev* **28**(23-24): 2527–2538.

Bond, G., Kromer, B., Beer, J., Muscheler, R., Evans, M. N., Showers, W., Hoffmann, S., Lotti-Bond, R., Hajdas, I. and Bonani, G. (2001). Persistent solar influence on north Atlantic climate during the Holocene, *Science* **294**(5549): 2130–2136.

Bond, G., Showers, W., Cheseby, M., Lotti, R., Almasi, P., deMenocal, P., Priore, P., Cullen, H., Hajdas, I. and Bonani, G. (1997). A Pervasive Millennial-Scale Cycle in North Atlantic Holocene and Glacial Climates, *Science* **278**(5341): 1257–1266.

Borsato, A., Frisia, S., Fairchild, I. J., Somogyi, A. and Susini, J. (2007). Trace element distribution in annual stalagmite laminae mapped by micrometer-resolution X-ray fluorescence: Implications for incorporation of environmentally significant species, *Geochim Cosmochim Acta* **71**(6): 1494–1512.

Bosle, J. M., Mischel, S. A., Schulze, A.-L., Scholz, D. and Hoffmann, T. (2014). Quantification of low molecular weight fatty acids in cave drip water and speleothems using HPLC-ESI-IT/MS - development and validation of a selective method, *Anal Bioanal Chem* **406**(13): 3167–3177.

Casty, C., Wanner, H., Luterbacher, J., Esper, J. and Bohm, R. (2005). Temperature and precipitation variability in the European Alps since 1500, *Int J Climatol* **25**(14): 1855–1880.

Cerling, T. E. (1984). The stable isotopic composition of modern soil carbonate and its relationship to climate, *Earth Planet Sci Lett* **71**(2): 229 – 240.

Cheng, H., Edwards, R. L., Hoff, J., Gallup, C. D., Richards, D. A. and Asmerom, Y. (2000). The half-lives of uranium-234 and thorium-230, *Chem Geol* **169**(1-2): 17–33.

Comas-Bru, L. and McDermott, F. (2013). Impacts of the EA and SCA patterns on the European twentieth century NAO-winter climate relationship, *Q J R Meteorol Soc* **140**(679): 354–363.

Cook, E. R., D'Arrigo, R. D. and Briffa, K. R. (1998). A reconstruction of the North Atlantic Oscillation using tree-ring chronologies from North America and Europe, *Holocene* **8**(1): 9–17.

Coursey, J., Schwab, D., Tsai, J. and Dragoset, R. (2015). Atomic weights and isotopic compositions.
URL: *version 4.1 http://www.nist.gov/pml/data/comp.cfm*

Davis, B. A. S., Brewer, S., Stevenson, A. C. and Guiot, J. (2003). The temperature of Europe during the Holocene reconstructed from pollen data, *Quat Sci Rev* **22**(15-17): 1701–1716.

Day, C. and Henderson, G. (2011). Oxygen isotopes in calcite grown under cave-analogue conditions, *Geochim Cosmochim Acta* **75**(14): 3956–3972.

Deconinck, I., Latkoczy, C., Gunther, D., Govaert, F. and Vanhaecke, F. (2006). Capabilities of laser ablation-inductively coupled plasma mass spectrometry for (trace) element analysis of car paints for forensic purposes, *J Anal At Spectrom* **21**(3): 279–287.

Deininger, M., Fohlmeister, J., Scholz, D. and Mangini, A. (2012). Isotope disequilibrium effects: The influence of evaporation and ventilation effects on the carbon and oxygen isotope composition of speleothems-A model approach, *Geochim Cosmochim Acta* **96**: 57–79.

Domínguez-Villar, D., Lojen, S., Krklec, K., Baker, A. and Fairchild, I. J. (2015). Is global warming affecting cave temperatures? Experimental and model data from a paradigmatic case study, *Clim Dyn* **45**(3-4): 569–581.

Dreybrodt, W. and Scholz, D. (2011). Climatic dependence of stable carbon and oxygen isotope signals recorded in speleothems: from soil water to speleothem calcite, *Geochim Cosmochim Acta* **75**(3): 734–752.

Dykoski, C., Edwards, R., Cheng, H., Yuan, D., Cai, Y., Zhang, M., Lin, Y., Qing, J., An, Z. and Revenaugh, J. (2005). A high-resolution, absolute-dated Holocene and deglacial Asian monsoon record from Dongge Cave, China, *Earth Planet Sci Lett* **233**(1-2): 71–86.

Fairchild, I. J. and Baker, A. (2012). *Speleothem science: from process to past environments*, Wiley-Blackwell, Chichester, pp432.

Fairchild, I. J., Borsato, A., Tooth, A. F., Frisia, S., Hawkesworth, C. J., Huang, Y., McDermott, F. and Spiro, B. (2000). Controls on trace element (Sr–Mg) compositions of carbonate cave waters: implications for speleothem climatic records, *Chem Geol* **166**(3–4): 255 – 269.

Fairchild, I. J. and McMillan, E. A. (2007). Speleothems as indicators of wet and dry periods, *Int J Speleol* **36**(2): 69–74.

Fairchild, I. J., Smith, C. L., Baker, A., Fuller, L., Spotl, C., Mattey, D. and McDermott, F. (2006). Modification and preservation of environmental signals in speleothems, *Earth Sci Rev* **75**(1-4): 105–153.

Fairchild, I. J. and Treble, P. C. (2009). Trace elements in speleothems as recorders of environmental change, *Quat Sci Rev* **28**(5-6): 449–468.

Felis, T., Lohmann, G., Kuhnert, H., Lorenz, S., Scholz, D., Patzold, J., Al-Rousan, S. and Al-Moghrabi, S. (2004). Increased seasonality in Middle East temperatures during the last interglacial period, *Nature* **429**(6988): 164–168.

Finch, A. A., Shaw, P. A., Holmgren, K. and Lee-Thorp, J. (2003). Corroborated rainfall records from aragonitic stalagmites, *Earth Planet Sci Lett* **215**(1-2): 265–273.

Fohlmeister, J., Scholz, D., Kromer, B. and Mangini, A. (2011). Modelling carbon isotopes of carbonates in cave drip water, *Geochim Cosmochim Acta* **75**(18): 5219–5228.

Fohlmeister, J., Schroder-Ritzrau, A., Scholz, D., Spotl, C., Riechelmann, D. F. C., Mudelsee, M., Wackerbarth, A., Gerdes, A., Riechelmann, S., Immenhauser, A., Richter, D. K. and Mangini, A. (2012). Bunker Cave stalagmites: an archive for central European Holocene climate variability, *Clim Past* **8**(5): 1751–1764.

Foley, S. F., Prelevic, D., Rehfeldt, T. and Jacob, D. E. (2013). Minor and trace elements in olivines as probes into early igneous and mantle melting processes, *Earth Planet Sci Lett* **363**: 181–191.

Ford, D. and Williams, P. W. (2007). *Karst hydrology and geomorphology*, John Wiley & Sons, Ltd.

Frisia, S., Borsato, A., Preto, N. and McDermott, F. (2003). Late Holocene annual growth in three Alpine stalagmites records the influence of solar activity and the North Atlantic Oscillation on winter climate, *Earth Planet Sci Lett* **216**(3): 411–424.

Genty, D. (2008). Palaeoclimate Research in Villars Cave (Dordogne, SW-France), *Int J Speleol* **37**(3): 173–191.

Genty, D., Labuhn, I., Hoffmann, G., Danis, P., Mestre, O., Bourges, F., Wainer, K., Massault, M., Exter, S. V., Régnier, E., Orengo, P., Falourd, S. and Minster, B. (2014). Rainfall and cave water isotopic relationships in two South-France sites, *Geochim Cosmochim Acta* **131**: 323 – 343.

Gluhak, T. M. and Rosenberg, D. (2013). Geochemical discrimination of basaltic sources as a tool for provenance analyses of bifacial tools in the southern Levant: first results from the Jezreel Valley, Israel, *J Archaeol Sci* **40**(3): 1611–1622.

Goede, A. and Vogel, J. C. (1991). Trace-element Variations and Dating of A Late Pleistocene Tasmanian Speleothem, *Palaeogeogr Palaeoclimatol Palaeoecol* **88**(1-2): 121–131.

Griffin, W., Powell, W., Pearson, N. and O'Reilly, S. (2008). *Laser Ablation-ICP-MS in the Earth Sciences. Current Practices and outstanding issues.*, number 40 in *Short Course Ser - Mineral Assoc Can*, chapter Appendix A2: Glitter: Data reduction software for Laser Ablation ICP-MS, pp. 308–311.

Griffiths, M. L., Fohlmeister, J., Drysdale, R. N., Hua, Q., Johnson, K. R., Hellstrom, J. C., Gagan, M. K. and Zhao, J. x. (2012). Hydrological control of the dead carbon fraction in a Holocene tropical speleothem, *Quat Geochronol* **14**: 81–93.

Guillong, M., Meier, D., Allan, M., Heinrich, C. and Yardley, B. (2008). *Laser Ablation-ICP-MS in the Earth Sciences. Current Practices and outstanding issues.*, number 40 in *Short Course Ser - Mineral Assoc Can*, chapter Appendix A6: SILLS: A Matlab-based program for the reduction of laser ablation ICP-MS data of homogeneous materials and inclusions, pp. 328–333.

Hansen, M., Dreybrodt, W. and Scholz, D. (2013). Chemical evolution of dissolved inorganic carbon species flowing in thin water films and its implications for (rapid) degassing of CO_2 during speleothem growth, *Geochim Cosmochim Acta* **107**: 242–251.

Haude, W. (1954). Zur praktischen Bestimmung der aktuellen und potentiellen Evapotranspiration, *Mitt Dtsch Wetterd* **8**: 1–15.

Haude, W. (1955). Zur Bestimmung der Verdunstung auf möglichst einfache Weise, *Mitt Dt Wetterd* **11**(2): 1–24.

Hellstrom, J. C. and McCulloch, M. T. (2000). Multi-proxy constraints on the climatic significance of trace element records from a New Zealand speleothem, *Earth Planet Sci Lett* **179**(2): 287–297.

Hellstrom, J. C., Paton, C., Woodhead, J. and Hergt, J. (2008). *Laser Ablation-ICP-MS in the Earth Sciences. Current Practices and outstanding issues.*, number 40 in *Short Course Ser - Mineral Assoc Can*, chapter Chapter A9: Iolite: Software for spacially resolved LA-(Quad and MC)-ICP-MS analysis, pp. 343–348.

Henderson, G. M. (2006). Climate - Caving in to new chronologies, *Science* **313**(5787): 620–622.

Henningsen, A. and Toomet, O. (2013). *miscTools: Miscellaneous Tools and Utilities*. R package version 0.6-16.
URL: *http://CRAN.R-project.org/package=miscTools*

Hettmann, K., Kreissig, K., Rehkaemper, M., Wenzel, T., Mertz-Kraus, R. and Markl, G. (2014). Thallium geochemistry in the metamorphic Lengenbach sulfide deposit, Switzerland: Thallium-isotope fractionation in a sulfide melt, *Am Mineral* **99**(4): 793–803.

Hoffmann, D. L., Prytulak, J., Richards, D. A., Elliott, T., Coath, C. D., Smart, P. L. and Scholz, D. (2007). Procedures for accurate U and Th isotope measurements by high precision MC-ICPMS, *Int J Mass Spectrom* **264**(2-3): 97–109.

Huang, H. M., Fairchild, I. J., Borsato, A., Frisia, S., Cassidy, N. J., McDermott, F. and Hawkesworth, C. J. (2001). Seasonal variations in Sr, Mg and P in modern speleothems (Grotta di Ernesto, Italy), *Chem Geol* **175**(3-4): 429–448.

Hurrell, J. W. (1995). Decadal Trends In the North-atlantic oscillation - regional temperatures and precipitation, *Science* **269**(5224): 676–679.

IAEA/WMO (2014). Global Network of Isotopes in Precipitation. The GNIP Database, *http://www.iaea.org/water* . Accessed 05 June 2014.

Jochum, K. P., Nohl, L., Herwig, K., Lammel, E., Stoll, B. and Hofmann, A. W. (2005). GeoReM: A new geochemical database for reference materials and isotopic standards, *Geostand Geoanal Res* **29**(3): 333–338.

Jochum, K. P., Scholz, D., Stoll, B., Weis, U., Wilson, S. A., Yang, Q., Schwalb, A., Boerner, N., Jacob, D. E. and Andreae, M. O. (2012). Accurate trace element analysis of speleothems and biogenic calcium carbonates by LA-ICP-MS, *Chem Geol* **318**: 31–44.

Jochum, K. P., Stoll, B., Herwig, K. and Willbold, M. (2007). Validation of LA-ICP-MS trace element analysis of geological glasses using a new solid-state 193 nm Nd : YAG laser and matrix-matched calibration, *J Anal At Spectrom* **22**(2): 112–121.

Johnson, K., Hu, C., Belshaw, N. and Henderson, G. (2006). Seasonal trace-element and stable-isotope variations in a Chinese speleothem: The potential for high-resolution paleomonsoon reconstruction, *Earth Planet Sci Lett* **244**(1-2): 394–407.

Jolliffe, I. (2002). *Principal Component Analysis*, Springer Series in Statistics.

Jones, P. D., Jonsson, T. and Wheeler, D. (1997). Extension to the North Atlantic Oscillation using early instrumental pressure observations from Gibraltar and south-west Iceland, *Int J Climatol* **17**(13): 1433–1450.

Jouzel, J., Hoffmann, G., Koster, K. and Masson, V. (2000). Water isotopes in precipitation: data/model comparison for present-day and past climates, *Quat Sci Rev* **19**: 363–379.

Kluge, T., Affek, H. P., Marx, T., Aeschbach-Hertig, W., Riechelmann, D. F. C., Scholz, D., Riechelmann, S., Immenhauser, A., Richter, D. K., Fohlmeister, J., Wackerbarth, A., Mangini, A. and Spoetl, C. (2013). Reconstruction of drip-water delta O-18 based on calcite oxygen and clumped isotopes of speleothems from Bunker Cave (Germany), *Clim Past* **9**(1): 377–391.

Kluge, T., Riechelmann, D. F. C., Wieser, M., Spotl, C., Sultenfuss, J., Schroder-Ritzrau, A., Niggemann, S. and Aeschbach-Hertig, W. (2010). Dating cave drip water by tritium, *J Hydrol* **394**(3-4): 396–406.

Kotlia, B. S., Ahmad, S. M., Zhao, J.-X., Raza, W., Collerson, K. D., Joshi, L. M. and Sanwal, J. (2012). Climatic fluctuations during the LIA and post-LIA in the Kumaun Lesser Himalaya, India: Evidence from a 400 y old stalagmite record, *Quat Int* **263**: 129–138.

Kotzeva, B. G., Guillong, M., Stefanova, E. and Piperov, N. B. (2011). LA-ICP-MS analysis of single fluid inclusions in a quartz crystal (Madan ore district, Bulgaria) , *J Geochem Explor* **108**(3): 163 – 175.

Labuhn, I., Genty, D., Vonhof, H., Bourdin, C., Blamart, D., Douville, E., Ruan, J., Cheng, H., Edwards, L. R., Pons-Branchu, E. and Pierre, M. (2015). A high-resolution fluid inclusion delta O-80 record from a stalagmite in SW France: modern calibration and comparison with multiple proxies, *Quat Sci Rev* **110**: 152–165.

Lachniet, M. S. (2009). Climatic and environmental controls on speleothem oxygen-isotope values, *Quat Sci J Rev* **28**(5-6): 412–432.

Langebroek, P., Werner, M. and Lohmann, G. (2011). Climate information imprinted in oxygen-isotopic composition of precipitation in Europe, *Earth Planet Sci Lett* **311**(1-2): 144–154.

Lauritzen, S. E. and Lundberg, J. (1999). Speleothems and climate: a special issue of The Holocene, *Holocene* **9**(6): 643–647.

Lawrence, D. M., Thornton, P. E., Oleson, K. W. and Bonan, G. B. (2007). The partitioning of evapotranspiration into transpiration, soil evaporation, and canopy evaporation in a GCM: Impacts on land-atmosphere interaction, *J Hydrometeorol* **8**(4): 862–880.

Litt, T., Schmincke, H.-U. and Kromer, B. (2003). Environmental response to climatic and volcanic events in central Europe during the Weichselian Lateglacial, *Quat Sci Rev* **22**(1): 7–32.

Litt, T., Scholzel, C., Kuhl, N. and Brauer, A. (2009). Vegetation and climate history in the Westeifel Volcanic Field (Germany) during the past 11 000 years based on annually laminated lacustrine maar sediments, *Boreas* **38**(4): 679–690.

Litt, T. and Stebich, M. (1999). Bio- and chronostratigraphy of the lateglacial in the Eifel region, Germany, *Quat Int* **61**: 5–16.

Liu, H., Mao, X. and Russo, R. (2001). Representative sampling using single-pulse laser ablation with inductively coupled plasma mass spectrometry, *J Anal At Spectrom* **16**(10): 1115–1120.

Longerich, H., Jackson, S. and Gunther, D. (1996). Laser ablation inductively coupled plasma mass spectrometric transient signal data acquisition and analyte concentration calculation, *J Anal At Spectrom* **11**(9): 899–904.

Luetscher, M. and Ziegler, F. (2012). CORA - a dedicated device for carbon dioxide monitoring in cave environments, *Int J Speleol* **41**(2): 273–281.

Luterbacher, J., Xoplaki, E., Dietrich, D., Jones, P. D., Davies, T. D., Portis, D., Gonzalez-Rouco, J. F., von Storch, H., Gyalistras, D., Casty, C. and Wanner, H. (2001). Extending North Atlantic Oscillation reconstructions back to 1500, *Atmos Sci Lett* **2**(1-4): 114–124.

Macholdt, D. S., Jochum, K. P., Stoll, B., Weis, U. and Andreae, M. O. (2014). A new technique to determine element amounts down to femtograms in dust using femtosecond laser ablation-inductively coupled plasma-mass spectrometry, *Chem Geol* **383**: 123–131.

Mangini, A., Spötl, C. and Verdes, P. (2005). Reconstruction of temperature in the Central Alps during the past 2000 yr from a δ^{18}O stalagmite record, *Earth Planet Sci Lett* **235**(3–4): 741 – 751.

Mangini, A., Verdes, P., Spoetl, C., Scholz, D., Vollweiler, N. and Kromer, B. (2007). Persistent influence of the North Atlantic hydrography on central European winter temperature during the last 9000 years, *Geophys Res Lett* **34**(2).

Mattey, D., Lowry, D., Duffet, J., Fisher, R., Hodge, E. and Frisia, S. (2008). A 53 year seasonally resolved oxygen and carbon isotope record from a modem Gibraltar speleothem: Reconstructed drip water and relationship to local precipitation, *Earth Planet Sci Lett* **269**(1-2): 80–95.

McDermott, F. (2004). Palaeo-climate reconstruction from stable isotope variations in speleothems: a review, *Quat Sci Rev* **23**(7-8): 901–918.

McDermott, F., Frisia, S., Huang, Y. M., Longinelli, A., Spiro, B., Heaton, T. H. E., Hawkesworth, C. J., Borsato, A., Keppens, E., Fairchild, I. J., van der Borg, K., Verheyden, S. and Selmo, E. (1999). Holocene climate variability in Europe: Evidence from delta O-18, textural and extension-rate variations in three speleothems, *Quat Sci Rev* **18**(8-9): 1021–1038.

McDonald, J., Drysdale, R., Hill, D., Chisari, R. and Wong, H. (2007). The hydrochemical response of cave drip waters to sub-annual and inter-annual climate variability, Wombeyan Caves, SE Australia, *Chem Geol* **244**(3-4): 605–623.

McMillan, E. A., Fairchild, I. J., Frisia, S., Borsato, A. and McDermott, F. (2005). Annual trace element cycles in calcite-aragonite speleothems: evidence of drought in the western Mediterranean 1200-1100 yr BP, *J Quat Sci* **20**(5): 423–433.

Mertz-Kraus, R., Brachert, T. C., Jochum, K. P., Reuter, M. and Stoll, B. (2009). LA-ICP-MS analyses on coral growth increments reveal heavy winter rain in the Eastern Mediterranean at 9 Ma, *Palaeogeogr Palaeoclimatol Palaeoecol* **273**(1-2): 25–40.

Meyer, M. C., Spotl, C. and Mangini, A. (2008). The demise of the Last Interglacial recorded in isotopically dated speleothems from the Alps, *Quat Sci Rev* **27**(5-6): 476–496.

Mickler, P. J., Stern, L. A. and Banner, J. L. (2006). Large kinetic isotope effects in modern speleothems, *Geol Soc Am Bull* **118**(1-2): 65–81.

Mischel, S. A. (2010). Petrographische Untersuchungen, ^{230}Th\U-Altersdatierungen und Spurenelementanalysen an Speläothemen aus dem Herbstlabyrinth-Adventhöhle-System bei Breitscheid-Erdbach, Hessen. unpublished diploma-thesis.

Mischel, S. A., Mertz-Kraus, R., Jochum, K. P. and Scholz, D. (2016). TERMITE - An R script for fast reduction of LA-ICPMS data and its application to trace element measurements, *submitted* .

Mischel, S. A., Scholz, D. and Spötl, C. (2015). δ^{18}O values of cave drip water: a promising proxy for the reconstruction of the North Atlantic Oscillation?, *Clim Dyn* **45**: 3035–3050.

Mischel, S. A., Scholz, D., Spötl, C., Jochum, K. P., Schröder-Ritzrau, A. and Fiedler, S. (accepted). Holocene climate variability in central Germany and a potential link to the polar North Atlantic - a replicated record from three coeval speleothems, *Holocene* .

Munoz-Diaz, D. and Rodrigo, F. S. (2003). Effects of the North Atlantic oscillation on the probability for climatic categories of local monthly rainfall in southern Spain, *Int Climatol* **23**(4): 381–397.

Mühlinghaus, C., Scholz, D. and Mangini, A. (2009). Modelling fractionation of stable isotopes in stalagmites, *Geochim Cosmochim Acta* **73**(24): 7275–7289.

Niggemann, S., Mangini, A., Richter, D. K. and Wurth, G. (2003). A paleoclimate record of the last 17,600 years in stalagmites from the B7 cave, Sauerland, Germany, *Quat Sci Rev* **22**(5-7): 555–567.

Noronha, A. L., Johnson, K. R., Hu, C., Ruan, J., Southon, J. R. and Ferguson, J. E. (2014). Assessing influences on speleothem dead carbon variability over the Holocene: Implications for speleothem-based radiocarbon calibration, *Earth Planet Sci Lett* **394**: 20–29.

Obert, J. C., Scholz, D., Felis, T., Brocas, W. M., Jochum, K. P. and Andreae, M. O. (2016). ^{230}Th/U dating of Last Interglacial brain corals from Bonaire (southern Caribbean) using bulk and theca wall material, *Geochim Cosmochim Acta* **178**: 20 – 40.

Olsen, J., Anderson, N. J. and Knudsen, M. F. (2012). Variability of the North Atlantic Oscillation over the past 5,200 years, *Nat Geosci* **5**(11): 808–812.

R Core Team (2016). *R: A Language and Environment for Statistical Computing*, R Foundation for Statistical Computing, Vienna, Austria.
URL: *https://www.R-project.org/*

Rasmussen, S., Andersen, K., Svensson, A., Steffensen, J., Vinther, B., Clausen, H., Siggaard-Andersen, M., Johnsen, S., Larsen, L., Dahl-Jensen, D., Bigler, M., Rothlisberger, R., Fischer, H., Goto-Azuma, K., Hansson, M. and Ruth, U. (2006). A new Greenland ice core chronology for the last glacial termination, *J Geophys Res: Atmosph* **111**(D6).

Renger, M., Strebel, O., Wessolek, G. and Duynisveld, W. H. M. (1974). Evapotranspiration and groundwater recharge – a case study from different climate, crop patterns, soil properties and groundwater depth conditions, *Z Pflanzenernaehr Bodenk* **149**: 371–381.

Revelle, W. (2015). *psych: Procedures for Psychological, Psychometric, and Personality Research*, Northwestern University, Evanston, Illinois. R package version 1.5.4.
URL: *http://CRAN.R-project.org/package=psych*

Richards, D. A. and Dorale, J. A. (2003). Uranium-series chronology and environmental applications of speleothems, *Uranium-series Geochem* **52**: 407–460.

Richter, D. K., Meissner, P., Immenhauser, A., Schulte, U. and Dorsten, I. (2010). Cryogenic and non-cryogenic pool calcites indicating permafrost and non-permafrost periods: a case study from the Herbstlabyrinth-Advent Cave system (Germany), *Cryosphere* **4**(4): 501–509.

Riechelmann, D. F. C., Schröder-Ritzrau, A., Scholz, D., Fohlmeister, J., Spötl, C., Richter, D. K. and Mangini, A. (2011). Monitoring Bunker Cave (NW Germany): A prerequisite to interpret geochemical proxy data of speleothems from this site, *J Hydrol* **409**(3-4): 682–695.

Riechelmann, D. F., Deininger, M., Scholz, D., Riechelmann, S., Schröder-Ritzrau, A., Spötl, C., Richter, D. K., Mangini, A. and Immenhauser, A. (2013). Disequilibrium carbon and oxygen isotope fractionation in recent cave calcite: Comparison of cave precipitates and model data, *Geochim Cosmochim Acta* **103**(0): 232–244.

Rittner, M. and Mueller, W. (2012). 2D mapping of LA-ICPMS trace element distributions using R, *Comput Geosci* **42**: 152–161.

Roberts, M. S., Smart, P. L. and Baker, A. (1998). Annual trace element variations in a Holocene speleothem, *Earth Planet Sci Lett* **154**(1-4): 237–246.

Roberts, M. S., Smart, P. L., Hawkesworth, C. J., Perkins, W. T. and Pearce, N. J. G. (1999). Trace element variations in coeval Holocene speleothems from GB cave, southwest England, *Holocene* **9**(6): 707–713.

Schiff, H. (1975). Berechnung der potentiellen Verdunstung und deren Vergleich mit aktuellen Verdunstungswerten von Lysimetern, *Arch Met Geoph Biokl Ser B* **23**(4): 331–342.

Scholz, D., Frisia, S., Borsato, A., Spoetl, C., Fohlmeister, J., Mudelsee, M., Miorandi, R. and Mangini, A. (2012). Holocene climate variability in north-eastern Italy: potential influence of the NAO and solar activity recorded by speleothem data, *Clim Past* **8**(4): 1367–1383.

Scholz, D. and Hoffmann, D. L. (2008). ^{230}Th/U-dating of fossil corals and speleothems, *Quat Sci J* **57**(1-2): 52–76.

Scholz, D. and Hoffmann, D. L. (2011). StalAge - An algorithm designed for construction of speleothem age models, *Quat Geochronol* **6**(3-4): 369–382.

Scholz, D., Muehlinghaus, C. and Mangini, A. (2009). Modelling delta C-13 and delta O-18 in the solution layer on stalagmite surfaces, *Geochim Cosmochim Acta* **73**(9): 2592–2602.

Scholz, D., Tolzmann, J., Hoffmann, D. L., Jochum, K. P., Spoetl, C. and Riechelmann, D. F. C. (2014). Diagenesis of speleothems and its effect on the accuracy of Th-230/U-ages, *Chem Geol* **387**: 74–86.

Seppa, H., Birks, H. J. B., Giesecke, T., Hammarlund, D., Alenius, T., Antonsson, K., Bjune, A. E., Heikkila, M., MacDonald, G. M., Ojala, A. E. K., Telford, R. J. and Veski, S. (2007). Spatial structure of the 8200 cal yr BP event in northern Europe, *Clim Past* **3**(2): 225–236.

Solari, L. A. and Tanner, M. (2011). UPb.age, a fast data reduction script for LA-ICP-MS U-Pb geochronology, *Rev Mex Cienc Geol* **28**(1): 83–91.

Spötl, C., Fairchild, I. J. and Tooth, A. F. (2005). Cave air control on dripwater geochemistry, Obir Caves (Austria): Implications for speleothem deposition in dynamically ventilated caves, *Geochim Cosmochim Acta* **69**(10): 2451–2468.

Spötl, C. and Mangini, A. (2007). Speleothems and paleoglaciers, *Earth Planet Sci Lett* **254**(3–4): 323–331.

Spötl, C. and Mattey, D. (2006). Stable isotope microsampling of speleothems for palaeoenvironmental studies: A comparison of microdrill, micromill and laser ablation techniques, *Chem Geol* **235**(1:2): 48–58.

Spötl, C., Scholz, D. and Mangini, A. (2008). A terrestrial U/Th-dated stable isotope record of the Penultimate Interglacial, *Earth Planet Sci Lett* **276**(3–4): 283–292.

Spötl, C. and Vennemann, T. W. (2003). Continuous-flow isotope ratio mass spectrometric analysis of carbonate minerals, *Rapid Comm Mass Spec* **17**(9): 1004–1006.

Steffensen, J. P., Andersen, K. K., Bigler, M., Clausen, H. B., Dahl-Jensen, D., Fischer, H., Goto-Azuma, K., Hansson, M., Johnsen, S. J., Jouzel, J., Masson-Delmotte, V., Popp, T., Rasmussen, S. O., Roethlisberger, R., Ruth, U., Stauffer, B., Siggaard-Andersen, M.-L., Sveinbjornsdottir, A. E., Svensson, A. and White, J. W. C. (2008). High-resolution Greenland Ice Core data show abrupt climate change happens in few years, *Science* **321**(5889): 680–684.

Stoll, H. M., Mueller, W. and Prieto, M. (2012). I-STAL, a model for interpretation of Mg/Ca, Sr/Ca and Ba/Ca variations in speleothems and its forward and inverse application on seasonal to millennial scales, *Geochem Geophys Geosys* **13**.

Stummp, C., Klaus, J. and Stichler, W. (2014). Analysis of long-term stable isotopic composition in German precipitation, *J Hydrol* **517**: 351–361.

Sutanto, S. J., Wenninger, J., Coenders-Gerrits, A. M. J. and Uhlenbrook, S. (2012). Partitioning of evaporation into transpiration, soil evaporation and interception: a comparison between isotope measurements and a HYDRUS-1D model, *Hydrol Earth Syst Sci* **16**(8): 2605–2616.

Tooth, A. F. and Fairchild, I. J. (2003). Soil and karst aquifer hydrological controls on the geochemical evolution of speleothem-forming drip waters, Crag Cave, southwest Ireland, *J Hydrol* **273**(1-4): 51–68.

Treble, P., Shelley, J. M. G. and Chappell, J. (2003). Comparison of high resolution sub-annual records of trace elements in a modern (1911-1992) speleothem with instrumental climate data from southwest Australia, *Earth Planet Sci Lett* **216**(1-2): 141–153.

Tremaine, D. M., Froelich, P. N. and Wang, Y. (2011). Speleothem calcite farmed in situ: Modern calibration of δ^{18}O and δ^{13}C paleoclimate proxies in a continuously-monitored natural cave system, *Geochim Cosmochim Acta* **75**(17): 4929–4950.

Trigo, R. M., Osborn, T. J. and Corte-Real, J. M. (2002). The North Atlantic Oscillation influence on Europe: climate impacts and associated physical mechanisms, *Clim Res* **20**(1): 9–17.

Trouet, V., Esper, J., Graham, N. E., Baker, A., Scourse, J. D. and Frank, D. C. (2009). Persistent positive North Atlantic Oscillation Mode Dominated the Medieval Climate Anomaly, *Science* **324**(5923): 78–80.

van Beynen, P. E., Asmerom, Y., Polyak, V., Soto, L. and Polk, J. S. (2007). Variable intensity of teleconnections during the late Holocene in subtropical North America from an isotopic study of speleothem from Florida, *Geophys Res Lett* **34**(18): L18703.

van Beynen, P. E., Soto, L. and Pace-Graczyk, K. (2008). Paleoclimate reconstruction derived from speleothem strontium and delta C-13 in Central Florida, *Quat Int* **187**: 76–83.

Verheyden, S. (2004). Trace elements in speleothems. A short review of the state of the art., *Int J Speleol* **33**: 95–101.

Vinther, B. M., Clausen, H. B., Johnsen, S. J., Rasmussen, S. O., Andersen, K. K., Buchardt, S. L., Dahl-Jensen, D., Seierstad, I. K., Siggaard-Andersen, M.-L., Steffensen, J. P., Svensson, A., Olsen, J. and Heinemeier, J. (2006). A synchronized dating of three Greenland ice cores throughout the Holocene, *J Geophys Res: Atmosph* **111**(D13). D13102.

Vollweiler, N., Scholz, D., Muehlinghaus, C., Mangini, A. and Spoetl, C. (2006). A precisely dated climate record for the last 9 kyr from three high alpine stalagmites, Spannagel Cave, Austria, *Geophys Res Lett* **33**(20): L20703.

von Grafenstein, U., Erlenkeuser, H., Brauer, A., Jouzel, J. and Johnsen, S. (1999). A mid-European decadal isotope-climate record from 15,500 to 5000 years BP, *Science* **284**(5420): 1654–1657.

Wackerbarth, A., Scholz, D., Fohlmeister, J. and Mangini, A. (2010). Modelling the $\delta^{18}O$ value of cave drip water and speleothem calcite, *Earth Planet Sci Lett* **299**(3-4): 387–397.

Walker, M., Johnsen, S., Rasmussen, S. O., Popp, T., Steffensen, J.-P., Gibbard, P., Hoek, W., Lowe, J., Andrews, J., Björck, S., Cwynar, L. C., Hughen, K., Kershaw, P., Kromer, B., Litt, T., Lowe, D. J., Nakagawa, T., Newnham, R. and Schwander, J. (2009). Formal definition and dating of the GSSP (Global Stratotype Section and Point) for the base of the Holocene using the Greenland NGRIP ice core, and selected auxiliary records, *J Quat Sci* **24**(1): 3–17.

Wang, Z., Hattendorf, B. and Gunther, D. (2006). Analyte response in laser ablation inductively coupled plasma mass spectrometry, *J Am Soc Mass Spectrom* **17**(5): 641–651.

Wassenburg, J. A., Immenhauser, A., Richter, D. K., Jochum, K. P., Fietzke, J., Deininger, M., Goos, M., Scholz, D. and Sabaoui, A. (2012). Climate and cave control on Pleistocene/Holocene calcite-to-aragonite transitions in speleothems from Morocco: Elemental and isotopic evidence, *Geochim Cosmochim Acta* **92**(0): 23–47.

Wassenburg, J., Immenhauser, A., Richter, D., Niedermayr, A., Riechelmann, S., Fietzke, J., Scholz, D., Jochum, K., Fohlmeister, J., Schröder-Ritzrau, A., Sabaoui, A., Riechelmann, D., Schneider, L. and Esper, J. (2013). Moroccan speleothem and tree ring records suggest a variable positive state of the North Atlantic Oscillation during the Medieval Warm Period, *Earth Planet Sci Lett* **375**(0): 291–302.

Williams, P. W. (2008). The role of the epikarst in karst and cave hydrogeology: a review, *Int J Speleol* **37**(1): 1–10.

Yang, Q., Jochum, K. P., Stoll, B., Weis, U., Boerner, N., Schwalb, A., Frenzel, P., Scholz, D., Doberschuetz, S., Haberzettl, T., Gleixner, G., Maeusbacher, R., Zhu, L. and Andreae, M. O. (2014). Trace element variability in single ostracod valves as a proxy for hydrochemical change in Nam Co, central Tibet, during the Holocene, *Palaeogeogr Palaeoclimatol Palaeoecol* **399**: 225–235.

Yang, Q., Scholz, D., Jochum, K. P., Hoffmann, D. L., Stoll, B., Weis, U. Schwager, B. and A., M. O. (2015). Lead isotope variability in speleothems—A promising new proxy for hydrological change? First results from a stalagmite from western Germany, *Chem Geol* **396**(0): 143 – 151.

Zhou, H., Chi, B., Lawrence, M., Zhao, J., Yan, J., Greig, A. and Feng, Y. (2008). High-resolution and precisely dated record of weathering and hydrological dynamics recorded by manganese and rare-earth elements in a stalagmite from Central China, *Quat Res* **69**(3): 438–446.

Zhou, H. Y., Wang, Q., Zhao, J. X., Zheng, L. N., Guan, H. Z., Feng, Y. X. and Greig, A. (2008). Rare earth elements and yttrium in a stalagmite from Central China and potential paleoclimatic implications, *Palaeogeogr Palaeoclimatol Palaeoecol* **270**(1-2): 128–138.

Zwaan, J. C. H., Buter, E., Mertz-Kraus, R. and Kane, R. E. (2015). Alluvial Sapphires from Montana: Inclusions, geochemistry, and Indications of a metasomatic origin, *Gems Gemol* **51**(4): 370–391.

Eidesstattliche Erklärung

Ich versichere hiermit, die Arbeit selbstständig und nur unter Verwendung der angegebenen Hilfsmittel verfasst zu haben. Ich habe oder hatte die hier als Dissertation vorgelegte Arbeit nicht als Prüfungsarbeit für eine staatliche oder andere wissenschaftliche Prüfung eingereicht. Ich hatte weder die jetzt als Dissertation vorgelegte Arbeit noch Teile davon bei einer anderen Fakultät bzw. einem anderen Fachbereich als Dissertation eingereicht.

Mainz, Juli 2016